Université de Valenciennes et du Hainaut-Cambrésis

Thèse de doctorat

Pour obtenir le grade de Docteur de l'Université de

VALENCIENNES ET DU HAINAUT-CAMBRESIS

Mécanique

Présentée et soutenue par Romain, BALIEU.

Le 03/12/2012, à Valenciennes

Ecole doctorale :
Sciences Pour l'Ingénieur (SPI)

Equipe de recherche, Laboratoire :
Laboratoire d'Automatique, de Mécanique et d'Informatique Industrielles et Humaines (LAMIH)

Modèle viscoélastique-viscoplastique couplé avec endommagement pour les matériaux polymères semi-cristallins

JURY

Président du jury
- Cognard, Jean-Yves. Yves. Professeur. ENSTA Bretagne.

Rapporteurs
- Hopperstad, Odd Sture. Professeur. Norvegian University of Science and Technology.
- Bahlouli, Nadia. Professeur. Université de Strasbourg.

Examinateurs
- Bennani, Bruno. Maître de Conférences. Université de Valencienne.
- Haugou, Grégory. Maître de Conférences. Université de Valenciennes.

Directeur de thèse
- Lauro, Franck. Professeur. Université de Valencienne.

Membres invités
- Matsumoto, Tsukatada. Senior Project Manager, CAE Group, Toyota.
- Mottola, Ernesto. Senior CAE Engineer, Toyota.

I would like to dedicate this thesis to my parents ...

Acknowledgements

The present research work is a collaboration between Toyota Motor Europe (TME) and the *Université de Valenciennes et du Hainaut cambrésis* (UVHC). I would like to acknowledge Kenji Nakaya san and Mr Enda Haran who followed the first part of my thesis and Tsukatada Matsumoto san and Doctor Ernesto Mottola for the industrial supervision until the end of this thesis.

I would like also to acknowledge my university supervisors Professor Franck Lauro and Doctor Bruno Bennani for their support and guidance during these three years of thesis. I would like to express my appreciation for their trust and confidence in my abilities.

I would like also to thank Professors Nadia Bahlouli and Odd Sture Opperstad for reviewing this dissertation and Professor Jean-Yves Cognard for presiding my jury.

I also thank all those who have contributed to this PhD work: Benjamin Bourrel, Denis Lesueur, Fahmi Chaari and especially to Rémi Dellile and Grégory Haugou for giving me their time in the experimental works. I would like to acknowledge all the LAMIH and TEMPo laboratory members and all those that I have met through this thesis, Cédric Hubert, David Morin, Fabrice Epée and many others without forgetting the other PhD students Olivier Mayeur and Olivier Cazier.

I am very grateful to all my family who have always been present for me and particularly my parents for their continuous support through all my studies.

Finally, I would like to especially thank Anays for her patience and support that helped me through the good and the hard times. Thank you.

Contents

List of Figures

List of Tables

Notations

Operators

x	Scalar
$\vec{x}$	Vector
x_i	Component of a vector $\vec{x}$
$\underset{\sim}{\mathbf{x}}$	Second order tensor
x_{ij}	Component of a second order tensor
$\underset{\approx}{\mathbf{x}}$	Fourth order tensor
$[X]$	Matrix
$\exp(\cdot)$	Exponential of $(\cdot)$
$\ln(\cdot)$	Natural logarithm of $(\cdot)$
$\mathrm{tr}(\cdot)$	Trace of $(\cdot)$
$\Delta(\cdot)$	Increment of $(\cdot)$, i.e. $\Delta(\cdot) = (\cdot)_{n+1} - (\cdot)_n$
$\nabla(\cdot)$	Gradient of $(\cdot)$
$\frac{\partial(\cdot)}{\partial a}$, $(\cdot)_{,a}$	Derivative of $(\cdot)$ with respect to a
$\dot{(\cdot)}$	Material time derivative of $(\cdot)$
$(\cdot)^{\mathrm{T}}$	Transpose of $(\cdot)$
$(:)$	Double contraction of tensors
$\otimes$	Tensor product of tensors or vectors
$\lvert x \rvert$	Absolute value of x
$\lVert \vec{x} \rVert$, $\lVert \underset{\sim}{\mathbf{x}} \rVert$	Euclidean norm of tensors or vectors
$< x >$	Macauley braket, i.e. $< x >= \frac{\lvert x \rvert + x}{2}$

Symbols

$[J]$	Jacobian matrix

$\underset{\approx}{\mathscr{L}}^{e}$	Elastic stiffness tensor
$\underset{\approx}{\mathscr{L}}$	Consistent tangent operator
$\underset{\approx}{\mathscr{L}}^{ve}$	Viscoelastic stiffness tensor
$\underset{\approx}{\mathscr{L}}^{ve}_{\infty}$	Long term viscoelastic stiffness tensor
ε, ε_{ij}, $\underset{\sim}{\boldsymbol{\varepsilon}}$	Uniaxial and tensorial infinitesimal total strain
ε^{e}, ε^{e}_{ij}, $\underset{\sim}{\boldsymbol{\varepsilon}}^{e}$	Uniaxial and tensorial infinitesimal elastic strains
ε^{p}, ε^{p}_{ij}, $\underset{\sim}{\boldsymbol{\varepsilon}}^{p}$	Uniaxial and tensorial infinitesimal plastic strains
ε^{ve}, ε^{ve}_{ij}, $\underset{\sim}{\boldsymbol{\varepsilon}}^{ve}$	Uniaxial and tensorial infinitesimal viscoelastic strains
ε^{vp}, ε^{vp}_{ij}, $\underset{\sim}{\boldsymbol{\varepsilon}}^{vp}$	Uniaxial and tensorial infinitesimal viscoplastic strains
ε^{v}, ε^{v}_{ij}, $\underset{\sim}{\boldsymbol{\varepsilon}}^{v}$	Uniaxial and tensorial infinitesimal viscous strains
ε_{∞}, $\varepsilon_{ij\,\infty}$, $\underset{\sim}{\boldsymbol{\varepsilon}}_{\infty}$	Uniaxial and tensorial long term strain
Γ, Γ_{ij},$\underset{\sim}{\boldsymbol{\Gamma}}$	Uniaxial and tensorial engineering strains
$\underset{\sim}{\mathbf{I}}$	Identity tensor
$\underset{\approx d}{\mathbf{I}}$	Deviatoric projection tensor
ψ	Gaussian weight function
κ	Equivalent (visco)plastic strain
λ	(Visco)Plastic multiplier
$\mathbb{K}$	Nonlocal penalty factor
$\mathscr{D}^{mech}$	Total power of dissipation
$\mathscr{D}^{p}$	Plastic power of dissipation
$\mathscr{D}^{th}$	Thermal power of dissipation
μ	Viscosity coefficient
ν	Poisson ratio
Ω	Domain of a body
$\overset{\circ}{\underset{\sim}{\mathbf{T}}}$	Objective rate of a stress tensor $\underset{\sim}{\mathbf{T}}$
$\overset{\circ^{R}}{\underset{\sim}{\mathbf{T}}}$	Green-naghdi rate of a stress tensor $\underset{\sim}{\mathbf{T}}$
$\overset{\circ^{Z}}{\underset{\sim}{\mathbf{T}}}$	Zaremba-Jaumann rate of a stress tensor $\underset{\sim}{\mathbf{T}}$
Ψ	Helmholtz specific free energy
Ψ^{e}	Elastic state potential
Ψ^{p}	Plastic state potential
Ψ^{ve}	Viscoelastic state potential
Ψ^{vp}	Viscoplastic state potential
ρ	Material density
$\underset{\approx}{\mathscr{R}}^{ve}$	Relaxation stiffness tensor

σ, σ_{ij}, $\underset{\sim}{\boldsymbol{\sigma}}$	Uniaxial and tensorial Cauchy stresses
Σ, Σ_{ij}, $\underset{\sim}{\boldsymbol{\Sigma}}$	Uniaxial and tensorial engineering stresses
σ^{e}, σ^{e}_{ij}, $\underset{\sim}{\boldsymbol{\sigma}}^{e}$	Uniaxial and tensorial elastic Cauchy stresses
σ^{v}, σ^{v}_{ij}, $\underset{\sim}{\boldsymbol{\sigma}}^{v}$	Uniaxial and tensorial viscous Cauchy stresses
σ_{e}	von Mises equivalent stress
σ_{∞}, $\sigma_{ij\,\infty}$, $\underset{\sim}{\boldsymbol{\sigma}}_{\infty}$	Uniaxial and tensorial long term Cauchy stresses
τ	Relaxation time
T_{g}	Glass transition temperature
T_{m}	Melting temperature
Θ	Total dissipation potential
$\tilde{\sigma}$, $\tilde{\sigma}_{ij}$, $\underset{\sim}{\tilde{\boldsymbol{\sigma}}}$	Uniaxial and tensorial effective Cauchy stresses
$\tilde{S}$	Effective surface
$\underset{\sim}{\mathbf{n}}$	(Visco)Plastic flow tensor
$\underset{\sim}{\mathbf{D}}$	Rate deformation tensor
$\underset{\sim}{\mathbf{D}}^{ve}$	Viscoelastic part of the rate deformation tensor
$\underset{\sim}{\mathbf{D}}^{vp}$	Viscoplastic part of the rate deformation tensor
$\underset{\sim}{\mathbf{F}}$	Deformation gradient tensor
$\underset{\sim}{\mathbf{L}}$	Velocity gradient tensor
$\underset{\sim}{\mathbf{R}}$	Orthogonal tensor
$\underset{\sim}{\mathbf{U}}$	Right stretch tensor
$\underset{\sim}{\mathbf{V}}$	Left stretch tensor
$\underset{\sim}{\mathbf{W}}$	Spin tensor
ψ	Normalising nonlocal factor
Ξ	Normalised relaxation modulus
D	Isotropic damage variable
E	Young modulus
e, e_{ij}, $\underset{\sim}{\mathbf{e}}$	Uniaxial and tensorial total Henky strains
e^{ve}, e^{ve}_{ij}, $\underset{\sim}{\mathbf{e}}^{ve}$	Uniaxial and tensorial viscoelastic Henky strains
e^{vp}, e^{vp}_{ij}, $\underset{\sim}{\mathbf{e}}^{vp}$	Uniaxial and tensorial viscoplastic Henky strains
E_{∞}	Long term Young modulus
F^{D}	Damage dissipation potential
F^{p}	Plastic dissipation potential
F^{vp}	Viscoplastic dissipation potential
f^{vp}	Yield surface
G	Shear modulus

G_∞	Long term shear modulus
H	Hardening modulus
h, h_{ij}, $\underset{\sim}{\mathbf{h}}$	Uniaxial and tensorial Cauchy stresses in a Maxwell element
I_1	First invariant of the stress tensor
J_2	Second invariant of the deviatoric stress tensor
K	Bulk modulus
K_∞	Long term bulk modulus
l	Intrinsic length
q	Heat flux
R	Isotropic hardening conjugate force
r	Isotropic hardening state variable
S	Real surface
s	Specific entropy
S, S_{ij}, $\underset{\sim}{\mathbf{S}}$	Uniaxial and tensorial deviatoric stresses
S^D	Cracks and voids area
T	Temperature
Y	Isotropic damage conjugate force
$\underset{\sim}{\mathbf{\Lambda}}$	Rotation tensor
$\underset{\sim}{\mathbf{\Omega}}^*$	Skew symmetric tensor
$\underset{\sim}{\mathbf{\Omega}}^R$	Polar skew symmetric tensor

Material parameters

α^+	Dilatation parameter
α^-	Compaction parameter
η	Hydrostatic pressure parameter
$\dot{\kappa}_0$	Strain rate parameter
σ_c	Compression yield stress
σ_t	Tensile yield stress
$b1$, $b2$, $b3$, $b4$, $b5$	Hardening parameters
k_c	Damage parameter
p	Hydrostatic pressure
$Q1$, $Q2$, $Q3$	Hardening parameters
n	Strain rate parameter

Chapter 1

Introduction

DUE to the attractive mechanical properties and the ease processability, polymer materials are widely used in structural applications. In automotive sector, polymer materials are increasingly being used for structural parts like bumpers, fenders... and require particular specifications in term of quality, safety and mechanical performance (e.g. stiffness, strength, energy absorption). The complex behaviour of polymer materials have been largely studied in the last decades and it results an important number of external factors influencing their behaviour like strain-rate, time, stress triaxiality, temperature, humidity and fabrication process or intrinsic factors linked to the micro-structure of the material. The wide range of existing polymers is completed by adding fillers during the material fabrication. Filled polymer materials have been developed to increase performance and to reduce the production cost. The addition of fillers in polymer materials have obviously some consequences on the micro-structural deformation and consequently on the macroscopic behaviour of the material. Finite element simulations of polymer materials require therefore accurate behaviour models in order to take these influencing factors into account. Two approaches are generally used to describe the behaviour of polymer materials. The physical approach where the numerical response is actuated by the micro-structure of the material and the phenomenological approach where the physical discontinuities of the material at the micro-structural level (chains, fillers, cracks and voids) are homogenised in a representative volume element. The last approach, which is inscribed in the framework of continuum mechanics, is attractive for industrial applications where the material parameters arise from classic experiments.

1.1 Objectives and outlines

This work deals with the behaviour modelling of a semi-crystalline thermoplastic under isothermal condition on a large strain rate range for various loading conditions. The objective of this research is the characterisation and the modelling of a mineral filled semi-crystalline polymer (polypropylene) used in automotive sector. Experimental tests at several loading conditions and strain rates (quasi-static and dynamic) are carried out to characterise the behaviour of the material investigated. According to the experimental observations a constitutive model able to describe the mechanical behaviour of the material is developed and implemented in two commercial finite element codes (implicit and explicit). The proposed constitutive model is developed in the framework of continuum mechanics where the material parameters are deduced from the conducted experiments. The numerical responses predicted by the finite element simulations are compared to the experimental data in order to evaluate the accuracy of the constitutive model. The main axes of this thesis works are therefore defined as follows:

- to conduct experimental tests able to characterise the mineral filled semi-crystalline polymer under several loadings on a large strain rate range,
- to develop and implement a constitutive model which satisfy the requirement of the polymeric material simulation,
- to validate the constitutive model by comparing finite element simulations and experimental data.

Chapter 2 presents general concepts about polymeric materials in a micro-structural and macroscopic point of view. The second part of this chapter deals with the state of the art concerning the modelling of polymeric material behaviour. A revue of physical and phenomenological constitutive models where viscoelasticity, viscoplasticity, damage, finite strain and mesh dependency are treated in order to define the motivations of the selected choices for the model development.

Chapter 3 focuses on the numerical developments. Firstly the general theory of a linear viscoelastic model is presented with its implementation in a finite element code. Secondly the thermodynamical framework of the classic continuum plasticity is briefly presented in order to introduce the developed constitutive model. The proposed constitutive model is presented further. In this part, the description and the implementation of the model in an implicit and an explicit finite element codes is developed. The extension of this constitutive model on shell element, finite strain and with a nonlocal damage model is presented as well.

Chapter 4 describes the experiments conducted for the characterisation of the polymeric material investigated. Experimental procedures and results are detailed firstly. In a second time, the material parameter identification is presented.

Chapter 5 is devoted to the validation of the constitutive model. First, a verification in term of coherence between the explicit and the implicit finite element simulations is presented. Secondly, a verification of the mesh dependency is developed for several finite element simulations carried out with various element types. Comparisons between the responses predicted by the numerical model and the experimental data are presented in the last part of this chapter.

Finally, conclusions and recommendations for further researches are given in Chapter 6.

Chapter 2

Basic concepts and state of art of semi-crystalline polymer modelling

POLYMER material can be divided in several classes which depend on the organisation of the chains which compose the material structure. The definition of the different classes with their consequences on the macroscopic behaviour is given, firstly. The mechanical behaviour of semi-crystalline polymers is detailed in a second time. The relation between the micro-structure and the macroscopic behaviour is presented in order to have a better comprehension of the observed mechanical behaviours. The complex behaviour of semi-crystalline polymers with their strain rate, time, temperature, pressure dependency and volume variation is detailed in this chapter. Furthermore, the case of mineral filled semi-crystalline polymer is introduced with a comparison between neat and filled polypropylene in term of behaviour damage and fracture. In a last part, a revue of existing models developed in order to describe the behaviour of polymeric materials is presented. A comprehensive state of art where viscoelasticity, viscoplasticity, finite strain, damage and mesh dependency are discussed in order to understand the motivations of the proposed constitutive model.

2.1 Generalities about polymer materials

Polymer materials result of the polymerisation of small size organic molecules, called monomers, in order to form macromolecule. The results of the chemical reaction, i.e. polymerisation, is a chain of carbon atoms linked together with covalent bonds. During the polymerisation, the structure of the formed chains can differs. Three architectures of

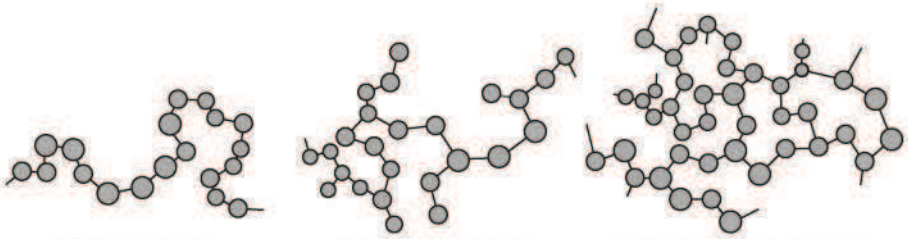

(a) linear chain (b) branched chain (c) crosslinked polymer

Figure 2.1: *Architecture of polymer chain: a linear chain (a), a branched chain (b) and a crosslinked polymer (c).*

polymer molecules can be distinguish: linear chain, branched chain and crossliked polymer. The linear chain class includes polymer with no branches or crosslinks. For a number of chains sufficiently important, the chains can be entangled. A polymer having extended sequences of repeating units attached to backbone appertains in the branched chain class. The last class is the crossliked polymer where the linear or branched chains are covalently linked to each other at several points (not just ends). Fig. 2.1 shows the three architectures of polymer molecules. The architecture of polymer molecules have a strong influence on the macroscopic behaviour of the material. A crosslinked polymer is very stiff, cannot be melted or made to flow with heat and is not reprocessable due to chain decomposition or bond breakage. This is the case of the thermosets. In the other hand, linear or entangled polymer can be melted or made to flow with heat and allows to be re-shaped. It results a very dependent temperature behaviour. The thermoplastics, which are widely used in industry, are situated in this class of polymers and are therefore characterised by their glass and melting temperatures T_g and T_m, respectively.

At the liquid state, i.e. above the melting temperature, all the thermoplastics possess a random molecular orientation and are therefore in an amorphous state. Upon cooling to the solid state, some thermoplastics have the property to order their structures. This phenomenon is called crystallisation. Generally, thermoplastic materials do not crystallise easily by reason of the crystallisation requires considerable ordering of entangled macromolecules. When the molecular disorder is complete, the material is totally amorphous. As soon as the disorder is partial, on part of the macromolecules are ordered in the form of crystalline phases in a amorphous matrix. This kind of material are called semi-crystalline polymer. The structure of a semi-crystalline polymer is therefore composed of crystalline domains separated by regions of amorphous polymer. The crystalline domains is composed of oriented layers, so called lamellae which have an approximate thickness of 5 to 50 nm. The lamellae form a superstructure called spherulite (Fig. 2.2) which have a typical diameter of 50 to 500 µm. Only this class of material is under investigation in this thesis.

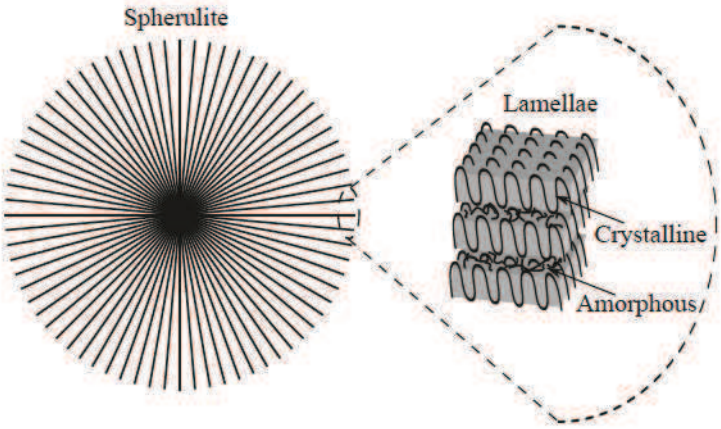

Figure 2.2: *Schematic representation of a spherulitic structure with their crystalline lamellae separated by amorphous layers.*

2.2 Mechanical behaviour of semi-crystalline polymers

The observed macroscopic behaviour of semi-crystalline polymers is very complex and depends on the properties of each phase and on the mechanical coupling between them. Semi-crystalline materials exhibit rate and time dependent behaviours. The rate dependency can be observed by an increase of the stiffness and the yield stress at increasing strain rate. The long time to recover the zero stress after loading of the material highlights the time dependent behaviour. The typical mechanical response of a ductile semi-crystalline polymer under uniaxial tensile loading is summarised in Fig. 2.3. The mechanical response of all polymers is characterised by a viscoelastic and a viscoplastic part. At very low strain, the behaviour is linear viscoelastic, while with increasing load the behaviour becomes progressively nonlinear viscoelastic until the yield stress. For higher deformation, the viscoplastic part becomes dominant and a structural evolution, which reduces the resistance of the

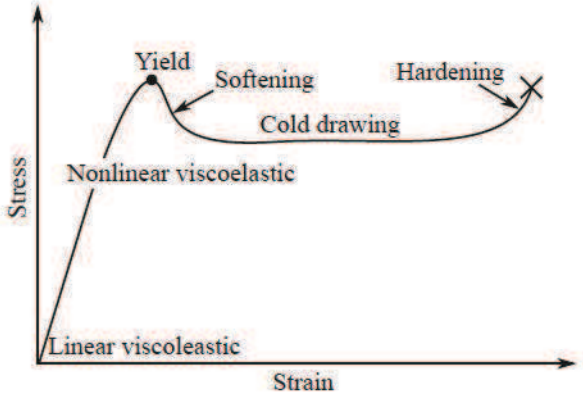

Figure 2.3: *Macroscopic tensile behaviour of a semi-crystalline polymer material.*

material to plastic flow, i.e. strain softening, appears. The cold drawing, which appears after the strain-softening, begins with the necking which is a narrowing of the material deformation to a smaller cross section. Contrary to metallic material, at increasing strain, a propagation of the necking occurs in the entire specimen. During the necking an extensive reorganisation of the material takes place, the spherulites are broken up and with an increasing deformation, the molecules become oriented in the direction of the stretch which gives rise to a subsequent increase of stress at large deformations, i.e. strain hardening. During uniaxial deformation of thermoplastic material, a transition from the initial spherulitic structure by plastic deformation to the final fibrillar structure takes place with the destruction of the lamellae, alignment and orientation of the structure by longitudinal sliding motion of the fibrils. The plastic deformation of semi-crystalline polymer can therefore be summarised in three steps: (1) pre-neck deformation of the spherulitic structure in the whole sample, (2) large deformation in the neck with transformation of the spherulitic structure to fibrillar structure, finally (3) post neck deformation of the fibrillar structure with an increase of plastic modulus.
The yield stress described in Fig. 2.3 which is located just before the strain softening behaviour is not the unique interpretation of the beginning of the viscoplastic state. Raghava *et al.* (1973) have defined the yield stress as the intersection between the strain displacement that is equivalent to a 0.3 % offset with the true stress curve. This definition of the

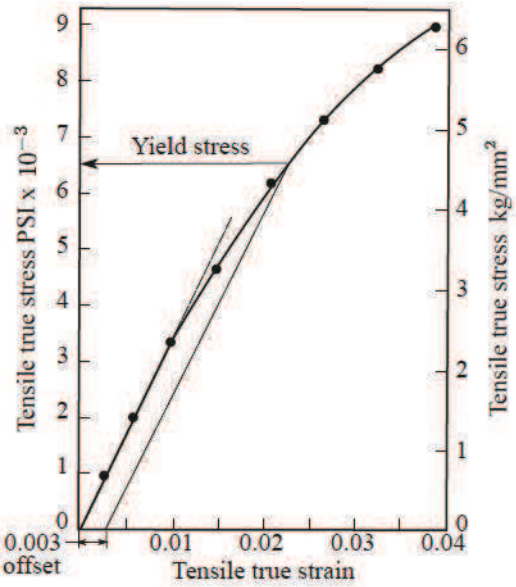

Figure 2.4: *Tensile true stress strain plot for PC illustrating the selection of yield stress as based upon offset of 0.3 % (i.e. a strain of 0.003). Data reproduced from Raghava* et al. *(1973).*

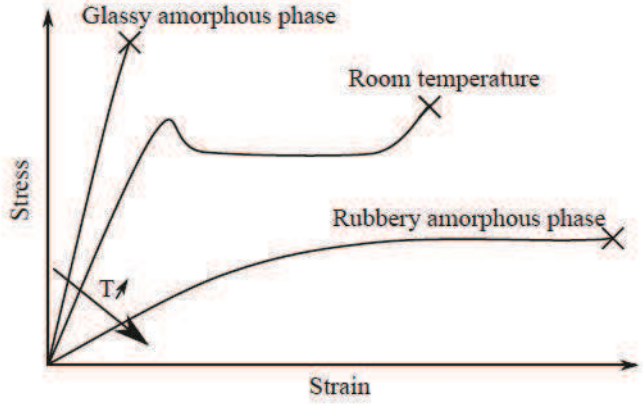

Figure 2.5: *Temperature effect on the typical stress-strain curves of semi-crystalline polymers.*

yield stress is illustrated on a polycarbonate* (PC) in (Fig. 2.4). With this definition of the yield stress, the material can be characterised by a linear viscoelastic state and beyond the yield stress, the viscoplastic state takes place. The viscoplastic state occurs therefore earlier without to be in a nonlinear viscoelastic state.

Semi-crystalline polymers exhibit a strong dependency to the temperature. If the amorphous portion of the material is rubbery, the stiffness of the material decreases significantly and the stretching necessary for the fracture becomes very large. On the other hand, by decreasing the temperature, the amorphous phase of the material becomes glassy and the macroscopic behaviour becomes brittle. A schematic representation of the temperature effect on the typical stress-strain curves of semi-crystalline polymers is presented in Fig. 2.5. Polymer materials exhibit a pressure dependent behaviour. Khan and Farrokh (2006) have carried out non proportional biaxial compression test on a thermoplastic nylon 101 to highlight this pressure dependency. For the non-proportional biaxial compression experiments, a rectangular block specimen is, first, subjected to uniaxial compression in the loading direction 1 and then, after some finite deformation, it is deformed under biaxial compression due to constraint in direction 2 which is becoming active after certain deformation in the direction 1. The results of this test is shown in Fig. 2.6. It results clearly that, unlike most annealed metals, the biaxial loading equivalent stress-strain relationship does not coincide with the uniaxial stress-strain response for the polymer nylon 101.

Another important typical behaviour of semi-crystalline polymer is the volume change during the viscoplastic deformation. G'Sell *et al.* (2002) have measured the volumetric strain on a polyethylene terephtalate (PET) and high-impact polystyrene (HIPS) by using a video-controlled testing system where the longitudinal and transverse strains are measured by following markers positioned on the specimens. The results of volume strain

*The polycarbonate is not a semi-crystalline polymer, nevertheless the aim of the figure is to illustrate the methodology.

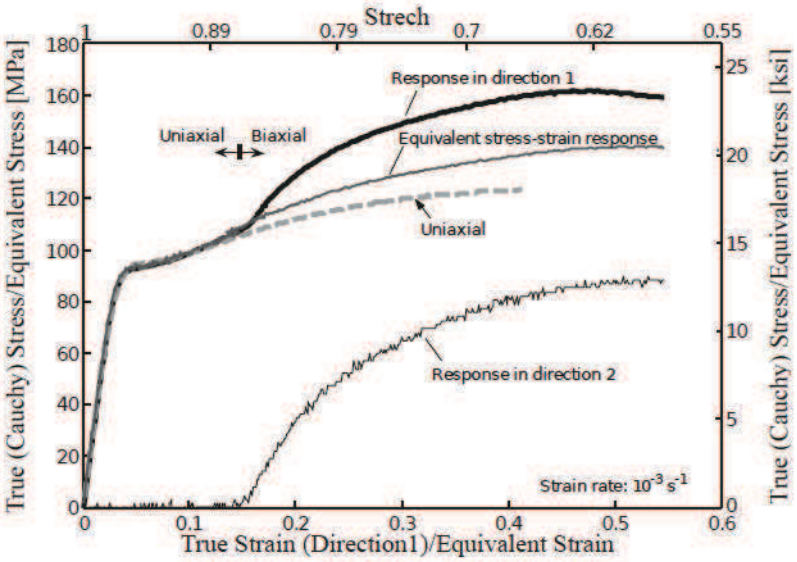

Figure 2.6: *Non-proportional biaxial compression response of nylon 101 at an engineering strain rate (stretch rate) of* 10^{-3} s^{-1}. *Data reproduced from Khan and Farrokh (2006).*

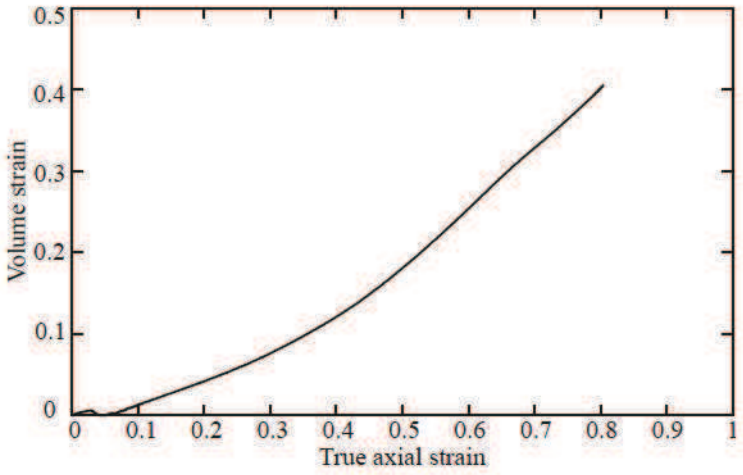

Figure 2.7: *Mechanical behavior of PET under tensile testing at ambient temperature: evolution of volume strain vs. axial true strain. Data reproduced from G'Sell* et al. *(2002).*

measurement on a PET under uniaxial tensile loading is given in Fig. 2.7. An increase of the volume variation at increasing axial strain is observed.

Semi-crystalline polymers have therefore a strain-rate, time, temperature and pressure dependent behaviour which is accompanied by volume change during the viscoplastic deformation. Furthermore, the material under investigation in this thesis is a mineral filled semi-crystalline polymer (polypropylene). The addition of mineral fillers to polymers is mainly done in order to increase the stiffness of the material. Fillers have also been used to decrease the dielectric loss or increase absorption of infrared radiation. However,

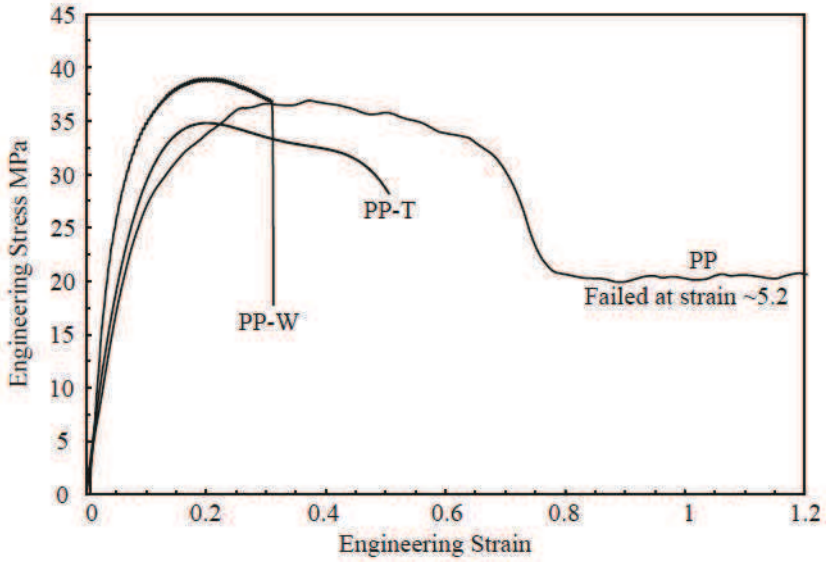

Figure 2.8: *Engineering stress-strain plot of neat (PP) and mineral-reinforced polymeric materials (wollastonite (PP-W) and talc(PP-T)) at a selected speed loading of 50 mm.min^{-1}. Data reproduced from Hadal* et al. *(2004).*

many studies concerning the modification of semi-crystalline polymer with rigid, inorganic fillers report a significant decrease of toughness compared to neat polymer (Dasari *et al.*, 2004; Hadal and Misra, 2004). Nevertheless, several studies demonstrating an increase in toughness with rigid particle fillers in certain systems such as filled polypropylene and filled polyethylene (Katz and Mileski, 1988). A study of the influence of polypropylenes reinforced with wollastonite and talc under tensile loading were carried out by Hadal *et al.* (2004). In their works, tensile bars were also cast without mineral particles to study the influence of reinforcement with wollastonite and talc which have an approximate median particle size of 7.5 and 8 μm, respectively. The volume fraction of wollastonite and talc was kept constant at around 20%. Engineering stress-strain plots for neat and mineral-reinforced polypropylenes at a selected speed loading of 50 mm.min^{-1} are presented in Fig. 2.8. It results that the reinforcement of polypropylenes with wollastonite and talc increased the stiffness of the material and decreased percentage of strain-to-fracture. In term of yield stress, it appears to be a marginal increase in the yield stress on the addition of wollastonite mineral to the polypropylene matrix and a slight decrease on the addition of talc. In term of fracture, the authors have noted that with the presence of reinforcement, the crystallisation process is accelerated and there is an increase in percentage of crystallinity of polypropylenes, which can be attributed to enhanced nucleation in the presence of minerals. The decrease in percentage of fracture strain in the wollastonite- and talc-reinforced polypropylenes can be explained by the fact that the matrix/particle interface provides po-

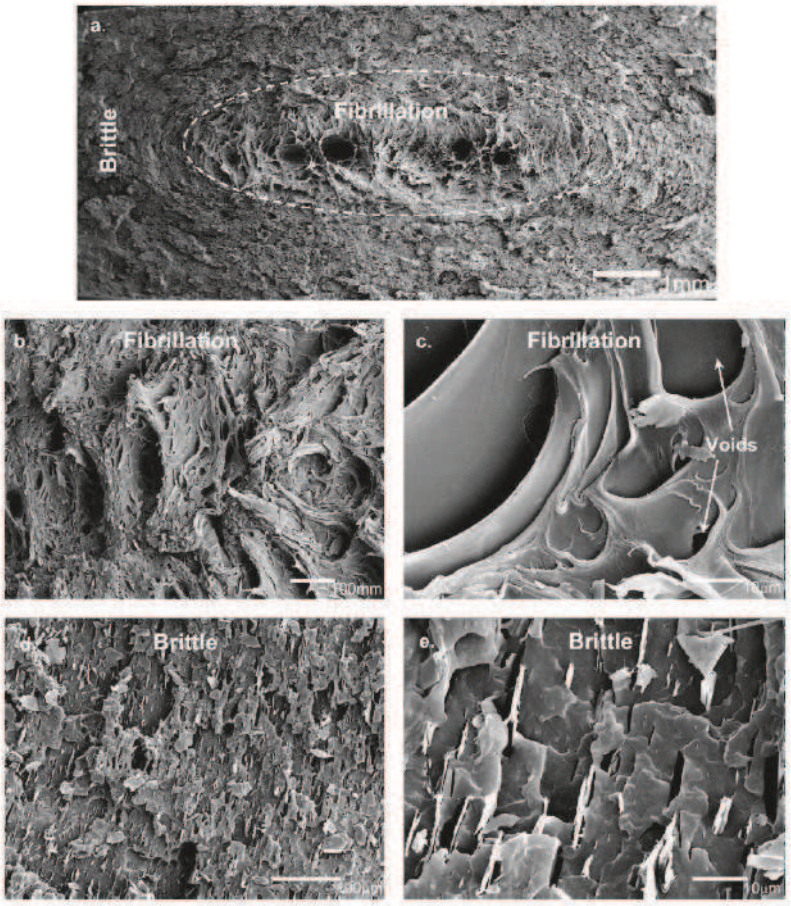

Figure 2.9: *Low magnification SEM micrograph of the fracture surface of talc-reinforced polypropylene tensile tested at a speed loading of 50 mm.min^{-1} (a) along with the high magnification micrographs of the two modes of fracture, fibrillation (b, c) and brittle (d, e) showing voiding and detached mineral particles. Data reproduced from Hadal* et al. *(2004).*

tential site for nucleation. In mineral filled materials, plastic deformation processes are initiated with wedge-shaped micro-cracks. Further straining led to the tearing of material with consequent debonding of mineral particles. The microstructure of the sample appeared porous and consisted of severely deformed fibrils with voids. Fig. 2.9 shows the low and high magnification SEM micrographs of the fracture surface of a talc-reinforced polypropylene illustrating different modes of fracture. Two types of fracture morphology were observed, fibrillation (ductile) in the centre and brittle away from the centre. The fracture is initiated in the core of the specimen where large voids are nucleated and rapidly extends outwards leading to brittle mode of deformation surrounding the fibrillated fracture. The previous results show that the addition of rigid, inorganic particles in a semi-crystalline polymer changes the plasticity, damage and fracture process. With a mineral-filled material the cavitation phenomenon causes the nucleation and growth of

micro-voids and micro-cracks, i.e. damage, with debonding of mineral particles.

Modelling strategy

Without taking into account the temperature effect[†], a strain rate and time dependent material model with non-isochoric viscoplastic deformation which has a pressure dependent yield surface coupled with a damage model is therefore necessary to reproduce the observed behaviour of mineral filled semi-crystalline polymer.

2.3 State of art of polymer modelling

Semi-crystalline polymers are widely used for structural applications in the automotive sector. Their complex mechanical behaviour, due to the important number of dependent parameters (fabrication process, temperature, humidity, strain rate and stress triaxiality), has been widely investigated for many years in the literature. In the two last decades, many constitutive models have been developed for the inelastic behaviour modelling of some polymers. Two approaches are widely used to capture the complex behaviour of solid polymers. The behaviour of amorphous polymers is usually modelled by using a physical approach, on the other way, the phenomenological approach is usually applied to study semi-crystalline polymers.

A physical-based model where the constitutive equations are based on the macromolecular structure of amorphous polymer have been developed in the uniaxial case by Haward and Thackray (1968). A widely-used, three-dimensional extension of this model was proposed by Boyce *et al.* (1988); Arruda and Boyce (1993); Wu and van der Giessen (1995); Anand and Gurtin (2003). More recently, Boyce *et al.* (2000) described the elasto-viscoplastic behaviour of amorphous polymer by including two parallel resistances in description of the mechanical behaviour: one due to the intermolecular resistance and the other for the molecular network interaction. In the same way, Anand and Ames (2006); Anand *et al.* (2009); Ames *et al.* (2009) have extended the model proposed by Boyce *et al.* (1988) where they describe the behaviour of amorphous polymer by one resistance due to the molecular network interaction in parallel with a generalised Kelvin-Voigt model in order to describe the intermolecular interaction. Physical approaches have been used as well to model behaviour of semi-crystalline polymers. Ahzi *et al.* (2003) proposed a model where the intermolecular resistance is treated in a composite framework where the crystalline and amorphous phases are considered as two separate resistances. In the same way, Ayoub *et al.*

[†]The temperature effect is not investigated and therefore not modelled in this thesis.

(2010, 2011b) have proposed rheological model for semi-crystalline polymer. A first resistance is used for intermolecular interaction and the other one for the molecular network stretching and orientation process.

The micro-structure of semi-crystalline polymers is composed by crystalline lamellae and amorphous regions organised like composite sandwich structure. The degree of crystallinity influences mechanical properties such as Young modulus and yield stress. Following this micro-structure, some multi-scale constitutive models have been developed to capture their viscoelastic, viscoplastic behaviour (Parks and Ahzi, 1990; Lee *et al.*, 1993; Nikolov and Doghri, 2000; Drozdov and Gupta, 2003; van Dommelen *et al.*, 2003; Drozdov and de C. Christiansen, 2007; Regrain *et al.*, 2009). In these models, each macroscopic material point is assumed to be the centre of a representative volume element which is an aggregate of two phase layered composite inclusions. Each inclusion consists on a stack of parallel crystalline lamellae with the adjacent amorphous layers. These kinds of models are good ways of evaluating the influence of the degree of crystallinity of the material.

Although physical models are currently used for amorphous polymer modelling, this approach is also used for-semi crystalline polymer. The previous theories are attractive to describe the macroscopic behaviour of the material by taking the micro-structure evolution into account, the identification of the material parameters is complex and not so adapted for industrial applications. Some phenomenological viscoelastic-viscoplastic rheological models based on the connection of Hooke, Newton and slider elements were developed in order to describe the uniaxial response of some polymers. Khan and Zhang (2001) have developed a rheological model to simulate the time dependent response of a polytetrafluoroethylene at room temperature and on a wide range of strain rates. Another phenomenological model based on rheological equations was proposed by Khan *et al.* (2006) to describe the time and temperature dependent mechanical response of Adiprene-L100. Unfortunately, these models does not take the pressure effect into account and an important numbers of parameters are required to obtain good predictions.

Although the deformation mechanism of semi-crystalline polymer is clearly influenced by the crystalline and the amorphous phases, another formalism coming within the framework of continuum mechanics considers that the physical discontinuities at the microstructural level is not expressed explicitly but are described globally at the level of a homogenised bulk element of the material (i.e. representative volume element). In this case, the general principles of thermodynamics with internal variables are used to represent the mechanical behaviour of polymeric material considering an homogeneous medium. This framework has been widely used to model the inelastic behaviour of polycrystalline metals and their alloys. Chaboche (1997) has discussed the ability of the classic thermody-

namics of irreversible processes framework to describe the behaviour of polymer material. The formalism proposed by Chaboche corresponds to an extension of the "generalised standard material" concept where the classic viscoplasticity (initially developed for metals) can be particularised into non-linear viscoelastic models (polymer) by eliminating the plasticity threshold. More recently, elasto-viscoplastic constitutive models based on overstress (VBO) derived from the unified state variable theory for metallic material (Krempl *et al.*, 1986) have been extended for polymer modelling by Krempl and Ho (2001); Ho and Krempl (2002); Krempl and Khan (2003); Colak (2005). In the same way, Colak and Dusunceli (2006); Dusunceli and Colak (2008) have modified the Krempl model to take the degree of cristallinity into account. Recently, Khan and Yeakle (2011) proposed a modification of the viscoplasticity theory based on overstress formulation in order to capture the creep response during the unloading stress-strain path of amorphous and semi-crystalline polymers. Drozdov and Christiansen (2007) proposed a constitutive model based on the thermodynamic of irreversible process to describe the cyclic behaviour of a hight density polyethylene. All these models developed in the framework of continuum mechanics are written with the assumption of incompressibility. The non-isochoric plastic deformation of many polymers has been studied by various authors. G'Sell *et al.* (2002) measured the volumetric strain on a polyethylene terephtalate (PET) and high-impact polystyrene (HIPS) by using a video-controlled testing. In the same way, the volume strain measurement for polypropylene material was quantified by G'Sell *et al.* (2004); Jerabek *et al.* (2010). According to these results, the plastic deformation should not be considered as an isochoric process. Furthermore, the previous constitutive models written in a thermodynamical framework does not take the hydrostatic pressure into account. The influence of the hydrostatic pressure on the yield stress of polymers has been widely studied as well (Wang and Pan, 2006; Khan and Farrokh, 2006). In the particular case of semi-crystalline polypropylene, Sauer and Pae (1974) have highlighted this pressure dependency. In order to overcome this deficiency, Ghorbel (2008) proposed a constitutive model by using the general principles of thermodynamics with internal variables in order to predict the viscoplastic behaviour of amorphous and semi-crystalline polymers under monotonic and cyclic loading in tension and compression. In this model, Ghorbel proposed a dissipation potential decomposed in a recovery part and a viscoplastic one which possesses a pressure dependent yield criterion. The model provides good agreement with experimental data on various polymers.

The formalism of a constitutive model for semi-crystalline polymer developed within the continuum mechanics framework is attractive. Classic viscoplastic models, initially developed for metallic materials, can be extended for polymers and the material parameters can be identified by using simple experimental tests (uniaxial tension, compression ...).

Nevertheless, in the previous described models, the viscoelastic behaviour of polymeric materials is not taken into account[‡]. Linear viscoelasticity is commonly described using linear response theory, which results in a Boltzmann single integral representation. The characteristic viscoelastic functions are supplied either as continuous or discrete spectra of relaxation times (Tschoegl, 1989). For nonlinear viscoelastic models, different constitutive relations are available. Most of them are generalisations of the linear Boltzmann integral, employing higher order stress or strain terms (Han, 1985). Some constitutive models where the viscoelastic-viscoplastic behaviour is developed within the continuum mechanics framework are present in the literature, e.g. Ghoneim and Chen (1983); Frank and Brockman (2001). A combined viscoelastic-viscoplastic model has been developed by Kim and Muliana (2010) to describe the time and rate dependent behaviour of particle reinforced composites. In this formulation, the well-known nonlinear viscoelastic model proposed by Schapery (1969) is combined with the viscoplastic model developed by Perzyna (1966). Recently, Miled *et al.* (2011) have proposed a viscoelastic-viscoplastic constitutive model where a linear viscoelastic model is coupled with a viscoplastic formulation in order to reproduce the behaviour of a high density polyethylene. The two previous models are attractive for semi-crystalline polymer modelling, nevertheless they are stated in the classic J_2 plasticity (or viscoplasticity) theory[§].

A coupled viscoelastic-viscoplastic constitutive model developed in the continuum mechanics framework with a viscoelastic model where the stress is given as a Boltzmann integral of the viscoelastic strain (i.e. linear viscoelastic model as in Miled *et al.* (2011)) coupled to a viscoplastic formulation with a pressure dependent yield surface and assuming the compressibility, seems to be an attractive way to describe the semi-crystalline polymer behaviour. Nevertheless, the small strain assumption of these constitutive models is the main limitation for polymer modelling. Even if physical based models are widely stated under finite strain framework, the continuum mechanical models are most frequently developed under infinitesimal strain framework where the total strain tensor is divided into an elastic and a plastic part (or a viscoelastic and viscoplastic part). In finite deformation plasticity, there is usually two approaches. The first class is based on the multiplicative decomposition of the deformation gradient tensor in an elastic part and a plastic one. This decomposition is mainly used with hyperelastic-plastic constitutive models[¶]. The second class is based on hypoelastic-plastic relations where the rate of the deformation tensor is divided in an

[‡]The constitutive model developed by Chaboche (Chaboche, 1997) possesses a viscoelastic formulation but not coupled with viscoplasticity.

[§]The J_2 plasticity theory uses a yield function which depends only on the second invariant of the deviatoric strain tensor. The hydrostatic pressure is therefore not taking into account.

[¶]Most of physical models developed for polymeric materials are based on this decomposition of the deformation gradient.

elastic and plastic components. This formulation is very attractive from the computational point of view and is valid for materials where the elastic part remains small in front of the plastic part. The major requirement in large deformation continuum mechanics using hypoelastic formulation is to achieve incremental objectivity and many objective rates are introduced in literature instead of material time derivative in order to retain material frame indifference during large deformations/rotations, e.g. Zaremba-Jaumann-Noll, Green-McInnis-Naghdi, Truesdell or Oldroyd stress rates. Extensive review on objective stress rates appears in the literature Xiao *et al.* (2000). In order to extend a constitutive model which is initially developed in the small strain framework, the hypoelastic formulation is the more appropriate.

In the particular case of mineral filled semi-crystalline polymers, the well known cavitation phenomenon due to the decohesion at matrix-particle interface occurs. In this case, the viscoelastic-viscoplastic response of the material is accompanied by damage in the form of nucleation, growth and coalescence of cavities. For these kinds of materials, constant inelastic volume during deformation cannot be assumed. Many authors have studied the effects of microvoids and microcracks on the plastic properties. They highlighted that the major effects of voids are the continuous deterioration of the material stiffness and the phenomenon of strain softening as well as the presence of plastic dilatation. Constitutive models including damage have been proposed to take these phenomena into account. These constitutive models can be classified in two categories: micro-structural models which describe void growth and coalescence as Gurson's model (Gurson, 1977) and continuum damage mechanics (CDM) models as Lemaitre's model (Lemaitre, 1985a). In the first approach, the constitutive relations are constructed from microscopic components of material (matrix and voids) and their individual and interactive behaviours. Many modifications of the Gurson damage model have been developed in the literature for metallic materials (Tvergaard, 1982; Tvergaard and Needleman, 1984; Gologanu *et al.*, 1993; Lauro *et al.*, 1997, 1998; Nahshon and Hutchinson, 2007; Besson, 2009). To capture the polymer degradation of the yield surface, some modifications have been made as well. Lazzeri and Bucknall (1995); Jeong and Pan (1995) have proposed a modification of the Gurson potential in order to take the hydrostatic pressure dependency of the matrix into account. Steenbrink *et al.* (1997); Pijnenburg and der Giessen (2001) have shown that elasticity effect can be significant for polymers and have modified the original Gurson potential with this aim. Laiarinandrasana *et al.* (2009) modeled the void volume fraction evolution at different temperatures of a Polyvinylidene Fluoride (PVDF) by using a modified Gurson-Tvergaard-Needleman (GTN) model. This GTN model was modified by Challier *et al.* (2006) to introduce isotropic hardening and strain rate effect in the PVDF matrix. Zaïri

et al. (2005) proposed a coupling between micromechanical GTN model and phenomenological Bodner and Partom theory (Bodner and Partom, 1975) to represent the elastoviscoplastic and damage behaviour of RTPMMA. Afterwards, two rubber-toughened glassy polymers (RTPMMA and HIPS) was modelled with this model (Zaïri *et al.*, 2008).

The second approach, is the continuum damage mechanic (CDM). It is based on the thermodynamics of the irreversible processes. The damage variable used represents the average material degradation which reflects the various types of damage at the microscopic level. This damage variable introduced by Kachanov (1958) is a scalar in the case of isotropic damage or a tensor (second or fourth order) for anisotropic damage. The damage variable is mostly function of the energy density release rate (Lemaitre, 1985a,b; Chaboche, 1997; Voyiadjis and Al-Rub, 2003; Voyiadjis and Dorgan, 2007; Celentano and Chaboche, 2007; Hammi and Horstemeyer, 2007; Cicekli *et al.*, 2007; Haddag *et al.*, 2009). In the same way, Bonora (1997); Bonora *et al.* (2005); Pirondi *et al.* (2006) proposed a CDM model where the analytical expression chosen for the damage dissipation potential leads to a nonlinear damage evolution as a function of the effective accumulated plastic strain. Alternatively, Brunig (2003); Brunig *et al.* (2008) proposed a CDM model in order to take the void volume fraction into account. Ayoub *et al.* (2011a) proposed a model using a CDM approach for the fatigue life prediction of styrene-butadiene rubber. Recently, Voyiadjis *et al.* (2012) adopted a thermodynamic approach for continuum damage healing mechanic (CDHM) where the non-associated viscoplasticity, viscodamage and viscohealing flow rules are used to capture the non-linear and irregular inelastic responses of glassy polymers. This approach where the damaged material is described globally at the level of a homogenised bulk element of the material is more attractive for the coupling with a viscoelastic-viscoplastic phenomenological constitutive model.

Furthermore, the nucleation and growth of micro-voids or micro-cracks during the deformation of filled polymeric materials under tensile loading induces a softening behaviour leading to the well known localisation problem of deformation in a narrow zone. The finite element simulation, using the classic continuum plasticity, is unable to describe the softening effect of such ductile materials (Pijaudier-Cabot *et al.*, 1988). This numerical problem leads to a mesh dependency on the mechanical response of the finite element simulations. This problem is due to the loss of ellipticity of the governing equilibrium equations in the static case and of hyperbolicity in the dynamic case. Many models are proposed in the literature to overcome the spurious mesh dependency. Needleman (1988); Loret and Prevost (1990) have shown that a viscoplastic formulation can overcome the mesh dependency phenomenon. The authors have shown that a length scale effect is naturally introduced by using a viscoplastic formulation. In the same way, Voyiadjis and Abed (2006) have high-

lighted the mesh dependency problem with a rate-independent analysis using a softening behaviour law on strips in tension with three different meshes. The mesh-sensitivity problem is solved by using a viscoplastic model formulated by the above authors. Nevertheless, as shown by (Besson *et al.*, 2001) for more localised deformation, the viscoplastic model does not overcome the mesh-dependent problem. In another way, the nonlocal continuum models were developed by introducing a nonlocal quantity which is defined by a spatial averaging of a quantity, and a material length scale is introduced through this radius of interaction. A revue of some integral-type nonlocal plasticity models is proposed by Jirásek and Rolshoven (2003) and de Sciarra (2008). An alternative regularising technique, which is closely related to the integral approach, is the "implicit" gradient formulation. Engelen *et al.* (2003) proposed an implicit gradient elastoplastic model where the damage is regularised by using a differential approximation of a nonlocal variable. A higher-order gradient terms of a local quantity can also be used in the yield function as a regularisation technique (De Borst and Múhlhaus, 1992; Voyiadjis *et al.*, 2010; Castrenze and Polizzotto, 2011). These kinds of models are called "explicit" gradient models. Unfortunately, the implementation of a nonlocal or gradient constitutive model in a commercial finite element code is not fulfilled in a simple manner. A very efficient approximation of a nonlocal quantity was proposed by Tvergaard and Needleman (1995). In their works, the rate form of the variable representing the void volume fraction of the Gurson model (GTN) is pondered by a coefficient depending on the average quantities calculated at previous time step. With this implementation, the local form of the constitutive equations is conserved and Tvergaard and Needleman concluded that the mesh sensitive problem have been totally overcome with their model. This approach is therefore very attractive to benefit of a nonlocal regularisation without modification of the classic formulation of a local continuum damage model.

2.4 Conclusions

The continuum mechanics, where the physical discontinuities of the material at the microstructural level, are described by a representative volume elements is a good way to develop a constitutive model for semi-crystalline polymeric materials. With this formulation the material parameters can be identified directly by classic experimental tests which is, in an industrial point of view, primordial. Furthermore, following this concept, the extension to the continuum damage mechanics has been carried out by many authors in a natural manner. The constitutive model developed by Ghorbel (2008) based on the general principles of thermodynamics with internal variables is attractive for polymer modelling. The intro-

duction of the pressure dependent yield criterion in this model describes the loading influence on the material response and following the "generalised standard material" concept, the compressibility of the material is assumed in an associative manner. More generally, a non-associated viscoplastic model is more suitable to describe the volume variation of the material. In this case, another viscoplastic dissipation potential is introduced in order to describe the viscoplastic strain rate. This approach is not included in the framework of the "generalised standard materials" but satisfy the principles of thermodynamic as well. In a phenomenological way, the coupled viscoelastic-vicoplastic model proposed by Miled *et al.* (2011), where a linear viscoelastic model is coupled with a viscoplastic formulation, is able to describe the time and rate dependent behaviour of polymeric materials. Finally, The spurious mesh dependency problem due to strain softening of mineral-filled polymer can be solved by using a viscoplastic formulation and a non local damage model. A nonlocal damage formulation based on the work of Tvergaard and Needleman (1995) seems to be the better approach in term of implementation and efficiency.
Consequently, in this thesis, a non-associated viscoelastic-viscoplastic model which possesses a pressure dependent yield surface stated in the framework of continuum mechanics (phenomenological model) coupled with a nonlocal damage model is developed in order to describe the behaviour of a mineral filled semi-crystalline polymer (polypropylene). An hypoelastic formulation using an objective stress rate is used to extend the constitutive model under finite strain framework with the retaining of material frame indifference during large deformations/rotations.

Chapter 3

Viscoelastic-viscoplastic constitutive model

POLYMER materials exhibit rate and time-dependent behaviour. The rate dependency can be observed by an increasing of the Young modulus and the yield stress at increasing strain rate, the long time to recover the zero-stress after loading of the material highlights the time dependent behaviour. Furthermore, particularly for filled polymers, the cavitation phenomenon causes the creation and growth of micro-voids and micro-cracks called damage accompanied by volume change during the deformation. In order to reproduce these phenomena, a viscoelastic-viscoplastic non-associated model coupled with damage which possesses a pressure dependent yield criterion and viscoplastic potential is developed in this chapter. Firstly, the linear viscoelastic Wiechert model, as well called generalised Maxwell model, is presented with its implementation in a finite element code under small strain framework. In a second time, the thermodynamical framework of the classic continuum plasticity is briefly presented in order to introduce the viscoelastic-viscoplastic constitutive model coupled with damage. The constitutive model and its implementation in implicit and explicit finite element codes under small strain framework are widely developed. The particular case of the plane stress viscoplastic stress return algorithm is detailed in order to use the developed model with continuum shell elements. An extension of the constitutive model under finite strain framework with its implementation in a finite element code based on a hypoelastic formulation is proposed in order to use the constitutive model with large strain finite element codes. Finally, with an eye to overcome the spurious mesh dependency caused by the simulation of material exhibiting softening, an integral type nonlocal extension of the proposed damage model with its implementation is presented at the end of the chapter.

3.1 Linear viscoelastic Wiechert model

The non-linear strain rate dependency and the multitude of relaxation times needed to model the polymer behaviour require a complex viscoelastic model. The linear Wiechert viscoelastic model is employed in the constitutive model in order to represent these complex phenomena. In this viscoelastic formulation, a finite number of separate Maxwell-elements are arranged in parallel with an elastic Hooke-element. This model is able to represent the realistic relaxation and the increase of the stiffness at increasing strain rates.

3.1.1 Basis of the linear viscoelasticity theory

A unique Maxwell element is a combination of Hooke and Newton-element in series (Fig. 3.1). In this simple element combination, the stress on each element is the same and equal to the imposed stress while the total strain is the sum of the strain of each element.

$$\sigma = \sigma^e = \sigma^v, \tag{3.1}$$

$$\varepsilon = \varepsilon^e + \varepsilon^v. \tag{3.2}$$

The superscripts $(.)^e$ and $(.)^v$ represent the Hooke (elastic) and the Newton (viscous) elements, respectively. For the Hooke element, the equation between the elastic strain ε^e and the elastic stress σ^e is a linear relation of the elastic constant E (Fig. 3.1), given by

$$\sigma^e = E\varepsilon^e. \tag{3.3}$$

The viscous stress σ^v of the Newton-element depends on the viscous strain rate $\dot{\varepsilon}^v$. These quantities are related linearly by the coefficient of viscosity μ (Fig. 3.1) such as

$$\sigma^v = \mu\dot{\varepsilon}^v. \tag{3.4}$$

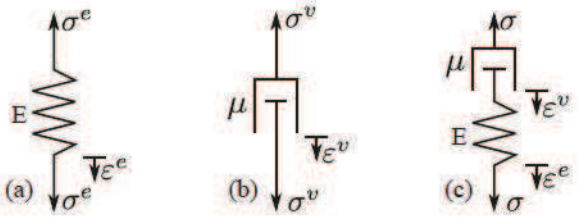

Figure 3.1: *Hooke-element (a), Newton-element (b) and Maxwell-element (c).*

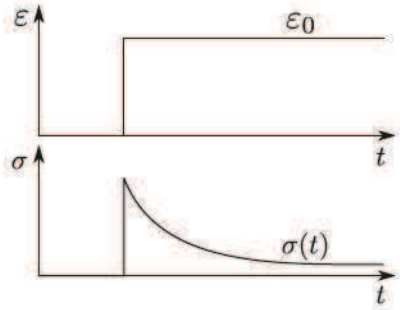

Figure 3.2: *Strain and stress histories in a relaxation test.*

By differentiating the strain equation (Eq. (3.2)) and combining with the relations of each element (Eqs. (3.3) and (3.4)), the fundamental relation of the strain of a Maxwell-element is given by

$$\dot{\varepsilon} = \dot{\varepsilon}^{e} + \dot{\varepsilon}^{v} = \frac{\dot{\sigma}}{E} + \frac{\sigma}{\mu}. \tag{3.5}$$

In a stress relaxation test, an imposed constant strain ε_0 is applied and as shown in Fig. 3.2, it results a time dependent stress. During this relaxation test, since the strain rate is null ($\dot{\varepsilon} = 0$), Eq. (3.5) becomes

$$\frac{\dot{\sigma}}{E} = -\frac{\sigma}{\mu}. \tag{3.6}$$

By introducing the relaxation time τ (i.e. $\tau = \frac{\mu}{E}$) in the previous differential equation (Eq. (3.6)), it results

$$\frac{d\sigma}{dt} = -\frac{\sigma}{\tau}. \tag{3.7}$$

The resolution of this differential equation (Eq. (3.7)) is done by integrating

$$\int_{\sigma_0}^{\sigma} \frac{d\sigma}{\sigma} = \int_{0}^{t} -\frac{t}{\tau} \mathrm{d}t \tag{3.8}$$

which leads to

$$\ln(\sigma) - \ln(\sigma_0) = -\frac{t}{\tau}. \tag{3.9}$$

The general expression of the stress at time t is therefore given by

$$\sigma(t) = \sigma_0 \exp\left(-\frac{t}{\tau}\right) \tag{3.10}$$

where σ_0 is the initial stress response of the Hooke-element loaded by ε_0 related by

$$\sigma_0 = E\varepsilon_0. \tag{3.11}$$

In the rheological Maxwell-element, the stress is therefore function of the strain and the time. Eq. (3.10) leads to the relaxation modulus which is defined by

$$E(t) = \frac{\sigma_0}{\varepsilon_0} \exp\left(\frac{-t}{\tau}\right) = E \exp\left(\frac{-t}{\tau}\right). \tag{3.12}$$

As shown in Eq. (3.10), for a time sufficiently large, the stress of a standard Maxwell-element relax as completely to zero. This is representative of fluid behaviour. The standard Maxwell-element is not able to describe properly a polymer behaviour. An Hooke-element is introduced in parallel to the Maxwell-element to overcome this deficiency (Fig. 3.3).This model is called Standard Linear Solid.

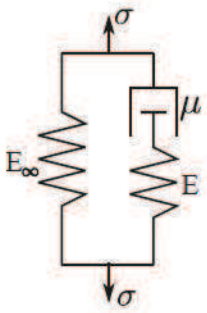

Figure 3.3: *Standard linear solid model.*

The added Hooke-element has a stiffness E_∞, so called long term Young modulus. In the Standard Linear Solid model, the strain on the Maxwell and Hooke elements in parallel are equal and the total stress is the sum of the Maxwell and Hooke elements as follows

$$\sigma = \sigma^e + \sigma_\infty = \sigma^v + \sigma_\infty \quad \text{and} \quad \varepsilon = \varepsilon^e + \varepsilon^v = \varepsilon_\infty. \tag{3.13}$$

σ_∞ and ε_∞ are the stress and the strain which are related with the long term Young modulus by

$$\sigma_\infty = E_\infty \varepsilon_\infty. \tag{3.14}$$

The stress at time t for the Standard Linear Solid model is obtained by combining Eq. (3.10) with the previous definitions,

$$\sigma(t) = E_\infty \varepsilon_0 + E\varepsilon_0 \exp\left(-\frac{t}{\tau}\right) = \sigma_\infty + \sigma_0 \exp\left(-\frac{t}{\tau}\right). \tag{3.15}$$

It appears clearly in the definition of the stress in the Standard Linear Solid model that the stress does not relax completely to zero for an imposed constant strain ε_0 (Fig. 3.4). The

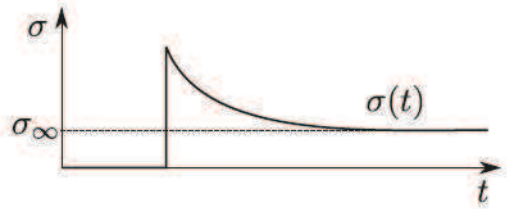

Figure 3.4: *Stress relaxation response of the Standard Linear Solid model.*

new relaxation modulus is therefore expressed as

$$E(t) = E_\infty + E \exp\left(\frac{-t}{\tau}\right). \tag{3.16}$$

Polymer materials does not relax with a single relaxation time. To incorporate this effect, a more realistic mathematical model was developed considering N Maxwell elements in parallel. By combining the N Maxwell elements with the parallel Hooke element introduced in the Standard Linear Solid model to obtain a long term stress response, it results the linear viscoelastic Wiechert model (i.e. generalised Maxwell model) (Fig. 3.5). The linear viscoelastic Wiechert model is used in the constitutive model to reproduce the viscoelastic behaviour of the polymeric material.

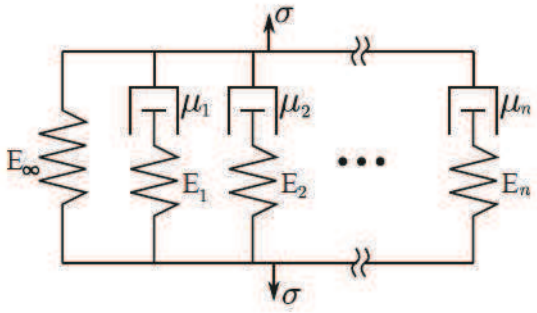

Figure 3.5: *Linear viscoelastic Wiechert model.*

In the Wiechert model, the strain on each element is the same as the total strain and the total stress is the sum of the individual stresses,

$$\varepsilon = \varepsilon_i \,, \quad \sigma = \sum_{i=1}^{N} \sigma_i. \tag{3.17}$$

Applying the superposition theorem, the expression of the stress at time t for the Wiechert model is given by

$$\sigma(t) = \left\{ E_\infty + \sum_{i=1}^{N} E_i \exp\left(-\frac{t}{\tau_i}\right) \right\} \varepsilon_0 \tag{3.18}$$

where E_i and τ_i are the Young modulus and the relaxation time of the i^{th} Maxwell element, respectively. The relaxation modulus can be expressed in the form of Prony series such as

$$E(t) = E_\infty + \sum_{i=1}^{N} E_i \exp\left(-\frac{t}{\tau_i}\right). \tag{3.19}$$

In the unique Maxwell element model or the linear standard model as well as the linear viscoelastic Wiechert model, the stress response is linearly function of the strain, with a time dependency, they are therefore included in the class of the linear viscoelastic models.

3.1.2 Boltzman superposition principle

In previous section, relaxation test is introduced and the relaxation modulus (Eq. (3.19)) is defined as the stress output for a constant strain input. Following the example of the relaxation test, to predict the output response with a non-constant input strain, it is possible to solve a general differential equation (in the one-dimensional case) but this approach can be a laborious task in many cases. The Boltzman superposition principle (i.e. integral) is able to be applied to stress analysis problems in two and three-dimensions where the stress or strain input varies with time. Considers $\sigma_1(t)$ at time t due to the application of strain increment $\Delta\varepsilon_1$ at a time ζ_1 previous to t, the stress produced by the strain history up to time t is given by

$$\sigma_1(t) = E(t - \zeta_1)\Delta\varepsilon_1. \tag{3.20}$$

In the same way, the stress $\sigma_2(t)$ at time t due to the application of strain increment $\Delta\varepsilon_2$ at a time ζ_2 previous to t is

$$\sigma_2(t) = E(t - \zeta_2)\Delta\varepsilon_2. \tag{3.21}$$

The total stress at time t, as proposed by Boltzmann, due to the both strain increments can be obtained by superposition of these two individual effects as follows

$$\sigma(t) = \sigma_1(t) + \sigma_2(t) = E(t - \zeta_1)\Delta\varepsilon_1 + E(t - \zeta_2)\Delta\varepsilon_2. \tag{3.22}$$

Since the integrals are summing operations, the expression of the stress at time t for various strain increments is given by

$$\sigma(t) = \int_0^t E(t - \zeta)d\varepsilon(\zeta) = \int_0^t E(t - \zeta)\frac{d\varepsilon(\zeta)}{d\zeta}d\zeta. \tag{3.23}$$

All events over the history of a viscoelastic material contribute to the current state of stress and strain, the lower limit of the hereditary integral is therefore often taken to be $-\infty$. The

expression of the stress at time t (Eq. (3.23)) becomes

$$\sigma(t) = \int_{-\infty}^{t} E(t-\zeta)\frac{\mathrm{d}\varepsilon(\zeta)}{\mathrm{d}\zeta}\mathrm{d}\zeta. \tag{3.24}$$

By considering a creep test, an analogous development of the output strain given by input variable stresses can demonstrate the following integral equation

$$\varepsilon(t) = \int_{-\infty}^{t} J(t-\zeta)\frac{\mathrm{d}\sigma(\zeta)}{\mathrm{d}\zeta}\mathrm{d}\zeta. \tag{3.25}$$

$J(t)$ is the creep compliance defined, in term of Prony series, as

$$J(t) = \frac{1}{E_\infty} + \sum_{i=1}^{N}\frac{1}{E_i}\exp\left(-\frac{t}{\tau_i}\right). \tag{3.26}$$

This uniaxial formulation of the hereditary integral can be extended to the three-dimensional case in a simple manner by replacing the uniaxial stress σ ans strain ε in Eq. (3.24) by the second order stress $\underset{\sim}{\boldsymbol{\sigma}}$ and strain $\underset{\sim}{\boldsymbol{\varepsilon}}$ tensors, it results

$$\underset{\sim}{\boldsymbol{\sigma}}(t) = \int_{-\infty}^{t} \underset{\approx}{\mathscr{R}}^{\mathrm{ve}}(t-\zeta) : \frac{\mathrm{d}\underset{\sim}{\boldsymbol{\varepsilon}}(\zeta)}{\mathrm{d}\zeta}\mathrm{d}\zeta \tag{3.27}$$

where $\underset{\approx}{\mathscr{R}}^{\mathrm{ve}}$ is the fourth order relaxation tensor. The symbol (:) represents the doubly contracted product of tensors. By analogy with the relaxation modulus of the Wiechert model (Eq. (3.19)), the fourth order relaxation tensor is expressed in term of Prony series as

$$\underset{\approx}{\mathscr{R}}^{\mathrm{ve}}(t) = \underset{\approx}{\mathscr{L}}^{\mathrm{ve}}_{\infty} + \sum_{i=1}^{N}\underset{\approx}{\mathscr{L}}^{\mathrm{ve}}_{i}\exp\left(-\frac{t}{\tau_i}\right). \tag{3.28}$$

$\underset{\approx}{\mathscr{L}}^{\mathrm{ve}}_{\infty}$ is the fourth order long-term elastic tensor defined by

$$\underset{\approx}{\mathscr{L}}^{\mathrm{ve}}_{\infty} = 2G_\infty \underset{\approx}{\mathbf{I}}_{\mathrm{d}} + K_\infty \underset{\sim}{\mathbf{I}} \otimes \underset{\sim}{\mathbf{I}}. \tag{3.29}$$

$\underset{\approx}{\mathbf{I}}_{\mathrm{d}}$ is the deviatoric projection tensor such as

$$\underset{\approx}{\mathbf{I}}_{\mathrm{d}} = \underset{\approx}{\mathbf{I}}_{\mathrm{s}} - \frac{1}{3}\underset{\sim}{\mathbf{I}} \otimes \underset{\sim}{\mathbf{I}} \tag{3.30}$$

where $\underset{\approx}{\mathbf{I}}_{\mathrm{s}}$ and $\underset{\sim}{\mathbf{I}}$ are the fourth order symmetric identity and second order identity tensors. The symbol $\otimes$ represents the tensor product. As in classic elasticity, the bulk and shear

long-term moduli, respectively, G_∞ and K_∞ are given by

$$G_\infty = \frac{E_\infty}{2(1+\nu)}\,, \quad K_\infty = \frac{E_\infty}{3(1-2\nu)} \tag{3.31}$$

where ν is the Poisson ratio. In the same way, the fourth order elastic stiffness tensor of the i^{th} Hooke element including in the i^{th} Maxwell element is defined by

$$\underset{\approx}{\mathscr{L}}_i^{\text{ve}} = 2G_i \underset{\approx}{\mathbf{I}}_{\text{d}} + K_i \underset{\sim}{\mathbf{I}} \otimes \underset{\sim}{\mathbf{I}}. \tag{3.32}$$

The respective shear and bulk moduli, G_i and K_i arise from

$$G_i = \frac{E_i}{2(1+\nu)}\,, \quad K_i = \frac{E_i}{3(1-2\nu)}. \tag{3.33}$$

3.1.3 Implementation of the linear Wiechert viscoelastic model

In the aim to describe the implementation of the linear Wiechert viscoelastic model into an implicit finite element code, the unidimensional case is firstly considered. In the unidimensional case, the relaxation modulus of the Wiechert viscoelastic model expressed in the form of Prony series (Eq. (3.19)) is given by

$$E(t) = E_\infty + \sum_{i=1}^{N} E_i \exp\left(-\frac{t}{\tau_i}\right). \tag{3.34}$$

The long term modulus E_∞ is therefore a constant term. In the following implementation, the relaxation modulus is normalized by the long term modulus. The normalized relaxation modulus $\Xi(t)$ is then defined by

$$\Xi(t) = \frac{E(t)}{E_\infty} = 1 + \sum_{i=1}^{N} \Xi_i \exp\left(-\frac{t}{\tau_i}\right). \tag{3.35}$$

Recalling the Boltzman hereditary integral for the current viscoelastic model in unidimensional condition (Eq. (3.24)) and taking E_∞like time independent parameter into account, the stress of the Wierchet model is calculated such as

$$\begin{aligned}
\sigma(t) &= \int_{-\infty}^{t} E(t-\zeta)\frac{\mathrm{d}\varepsilon(\zeta)}{\mathrm{d}\zeta}\mathrm{d}\zeta, \\
&= \int_{-\infty}^{t} E_\infty \frac{\mathrm{d}\varepsilon(\zeta)}{\mathrm{d}\zeta}\mathrm{d}\zeta + \int_{-\infty}^{t} \sum_{i=1}^{N} E_i \exp\left(-\frac{t-\zeta}{\tau_i}\right)\frac{\mathrm{d}\varepsilon(\zeta)}{\mathrm{d}\zeta}\mathrm{d}\zeta, \\
&= E_\infty \varepsilon(t) + \sum_{i=1}^{N} \int_{-\infty}^{t} E_i \exp\left(-\frac{t-\zeta}{\tau_i}\right)\frac{\mathrm{d}\varepsilon(\zeta)}{\mathrm{d}\zeta}\mathrm{d}\zeta,
\end{aligned}$$

$$= \sigma_\infty(t) + \sum_{i=1}^{N} h_i(t) \tag{3.36}$$

with

$$h_i(t) = \int_{-\infty}^{t} E_i \exp\left(-\frac{t-\zeta}{\tau_i}\right) \frac{\mathrm{d}\varepsilon(\zeta)}{\mathrm{d}\zeta} \mathrm{d}\zeta. \tag{3.37}$$

$h_i(t)$ is the stress response of the parallel Maxwell elements with zero-stress when the time tends towards infinity, i.e.

$$\lim_{t\to\infty} h_i(t) = 0. \tag{3.38}$$

The strain in all the Maxwell elements in parallel with the Hooke-element are equal. Furthermore, the strain component of the Hooke element does not depend on time. The following relation can therefore be assumed

$$\varepsilon(t) = \varepsilon_\infty(t) = \frac{\sigma_\infty}{E_\infty}. \tag{3.39}$$

Combining Eq. (3.39) with the normalized modulus defined in Eq. (3.35) and substituting into Eq. (3.37), the variable $h_i(t)$ can be expressed as

$$h_i(t) = \int_{-\infty}^{t} \Xi_i \exp\left(-\frac{t-\zeta}{\tau_i}\right) \frac{\mathrm{d}\sigma_\infty(\zeta)}{\mathrm{d}\zeta} \mathrm{d}\zeta. \tag{3.40}$$

For the numerical implementation of the viscoelastic model into a finite element code where the stress response is known at the time t_n in the time interval $[t_n,\ t_{n+1}]$, the aim is to compute the values of the variables at time t_{n+1}. For the following expressions, the current time step $\Delta t = t_{n+1} - t_n$ is defined. Using the multiplicative split of the exponential expression and the additive properties of the integrals, Eq. (3.40) becomes

$$\begin{aligned}
h_i(n+1) &= \Xi_i \int_0^{t_{n+1}} \exp\left(-\frac{t_{n+1}-\zeta}{\tau_i}\right) \frac{\mathrm{d}\sigma_\infty(\zeta)}{\mathrm{d}\zeta} \mathrm{d}\zeta, \\
&= \Xi_i \int_0^{t_n} \exp\left(-\frac{t_n + \Delta t - \zeta}{\tau_i}\right) \frac{\mathrm{d}\sigma_\infty(\zeta)}{\mathrm{d}\zeta} \mathrm{d}\zeta + \Xi_i \int_{t_n}^{t_{n+1}} \exp\left(-\frac{t_{n+1}-\zeta}{\tau_i}\right) \frac{\mathrm{d}\sigma_\infty(\zeta)}{\mathrm{d}\zeta} \mathrm{d}\zeta, \\
&= \Xi_i \exp\left(-\frac{\Delta t}{\tau_i}\right) \int_0^{t_n} \exp\left(-\frac{t_n-\zeta}{\tau_i}\right) \frac{\mathrm{d}\sigma_\infty(\zeta)}{\mathrm{d}\zeta} \mathrm{d}\zeta + \Xi_i \int_{t_n}^{t_{n+1}} \exp\left(-\frac{t_{n+1}-\zeta}{\tau_i}\right) \frac{\mathrm{d}\sigma_\infty(\zeta)}{\mathrm{d}\zeta} \mathrm{d}\zeta, \\
&= \exp\left(-\frac{\Delta t}{\tau_i}\right) h_i(n) + \Xi_i \int_{t_n}^{t_{n+1}} \exp\left(-\frac{t_{n+1}-\zeta}{\tau_i}\right) \frac{\mathrm{d}\sigma_\infty(\zeta)}{\mathrm{d}\zeta} \mathrm{d}\zeta.
\end{aligned} \tag{3.41}$$

The transition between differential values and discrete time steps is done following

$$\frac{d\sigma_\infty(\zeta)}{d\zeta} = \lim_{\Delta t \to 0} \frac{\sigma_{\infty\, n+1} - \sigma_{\infty\, n}}{\Delta t}. \tag{3.42}$$

Substituting Eq. (3.42) into Eq. (3.41) yields to

$$h_{i\, n+1} = \exp\left(-\frac{\Delta t}{\tau_i}\right) h_{i\, n} + \Xi_i \int_{t_n}^{t_{n+1}} \exp\left(-\frac{t_{n+1} - \zeta}{\tau_i}\right) \frac{\sigma_{\infty\, n+1} - \sigma_{\infty\, n}}{\Delta t} \mathrm{d}\zeta. \tag{3.43}$$

By integrating the previous relation, the exact regressive formula for the current value of the stress quantities h_i is given by

$$h_{i\, n+1} = \exp\left(-\frac{\Delta t}{\tau_i}\right) h_{i\, n} + \Xi_i \frac{1 - \exp\left(-\frac{\Delta t}{\tau_i}\right)}{\frac{\Delta t}{\tau_i}} \left[\sigma_{\infty\, n+1} - \sigma_{\infty\, n}\right]. \tag{3.44}$$

Combining Eq. (3.44) with the formulation of the stress for the linear viscoelastic Wierchet model (Eq. (3.36)), the expression of the stress at time t_{n+1} is therefore given by

$$\sigma_{n+1} = E_\infty \varepsilon_{n+1} + \sum_{i=1}^{N} h_{i\, n+1}. \tag{3.45}$$

The extension of the stress formulation to a three-dimensional model is fulfilled by introducing the tensor quantities. The current stress σ_{n+1}, strain ε_{n+1}, long-term modulus E_∞ and the stress quantities $h_{i\, n+1}$ are replaced by the stress tensor $\underset{\sim}{\boldsymbol{\sigma}}_{n+1}$, the strain tensor $\underset{\sim}{\boldsymbol{\varepsilon}}_{n+1}$, the fourth order long-term elastic stiffness tensor $\underset{\approx}{\mathscr{L}}^{\mathrm{e}}_{\infty}$ and the second order tensors $\underset{\sim}{\mathbf{h}}_{i\, n+1}$, respectively. The expression of the stress for the viscoelastic model is also given by

$$\underset{\sim}{\boldsymbol{\sigma}}_{n+1} = \underset{\approx}{\mathscr{L}}^{\mathrm{ve}}_{\infty} : \underset{\sim}{\boldsymbol{\varepsilon}}_{n+1} + \sum_{i=1}^{N} \underset{\sim}{\mathbf{h}}_{i\, n+1} \tag{3.46}$$

where $\underset{\sim}{\mathbf{h}}_{i\, n+1}$ is defined as

$$\underset{\sim}{\mathbf{h}}_{i\, n+1} = \exp\left(-\frac{\Delta t}{\tau_i}\right) \underset{\sim}{\mathbf{h}}_{i\, n} + \Xi_i \frac{1 - \exp\left(-\frac{\Delta t}{\tau_i}\right)}{\frac{\Delta t}{\tau_i}} \left[\underset{\sim}{\boldsymbol{\sigma}}_{\infty\, n+1} - \underset{\sim}{\boldsymbol{\sigma}}_{\infty\, n}\right]. \tag{3.47}$$

In order to implement the linear viscoelastic Wiechert model in an implicit finite element code, the consistent tangent modulus

$$\underset{\approx}{\mathscr{L}}^{\mathrm{ve}} = \frac{\partial \underset{\sim}{\boldsymbol{\sigma}}}{\partial \underset{\sim}{\boldsymbol{\varepsilon}}} = \left\{1 + \sum_{j=1}^{N} \frac{1 - \exp\left(\frac{\Delta t}{\tau_j}\right)}{\frac{\Delta t}{\tau_j}}\right\} \underset{\approx}{\mathscr{L}}^{\mathrm{ve}}_{\infty} \tag{3.48}$$

is computed as the derivative of the current stress with respect to the current strain (Simo and Taylor, 1985).

3.2 Thermodynamic formulation in elastoplasticity

In this section, the thermodynamical framework of the classic continuum plasticity is briefly presented in order to introduce the constitutive viscoelastic-viscoplastic model developed in the next sections. The following developments are formulated within the framework of the small strain theory. Under this hypothesis, the standard definition of infinitesimal strain tensor $\underset{\sim}{\boldsymbol{\varepsilon}}$ is the symmetric part of the displacement gradient operator $\nabla\vec{u}$, i.e

$$\underset{\sim}{\boldsymbol{\varepsilon}} = \frac{1}{2}\left[\nabla\vec{u} + \nabla\vec{u}^{\mathrm{T}}\right]. \tag{3.49}$$

Furthermore, the elastic behaviour is independent of the plastic internal state variables. The total strain tensor can therefore be additively decomposed into an elastic (recoverable) $\underset{\sim}{\boldsymbol{\varepsilon}}^{\mathrm{e}}$ and plastic $\underset{\sim}{\boldsymbol{\varepsilon}}^{\mathrm{p}}$ (unrecoverable) components, such as

$$\underset{\sim}{\boldsymbol{\varepsilon}} = \underset{\sim}{\boldsymbol{\varepsilon}}^{\mathrm{e}} + \underset{\sim}{\boldsymbol{\varepsilon}}^{\mathrm{p}}. \tag{3.50}$$

In the thermodynamic of irreversible process, two potentials are introduced. The state potential, written as a function of the state variables which defines the state laws. The other potential is the dissipation potential written with the associated variables of the state variables. The dissipative potential with its associated variables accounts to derive the evolution equations of the state variables. The thermodynamic based constitutive equations are therefore represented by local values of some state variables. The state variables are either observable variables (e.g. temperature, total strain) or internal variables. The internal variables are used in order to take the loading history into account when unrecoverable phenomenon occurs (e.g. plastic strain, damage). The Helmholtz free energy is considered as the thermodynamic state potential depending on the state variables. In the framework of isotropic-hardening elastoplasticity, the Helmholtz free energy Ψ depends on the total elastic and plastic strain, the temperature T and the hardening variable r. Hence, the Helmholtz free energy Ψ is expressed by

$$\Psi = \Psi\left(\underset{\sim}{\boldsymbol{\varepsilon}},\ \underset{\sim}{\boldsymbol{\varepsilon}}^{\mathrm{p}},\ r,\ T\right). \tag{3.51}$$

By following the decomposition of the strain tensor, the Helmholtz free energy becomes

$$\Psi = \Psi\left([\underset{\sim}{\varepsilon} - \underset{\sim}{\varepsilon}^{p}],\ r,\ T\right) = \Psi\left(\underset{\sim}{\varepsilon}^{e},\ r,\ T\right), \tag{3.52}$$

which leads to

$$\frac{\partial \Psi}{\partial \underset{\sim}{\varepsilon}^{e}} = \frac{\partial \Psi}{\partial \underset{\sim}{\varepsilon}} = -\frac{\partial \Psi}{\partial \underset{\sim}{\varepsilon}^{p}}. \tag{3.53}$$

The splitting between the elastic and plastic behaviour allows to write the Helmholtz free energy as

$$\Psi = \Psi_{e}\left(\underset{\sim}{\varepsilon}^{e},\ T\right) + \Psi_{p}\left(r,\ T\right). \tag{3.54}$$

The time derivative of Eq. (3.51) with respect to its state variables is given by

$$\dot{\Psi} = \frac{\partial \Psi}{\partial \underset{\sim}{\varepsilon}^{e}} \dot{\underset{\sim}{\varepsilon}}^{e} + \frac{\partial \Psi}{\partial r}\dot{r} + \frac{\partial \Psi}{\partial T}\dot{T}. \tag{3.55}$$

The second law of thermodynamics states that the change in entropy is always positive and it can be expressed by an inequality called Clausius-Duhem inequality. The entropy is a energy variation associated to a temperature variation. Following the second laws of thermodynamics, the local form of the Clausius-Duhem inequality under non-isothermal condition can be written as follows

$$\underset{\sim}{\sigma} : \dot{\underset{\sim}{\varepsilon}} - \rho\left(\dot{\Psi} + s\dot{T}\right) - \vec{q}\frac{\nabla T}{T} \geqslant 0 \tag{3.56}$$

where ρ is the material density, $\vec{q}$ is heat flux vector, ∇T is the temperature gradient, s is the specific entropy per unit of mass, $\underset{\sim}{\sigma}$ is the Cauchy stress tensor and $\dot{\underset{\sim}{\varepsilon}}$ is the total strain rate tensor. Substituting Eq. (3.55) into Eq. (3.56), the local form of the Clausius-Duhem inequality becomes

$$\left(\underset{\sim}{\sigma} - \rho\frac{\partial \Psi}{\partial \underset{\sim}{\varepsilon}^{e}}\right) : \dot{\underset{\sim}{\varepsilon}}^{e} + \underset{\sim}{\sigma} : \dot{\underset{\sim}{\varepsilon}}^{p} - \rho\frac{\partial \Psi}{\partial r}\dot{r} - \rho\left(\frac{\partial \Psi}{\partial T} + s\right)\dot{T} - \vec{q}\frac{\nabla T}{T} \geqslant 0. \tag{3.57}$$

Considering an elastic transformation at constant temperature $\left(\dot{T} = 0\right)$ and uniform $\left(\nabla T = 0\right)$ which does not change the plastic strain $\left(\dot{\underset{\sim}{\varepsilon}}^{p} = 0\right)$ and the internal variables $\left(\dot{r} = 0\right)$. The Clausius-Duhem inequality which needs to be verified for all $\underset{\sim}{\varepsilon}^{e}$ yields to

$$\underset{\sim}{\sigma} - \rho\frac{\partial \Psi}{\partial \underset{\sim}{\varepsilon}^{e}} = 0. \tag{3.58}$$

The equality now verified, considering a uniform thermal transformation such as $\nabla T = 0, \dot{\underset{\sim}{\varepsilon}}^{\mathrm{p}} = 0, \dot{r} = 0$, the Clausius-Duhem inequality is satisfed only if

$$s + \frac{\partial \Psi}{\partial T} = 0. \tag{3.59}$$

The two above equations (Eqs. (3.58) and (3.59)) leads to the thermoelasticity laws, i.e.

$$\underset{\sim}{\sigma} = \rho \frac{\partial \Psi}{\partial \underset{\sim}{\varepsilon}^{\mathrm{e}}}, \tag{3.60}$$

$$s = -\frac{\partial \Psi}{\partial T}. \tag{3.61}$$

By analogy with the previous relations, the thermodynamic force associated to the internal variable r is given by

$$R = \rho \frac{\partial \Psi}{\partial r}. \tag{3.62}$$

$\underset{\sim}{\sigma}$, s and R are the thermodynamic conjugate forces corresponding to the state variables $\underset{\sim}{\varepsilon}^{\mathrm{e}}$, T and r. The above equalities (Eqs. (3.60)-(3.62)) are called state laws. The thermodynamic state potential is not a perceptible quantity, only the internal variables are measurable. Experimental tests are therefore needed for the establishment of the state laws. Rewriting the Clausius-Duhem inequality (Eq. (3.57)) with the thermodynamic state laws (Eqs. (3.60)-(3.62), it results the rate of the total dissipation power $\mathscr{D}^{\mathrm{mech}}$ such as

$$\mathscr{D}^{\mathrm{mech}} = \underset{\sim}{\sigma} : \dot{\underset{\sim}{\varepsilon}}^{\mathrm{p}} - R\dot{r} - \vec{q}\frac{\nabla T}{T} \geqslant 0. \tag{3.63}$$

Decoupling the mechanical (in this case only the plastic dissipation is considered) and thermal dissipation, $\mathscr{D}^{\mathrm{p}}$ and $\mathscr{D}^{\mathrm{th}}$, respectively, as follows

$$\mathscr{D}^{\mathrm{mech}} = \mathscr{D}^{\mathrm{p}} + \mathscr{D}^{\mathrm{th}}, \tag{3.64}$$

the plastic dissipation power $\mathscr{D}^{\mathrm{p}}$ is defined as

$$\mathscr{D}^{\mathrm{p}} = \underset{\sim}{\sigma} : \dot{\underset{\sim}{\varepsilon}}^{\mathrm{p}} - R\dot{r} \geqslant 0, \tag{3.65}$$

the thermal dissipation power $\mathscr{D}^{\mathrm{th}}$ is given by

$$\mathscr{D}^{\mathrm{th}} = -\vec{q}\frac{\nabla T}{T} \geqslant 0. \tag{3.66}$$

In the framework of an iso-thermal process, only the plastic dissipation power is considered, the total dissipation power becomes

$$\mathscr{D}^{\text{mech}} = \mathscr{D}^{\text{p}}. \tag{3.67}$$

In order to describe the evolution of the state variables, a dissipation potential Θ which is a continuous and convex scalar valued function of the flux variables, is defined as follows*

$$\Theta = \Theta(\dot{\underset{\sim}{\boldsymbol{\varepsilon}}}^{\text{p}}, \dot{r}). \tag{3.68}$$

This potential is convex, positive and null at the origin in the space of the flux variables $\dot{\underset{\sim}{\boldsymbol{\varepsilon}}}^{\text{p}}$ and $\dot{r}$. By using the Legendre transformation, the potential Θ^* dual to Θ which is function of the conjugate forces is obtained

$$\Theta^* = \Theta^*(\underset{\sim}{\boldsymbol{\sigma}}, R). \tag{3.69}$$

The potential Θ^* can be decoupled into different potentials (i.e. plastic, damage ...), in this case only the plasticity is considered

$$\Theta^* = F^{\text{p}}(\underset{\sim}{\boldsymbol{\sigma}}, R). \tag{3.70}$$

In order to define the evolution of the plastic strain rate $\dot{\underset{\sim}{\boldsymbol{\varepsilon}}}^{\text{p}}$ and the hardening flux $\dot{r}$, an objective function γ^* with its Lagrangian multiplier $\dot{\lambda}$ is defined such as

$$\gamma^* = \mathscr{D}^{\text{mech}} - \dot{\lambda} F^{\text{p}}. \tag{3.71}$$

The previous objective function needs to be maximised by using the following conditions

$$\frac{\partial \gamma^*}{\partial \underset{\sim}{\boldsymbol{\sigma}}} = 0, \tag{3.72}$$

$$\frac{\partial \gamma^*}{\partial R} = 0. \tag{3.73}$$

Substituting Eq. (3.71) into the above relations, the corresponding flow laws of $\dot{\underset{\sim}{\boldsymbol{\varepsilon}}}^{\text{p}}$ and $\dot{r}$ are therefore obtained

$$\dot{\underset{\sim}{\boldsymbol{\varepsilon}}}^{\text{p}} = \dot{\lambda} \frac{\partial F^{\text{p}}}{\partial \underset{\sim}{\boldsymbol{\sigma}}}, \tag{3.74}$$

*In more complex cases, the state variables can be introduced in the dissipation potential.

$$\dot{r} = -\dot{\lambda}\frac{\partial F^{\mathrm{p}}}{\partial R}. \tag{3.75}$$

From the expression of the dual potential Θ^*, the normality rules are therefore obtained. To respect the second law of thermodynamics, the potentials Θ and Θ^* need to be convex non-negative and null at the start of the process. The normality rules are enough to satisfy the second law of thermodynamics. The materials for which the evolution of the state variables are given by the normality rules from the dissipation potential are called "generalised standard materials". For these kinds of materials, the plastic dissipation potential defines the yield surface and the plastic flow direction, the plasticity is defined as associated.
In the framework of associated elastoplasticity with linear isotropic hardening, the Helmholtz free energy potential expressed in analytical form of each internal variables takes the following form

$$\rho\Psi = \frac{1}{2}\underset{\approx}{\mathscr{L}}^{\mathrm{e}}\left(\underset{\sim}{\boldsymbol{\varepsilon}} - \underset{\sim}{\boldsymbol{\varepsilon}}^{\mathrm{p}}\right)^2 + \frac{1}{2}Hr^2, \tag{3.76}$$

where H is a material constant (plastic hardening) and $\underset{\approx}{\mathscr{L}}^{\mathrm{e}}$ is the fourth order elastic stiffness tensor given by

$$\underset{\approx}{\mathscr{L}}^{\mathrm{e}} = 2G\underset{\approx}{\mathbf{I}}_{\mathrm{d}} + K\underset{\sim}{\mathbf{I}} \otimes \underset{\sim}{\mathbf{I}}. \tag{3.77}$$

The bulk K and shear G moduli are given by

$$G = \frac{E}{2(1+\nu)} \text{ and } K = \frac{E}{3(1-2\nu)} \tag{3.78}$$

where E and ν are the Young modulus and the Poisson ratio, respectively. The thermodynamic state laws arising from the thermodynamic potential defined by Eq. (3.76) are given by using Eqs. (3.60) and (3.61) such as

$$\underset{\sim}{\boldsymbol{\sigma}} = \frac{\partial \Psi}{\partial \underset{\sim}{\boldsymbol{\varepsilon}}^{\mathrm{e}}} = \underset{\approx}{\mathscr{L}}^{\mathrm{e}}\left(\underset{\sim}{\boldsymbol{\varepsilon}} - \underset{\sim}{\boldsymbol{\varepsilon}}^{\mathrm{p}}\right), \tag{3.79}$$

$$R = \frac{\partial \Psi}{\partial r} = Hr. \tag{3.80}$$

Eq. (3.79) is the generalised Hooke law of an linear elastic material and Eq. (3.80) describes the change in size of the yield surface corresponding to the isotropic hardening. In order to be consistent and to satisfy the normality rules of the thermodynamics, the dissipation potential Θ^* is postulated as

$$\Theta^* = F^{\mathrm{p}} = \sqrt{\tfrac{3}{2}\underset{\sim}{\mathbf{S}} : \underset{\sim}{\mathbf{S}}} - \sigma_t - R(r). \tag{3.81}$$

σ_t is the yield stress obtained from simple uniaxial tensile test and $\underset{\sim}{\mathbf{S}}$ is the second order deviatoric stress tensor such as

$$\underset{\sim}{\mathbf{S}} = \underset{\approx}{\mathbf{I}}_{\mathrm{d}} : \underset{\sim}{\boldsymbol{\sigma}}. \tag{3.82}$$

This plastic dissipative potential corresponds to the well known von Mises yield surface used in the von Mises elastoplastic model. Introducing Eqs. (3.74) and (3.75) into Eq. (3.81), the evolutions of the internal variables, obtained by the normality rules of the generalised standard materials, are defined as

$$\dot{\underset{\sim}{\boldsymbol{\varepsilon}}}^{\mathrm{p}} = \dot{\lambda} \frac{\partial F^{\mathrm{p}}}{\partial \underset{\sim}{\boldsymbol{\sigma}}} = \dot{\lambda} \frac{3}{2} \frac{\underset{\sim}{\mathbf{S}}}{\sigma_e}, \tag{3.83}$$

$$\dot{r} = -\dot{\lambda} \frac{\partial F^{\mathrm{p}}}{\partial R} = \dot{\lambda}. \tag{3.84}$$

σ_e is the von Mises equivalent stress defined by

$$\sigma_e = \sqrt{\frac{3}{2} \underset{\sim}{\mathbf{S}} : \underset{\sim}{\mathbf{S}}}. \tag{3.85}$$

To complete the description of the associated elastoplasticity, the equivalent plastic strain rate $\dot{\kappa}$ is defined by

$$\dot{\kappa} = \sqrt{\tfrac{2}{3} \dot{\underset{\sim}{\boldsymbol{\varepsilon}}}^{\mathrm{p}} : \dot{\underset{\sim}{\boldsymbol{\varepsilon}}}^{\mathrm{p}}} = \sqrt{\frac{2}{3} \left(\dot{\lambda} \frac{3}{2} \frac{\underset{\sim}{\mathbf{S}}}{\sigma_e} : \dot{\lambda} \frac{3}{2} \frac{\underset{\sim}{\mathbf{S}}}{\sigma_e} \right)} = \frac{\dot{\lambda}}{\sigma_e} \sqrt{\frac{2}{3} \underset{\sim}{\mathbf{S}} : \underset{\sim}{\mathbf{S}}} = \dot{\lambda} = \dot{r}. \tag{3.86}$$

Assuming that the yield surface F^{p} is the unique path possible in plastic process, the stress states $\underset{\sim}{\boldsymbol{\sigma}}$ such that $F^{\mathrm{p}} = \sigma_e - \sigma_t - R(\kappa) > 0$ are not admissible. Furthermore, when the stress states lie in the elastic domain, i.e. $F^{\mathrm{p}} = \sigma_e - \sigma_t - R(\kappa) < 0$, no plastic deformations take place (i.e. $\dot{\underset{\sim}{\boldsymbol{\varepsilon}}}^{\mathrm{p}} = 0, \dot{\lambda} = 0$). Consequently, the plastic loading (i.e. $\dot{\underset{\sim}{\boldsymbol{\varepsilon}}}^{\mathrm{p}} \neq 0$) is assumed uniquely when the yield surface vanish (i.e. $F^{\mathrm{p}} = 0$). The yield surface is therefore defined as always negative or null,

$$F^{p}(\underset{\sim}{\boldsymbol{\sigma}}, \kappa) \leqslant 0. \tag{3.87}$$

Under plastic loading, the plastic strain rate tensor $\dot{\underset{\sim}{\boldsymbol{\varepsilon}}}^{\mathrm{p}}$ can be positive (stretching) in tension and negative (compressive) in compression but the plastic multiplier $\dot{\lambda}$ is always non-negative,

$$\dot{\lambda} \geqslant 0, \tag{3.88}$$

and satisfies the complementarity condition

$$\dot{\lambda} F^{\mathrm{p}} = 0. \tag{3.89}$$

Eqs. (3.87)-(3.89) define the so-called Kuhn-Tucker loading/unloading conditions of the elastoplastic model, such as

$$F^p(\underset{\sim}{\sigma}, \kappa) \leqslant 0, \quad \dot{\lambda} \geqslant 0, \quad \dot{\lambda} F^p = 0. \tag{3.90}$$

3.3 Non-associated viscoelastic-viscoplastic model coupled with damage

In this section, the constitutive model which satisfy the second law of thermodynamics in Clausius-Duhem inequality form is presented. The proposed model is able to reproduce the time and rate dependency of polymer materials by using a coupled viscoelastic-viscoplastic formulation. In order to take the pressure sensitivity on the behaviour into account, the Raghava yield criterion is introduced in the constitutive model. The non-isochoric deformation of polymer materials is modelled with the non-associated viscoplastic flow rule. Moreover, the volume change of the material which is not similar for positive and negative hydrostatic pressure have motived the development of a new viscoplastic dissipation potential which reproduces these phenomena. A continuum damage model is introduced in the constitutive formulation as well, in order to reproduce the softening behaviour caused by the creation and growth of micro-voids and micro-cracks.

3.3.1 Thermodynamic framework

The viscoelastic-viscoplastic constitutive model is formulated within the framework of the small strain theory and isothermal process. Under this hypothesis, the total strain tensor $\underset{\sim}{\varepsilon}$ is additively decomposed into a viscoelastic part $\underset{\sim}{\varepsilon}^{ve}$ and a viscoplastic one $\underset{\sim}{\varepsilon}^{vp}$ such as

$$\underset{\sim}{\varepsilon} = \underset{\sim}{\varepsilon}^{ve} + \underset{\sim}{\varepsilon}^{vp}. \tag{3.91}$$

In order to model the viscoelastic-viscoplastic behaviour with non-linear isotropic hardening coupled with isotropic damage and volume change (compaction-dilatation), the observable state variable is the total strain tensor $\underset{\sim}{\varepsilon}$ and the internal state variables which reproduce the history of the material are: the viscoplastic strain tensor $\underset{\sim}{\varepsilon}^{vp}$, the hardening variable κ which is the equivalent viscoplastic strain and the damage variable D[†]. The Helmholtz free energy Ψ is therefore assumed to be function of the total strain tensor $\underset{\sim}{\varepsilon}$, the viscoplastic strain tensor $\underset{\sim}{\varepsilon}^{vp}$, the viscoplastic equivalent strain κ and the damage D.

[†]The definition of the damage variable D is given in the next section

The Helmholtz free energy Ψ is also defined by

$$\Psi = \Psi\left(\underset{\sim}{\varepsilon}, \underset{\sim}{\varepsilon}^{vp}, \kappa, D\right) = \Psi\left(\underset{\sim}{\varepsilon}^{ve}, \kappa, D\right). \tag{3.92}$$

Furthermore, the Helmholtz free energy Ψ may be split in a viscoelastic Ψ_{ve} and viscoplastic part Ψ_{vp} such as

$$\Psi = \Psi_{ve}(\underset{\sim}{\varepsilon}^{ve}, D) + \Psi_{vp}(\kappa). \tag{3.93}$$

In the viscoplasticity theory, the equivalent viscoplastic strain κ is expressed as

$$\kappa = \sqrt{\tfrac{2}{3}\underset{\sim}{\varepsilon}^{vp} : \underset{\sim}{\varepsilon}^{vp}}. \tag{3.94}$$

The time derivative of the Helmholtz free energy (Eq. (3.92)) equation is given by

$$\dot{\Psi} = \frac{\partial \Psi}{\partial \underset{\sim}{\varepsilon}^{e}} \dot{\underset{\sim}{\varepsilon}}^{e} + \frac{\partial \Psi}{\partial \kappa}\dot{\kappa} + \frac{\partial \Psi}{\partial D}\dot{D}. \tag{3.95}$$

Respecting the second law of thermodynamics, considering an isothermal process, the Clausius-Duhem inequality becomes

$$\underset{\sim}{\sigma} : \dot{\underset{\sim}{\varepsilon}} - \rho\dot{\Psi} \geqslant 0. \tag{3.96}$$

Substituting Eq. (3.95) into Eq. (3.96) the Clausius-Duhem inequality yields to

$$\left(\underset{\sim}{\sigma} - \rho\frac{\partial \Psi}{\partial \underset{\sim}{\varepsilon}^{e}}\right)\dot{\underset{\sim}{\varepsilon}}^{e} + \underset{\sim}{\sigma} : \dot{\underset{\sim}{\varepsilon}}^{vp} - \rho\frac{\partial \Psi}{\partial \kappa}\dot{\kappa} - \rho\frac{\partial \Psi}{\partial D}\dot{D} \geqslant 0. \tag{3.97}$$

The thermodynamic conjugate force for each variable is obtained as follows

$$\underset{\sim}{\sigma} = \rho\frac{\partial \Psi}{\partial \underset{\sim}{\varepsilon}^{e}}, \tag{3.98}$$

$$R = \rho\frac{\partial \Psi}{\partial \kappa}, \tag{3.99}$$

$$Y = \rho\frac{\partial \Psi}{\partial D} \tag{3.100}$$

where the Cauchy stress tensor $\underset{\sim}{\sigma}$ is the conjugate force of the viscoelastic strain tensor, R, and Y are the conjugate forces of the isotropic hardening and damage variables, respectively. Substituting the conjugate force of each variable (Eqs. (3.98)-(3.100)) into the Clausius-Duhem inequality (Eq. (3.97)) yields to the following relation, as well called

power of dissipation

$$\mathscr{D}^{\text{mech}} = \underset{\sim}{\boldsymbol{\sigma}} : \dot{\underset{\sim}{\boldsymbol{\varepsilon}}}^{\text{vp}} - R\dot{\kappa} - Y\dot{D} \geqslant 0. \tag{3.101}$$

In order to obtain the evolution of the associated conjugate forces in function of the internal state variables, the power of dissipation $\mathscr{D}^{\text{mech}}$ is decoupled in two parts such as

$$\mathscr{D}^{\text{mech}} = \mathscr{D}^{\text{vp}} + \mathscr{D}^{\text{D}} \tag{3.102}$$

where $\mathscr{D}^{\text{vp}}$ and $\mathscr{D}^{\text{D}}$ are the dissipative power of viscoplasticity and damage, respectively given by

$$\mathscr{D}^{\text{vp}} = \underset{\sim}{\boldsymbol{\sigma}} : \dot{\underset{\sim}{\boldsymbol{\varepsilon}}}^{\text{vp}} - R\dot{\kappa}, \tag{3.103}$$

$$\mathscr{D}^{\text{D}} = -Y\dot{D}. \tag{3.104}$$

The viscoplasticity and damage mechanisms influence each other, and the two dissipated energy are interdependent through the stress and their corresponding conjugate forces. The dissipation potential Θ which depends on the viscoplastic and the damage states variables is postulated as follow

$$\Theta = \Theta\left(\dot{\underset{\sim}{\boldsymbol{\varepsilon}}}^{\text{ve}}, \dot{\kappa}, \dot{D}, \kappa, D\right). \tag{3.105}$$

By using the Legendre transformation, the potential Θ^* dual to Θ which is function of the conjugate forces yields to

$$\Theta^* = \Theta^*\left(\underset{\sim}{\boldsymbol{\sigma}}, R, Y, \kappa, D\right). \tag{3.106}$$

The dual potential Θ^* is used to describe the evolution equations of all the states variables. The potential Θ^* is decoupled into a viscoplastic and a damage potential, such as

$$\Theta^* = f^{\text{vp}}\left(\underset{\sim}{\boldsymbol{\sigma}}, R, D\right) + F^{\text{D}}\left(Y, \kappa, D\right). \tag{3.107}$$

Although, the potential Θ^* is decomposed in both parts, the generalised normality rule involves a single multiplier for the viscoplastic and damage mechanisms such as

$$\dot{\lambda} = \dot{\lambda}\left(\underset{\sim}{\boldsymbol{\sigma}}, R, Y, D\right). \tag{3.108}$$

The approach where the dissipation potential is decomposed in different parts with a unique multiplier was introduced by Lemaitre (1996) where the dissipation potential is divided in a plastic and a damage part with a single multiplier. Using the Lagrangian mul-

tiplier results in the following functional which should be maximised

$$\gamma^* = \mathscr{D}^{\text{mech}} - \dot{\lambda} f^{\text{vp}} - \dot{\lambda} F^{\text{D}}. \tag{3.109}$$

The above functional (Eq. (3.109)) is maximised by applying the following conditions

$$\frac{\partial \gamma^*}{\partial \underset{\sim}{\sigma}} = 0, \tag{3.110}$$

$$\frac{\partial \gamma^*}{\partial R} = 0, \tag{3.111}$$

$$\frac{\partial \gamma^*}{\partial Y} = 0. \tag{3.112}$$

Substituting Eqs. (3.110)-(3.112) into the functional Eq. (3.109) results the following normality rules

$$\dot{\underset{\sim}{\varepsilon}}^{\text{p}} = \dot{\lambda} \frac{\partial f^{\text{vp}}}{\partial \underset{\sim}{\sigma}}, \tag{3.113}$$

$$\dot{\kappa} = -\dot{\lambda} \frac{\partial f^{\text{vp}}}{\partial R}, \tag{3.114}$$

$$\dot{D} = -\dot{\lambda} \frac{\partial F^{\text{D}}}{\partial Y}. \tag{3.115}$$

However, several experimental works on polymeric materials show that viscoplastic deformation of this material is not an isochoric phenomenon (i.e. the trace of the viscoplastic strain tensor is not null during the viscoplastic deformation process). The normality rules of the generalised standard materials cannot be applied for the material being studied. This kind of (visco)plasticty is called non-associated (visco)plasticity. In order to describe the non-associated viscoplastic deformation, a new viscoplastic dissipation potential F^{vp} which differs to the yield surface f^{vp} needs to be introduced. Eqs. (3.113) and (3.114) are modified following non-associated normality rules such as

$$\dot{\underset{\sim}{\varepsilon}}^{\text{p}} = \dot{\lambda} \frac{\partial F^{\text{vp}}}{\partial \underset{\sim}{\sigma}}, \tag{3.116}$$

$$\dot{\kappa} = -\dot{\lambda} \frac{\partial F^{\text{vp}}}{\partial R}. \tag{3.117}$$

In the case where the viscoplastic dissipation potential function F^{vp} is similar to the yield surface f^{vp} (i.e. equipotential surface), the associated viscoplasticity is recovered and the material is therefore a "generalised standard material".

3.3.2 Viscoelastic coupled with damage constitutive equations

The linear viscoelastic Wiechert model which is used in the constitutive model is a finite number of Maxwell elements in parallel with a Hooke element to represent the long term effect (Section 3.1). In the constitutive model, the viscoelastic laws are coupled with the damage phenomenon (i.e. loss of stiffness during loading-unloading path.). The viscoelastic component of the Helmholtz free energy postulated in the constitutive model is therefore function of the viscoelastic strain tensor $\underset{\sim}{\boldsymbol{\varepsilon}}^{ve}$ and the damage variable D such as

$$\rho\Psi^{ve}(\underset{\sim}{\boldsymbol{\varepsilon}}^{ve}, D) = \frac{1}{2}(1-D)\int_0^t \int_0^t \underset{\approx}{\mathscr{R}}^{ve}(2t-\zeta-\varsigma)\frac{d\underset{\sim}{\boldsymbol{\varepsilon}}^{ve}(\zeta)}{d\zeta}\frac{d\underset{\sim}{\boldsymbol{\varepsilon}}^{ve}(\varsigma)}{d\varsigma}d\zeta d\varsigma \tag{3.118}$$

where $\underset{\approx}{\mathscr{R}}^{ve}$ is the relaxation modulus defined in Eq. (3.28). Without the damage coupling in the viscoelastic formulation (introduction of D in Ψ^{ve}), the above expression of the Helmholtz free energy was introduced by Staverman and Schwarzl (1925b,a). In their works, they consider that the Helmholtz free energy per unit volume of the material may be expressed as a sum of the energies of all the springs of the Maxwell chain at time t[‡];

$$\rho\Psi^{ve} = \underset{\approx}{\mathscr{L}}^{ve}{}^{-1}_{\infty}\frac{\underset{\sim}{\boldsymbol{\sigma}}^2_{\infty}(t)}{2(1-D)} + \sum_{i=1}^{N}\underset{\approx}{\mathscr{L}}^{ve-1}_{i}\frac{\underset{\sim}{\boldsymbol{\sigma}}^2_{i}(t)}{2(1-D)}. \tag{3.119}$$

Using the definition of the stress given in Eq. (3.27) combined with the definition of the second order relaxation modulus, the time-stress $\underset{\sim}{\boldsymbol{\sigma}}_{\infty}(t)$ may be expressed as

$$\underset{\sim}{\boldsymbol{\sigma}}_{\infty}(t) = (1-D)\int_0^t \underset{\approx}{\mathscr{L}}^{ve}_{\infty}\frac{d\underset{\sim}{\boldsymbol{\varepsilon}}^{ve}(\zeta)}{d\zeta}d\zeta \tag{3.120}$$

and the time stresses of the Maxwell elements $\underset{\sim}{\boldsymbol{\sigma}}_{i}(t)$ are given by

$$\underset{\sim}{\boldsymbol{\sigma}}_{i}(t) = (1-D)\int_0^t \underset{\approx}{\mathscr{L}}^{ve}_{i}\exp\left(\frac{-t-\zeta}{\tau_i}\right)\frac{d\underset{\sim}{\boldsymbol{\varepsilon}}^{ve}(\zeta)}{d\zeta}d\zeta. \tag{3.121}$$

Substituting Eqs. (3.120) and (3.121) into Eq. (3.119) the Helmholtz free energy can be expressed as

[‡]The following proof of the Helmholtz free energy introduced by Staverman and Schwarzl is modified for the constitutive formulation (coupling with the damage).

$$\rho\Psi^{ve} = \frac{1}{2(1-D)\underset{\approx}{\mathscr{L}}^{ve}_{\infty}} \int_0^t (1-D)\underset{\approx}{\mathscr{L}}^{ve}_{\infty} \frac{d\underset{\sim}{\varepsilon}^{ve}(\zeta)}{d\zeta} d\zeta \int_0^t (1-D)\underset{\approx}{\mathscr{L}}^{ve}_{\infty} \frac{d\underset{\sim}{\varepsilon}^{ve}(\varsigma)}{d\varsigma} d\varsigma$$
$$+ \sum_{i=1}^{N} \underset{\approx}{\mathscr{L}}^{ve}_{\infty} \frac{1}{2(1-D)} \int_0^t (1-D)\underset{\approx}{\mathscr{L}}^{ve}_{i} \exp\left(\frac{-t-\zeta}{\tau_i}\right) \frac{d\underset{\sim}{\varepsilon}^{ve}(\zeta)}{d\zeta} d\zeta$$
$$\cdot \int_0^t (1-D)\underset{\approx}{\mathscr{L}}^{ve}_{i} \exp\left(\frac{-t-\varsigma}{\tau_i}\right) \frac{d\underset{\sim}{\varepsilon}^{ve}(\varsigma)}{d\varsigma} d\varsigma \tag{3.122}$$

which leads to the following relation

$$\rho\Psi^{ve} = \frac{1}{2}(1-D) \int_0^t \int_0^t \underset{\approx}{\mathscr{L}}^{ve}_{\infty} + \sum_{i=1}^{N} \underset{\approx}{\mathscr{L}}^{ve}_{i} \exp\left(\frac{-2t-\zeta-\varsigma}{\tau_i}\right) \frac{d\underset{\sim}{\varepsilon}^{ve}(\zeta)}{d\zeta} \frac{d\underset{\sim}{\varepsilon}^{ve}(\varsigma)}{d\varsigma} d\zeta d\varsigma. \tag{3.123}$$

Considering the expression of the relaxation modulus of the constitutive model (Eq. (3.28)), the above relation is similar to Eq. (3.118). Following the viscoelastic state law (Eq. (3.98)), the corresponding time-dependent stress used in the constitutive model is given by

$$\underset{\sim}{\sigma}(t) = \rho \frac{\partial \Psi^{ve}}{\partial \underset{\sim}{\varepsilon}^{ve}} = (1-D) \int_0^t \underset{\approx}{\mathscr{R}}^{ve}(t-\zeta) \frac{d\underset{\sim}{\varepsilon}^{ve}(\zeta)}{d\zeta} d\zeta. \tag{3.124}$$

3.3.3 Viscoplastic flow rule

In the proposed model, a non-symmetric yield surface is used to capture the different behaviours of the material under different loadings (e.g. tension, compression ...). The yield surface introduced by Raghava *et al.* (1973) is used to model this non-symmetry. This yield surface is described by hydrostatic pressure dependency. This model assumes that the plasticity occurs when the first invariant of the stress tensor (I_1) and the second invariant of the deviatoric stress tensor (J_2) reach a critical combination. Furthermore, in Continuum Damage Mechanics where an isotropic damage process is considered, a scalar variable D (Kachanov, 1958), called isotropic damage variable, is introduced in the yield surface. In order to introduce the concept of the effective stress widely used in CDM (Lemaitre, 1985a,b), the total cross sectional area of a media in this current configuration (i.e. damaged) noted S and the total surface of cracks and voids noted S^D are defined. The fictitious undamaged (i.e. effective) surface of the media, noted $\tilde{S}$, is obtained by removing all the cracks and voids which characterise the damage (Fig. 3.6). For an isotropic damage process, the effective surface is therefore given by

$$\tilde{S} = S - S^D = S(1-D). \tag{3.125}$$

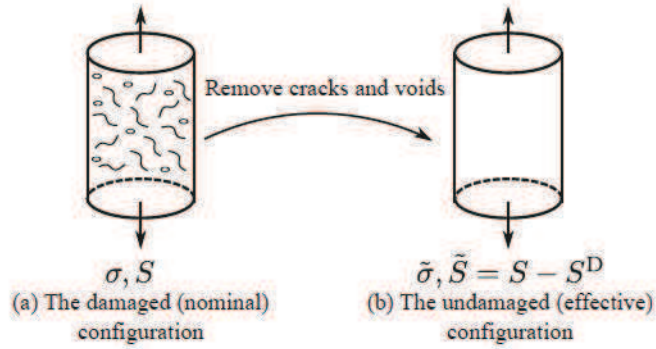

Figure 3.6: *Definition of the effective configuration in Continuum Damage Mechanics.*

The above relation yields to the definition of the effective stress, such as

$$\tilde{\underset{\sim}{\sigma}} = \frac{\underset{\sim}{\sigma}}{1-D}. \tag{3.126}$$

The Raghava yield surface used in the constitutive model which depends on the effective stress is given by

$$f^{vp}\left(\tilde{\underset{\sim}{\sigma}}, R\right) = \frac{(\eta-1)I_1(\tilde{\underset{\sim}{\sigma}}) + \sqrt{(\eta-1)^2 I_1^2(\tilde{\underset{\sim}{\sigma}}) + 12\eta J_2(\tilde{\underset{\sim}{S}})}}{2\eta} - \sigma_t - R(\kappa) \tag{3.127}$$

where $J_2\left(\tilde{\underset{\sim}{S}}\right)$ is the second invariant of the effective deviatoric stress tensor defined as follow

$$J_2\left(\tilde{\underset{\sim}{S}}\right) = \frac{1}{2}\tilde{\underset{\sim}{S}} : \tilde{\underset{\sim}{S}}. \tag{3.128}$$

$I_1(\tilde{\underset{\sim}{\sigma}})$ is the first invariant of the effective stress tensor given by

$$I_1 = \mathrm{tr}\left(\tilde{\underset{\sim}{\sigma}}\right). \tag{3.129}$$

The symbol $\mathrm{tr}(\cdot)$ represents the trace of a tensor. In the yield surface, the material parameter η, which characterises the hydrostatic pressure dependency, is defined by using the ratio between the quasi-static yield stresses in compression and tension, respectively σ_c and σ_t, such as

$$\eta = \frac{\sigma_c}{\sigma_t}. \tag{3.130}$$

The Raghava yield surface represented in the $\sqrt{3J_2} - p$[§] plane normalised by the yield stress σ_t is shown in Fig. 3.7. For an hydrostatic pressure parameter η set to 1, the Raghava yield surface becomes the von Mises yield surface (Eq. (3.81)). The yield surface of the constitu-

[§] p is the hydrostatic pressure, i.e. $p = \frac{1}{3}\mathrm{tr}(\tilde{\underset{\sim}{\sigma}})$.

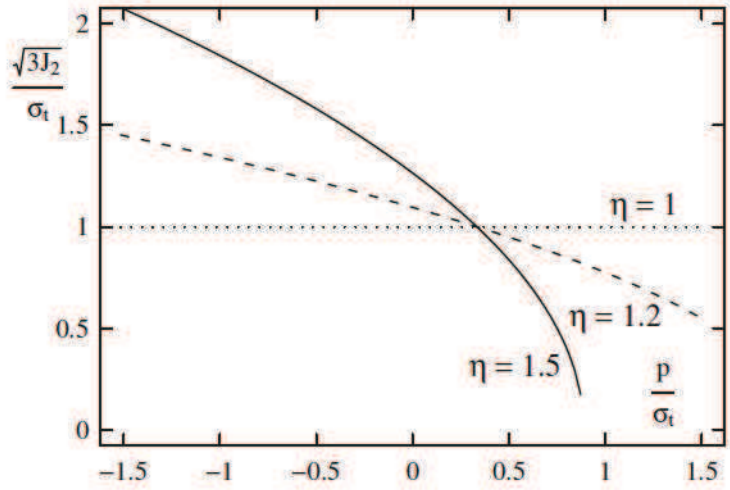

Figure 3.7: *Raghava yield surface for different value of* η.

tive model expressed in term of the nominal stress $\underset{\sim}{\sigma}$ is therefore obtained by substituting Eq. (3.126) into Eq. (3.127), i.e

$$f^{vp}\left(\underset{\sim}{\sigma}, R, D\right) = \frac{(\eta-1)I_1(\underset{\sim}{\sigma}) + \sqrt{(\eta-1)^2 I_1^2(\underset{\sim}{\sigma}) + 12\eta J_2(\underset{\sim}{S})}}{2\eta(1-D)} - \sigma_t - R(\kappa) \tag{3.131}$$

where $I_1(\underset{\sim}{\sigma})$ and $J_2\left(\underset{\sim}{S}\right)$ are the first invariant of the nominal stress tensor and the second invariant of the nominal deviatoric stress tensor, respectively.
The viscoplastic part of the Helmholtz free energy Ψ_{vp} which is a positive definite function of the hardening variable κ is defined as

$$\rho\Psi_{vp} = -\frac{Q_1}{b_1}\left(1+\frac{1}{b_1}\right)\exp(-b_1\kappa) + Q_2\left(\kappa + \frac{\exp(-b_2\kappa)}{b_2}\right) + \frac{b_3}{4}\kappa^4 + \frac{b_4}{3}\kappa^3 + \frac{b_5}{2}\kappa^2. \tag{3.132}$$

Substituting Eq. (3.132) into the viscoplastic state law Eq. (3.99), the thermodynamic conjugate force of the hardening variable R yields to

$$R = \rho\frac{\partial\Psi}{\partial\kappa} = Q_1\kappa\exp(-b_1\kappa) + Q_2(1-\exp(-b_2\kappa)) + b_3\kappa^3 + b_4\kappa^2 + b_5\kappa. \tag{3.133}$$

The hardening parameters Q_1, Q_2, b_1, b_2, b_3, b_4 and b_5 will be defined in the section relating to the parameter identification (Section 4.4.2). As mentioned previously, the plastic deformation of polymer material is not an isochoric phenomenon. The non-associated viscoplasticity is therefore used to represent this volume variation during the viscoplastic deformation process. In the constitutive model, the viscoplastic dissipation potential

function F^{vp} (which is different to the yield surface f^{vp}) is postulated as follows

$$F^{vp}\left(\underset{\sim}{\sigma}\right) = \frac{\sqrt{3J_2\left(\underset{\sim}{S}\right) + \alpha^+ < p >^2 + \alpha^- < -p >^2}}{1 - D} \tag{3.134}$$

where α^+ and α^- are parameters which define the volume variation for positive and negative hydrostatic pressures, respectively. The symbol $< . >$ is the Macauley bracket, that is, for any scalar x, given by $\frac{(x+|x|)}{2}$. This proposed viscoplastic potential is represented in Fig. 3.8 for different values of α^+ and α^-. With this formulation, the flow direction of the rate of the viscoplastic strain tensor for positive and negative pressures can evolve independently.

Polymeric materials are highly strain-rate dependent. A viscoplastic formulation is therefore used to take the strain rate effect on the yield surface into account. The viscous yield surface $\mathscr{F}^{vp}$ which takes the equivalent viscoplastic strain rate $\dot{\kappa}$ into account is defined by

$$\mathscr{F}^{vp}\left(\tilde{\underset{\sim}{\sigma}}, R, \dot{\kappa}, D\right) = \frac{(\eta - 1)I_1(\underset{\sim}{\sigma}) + \sqrt{(\eta - 1)^2 I_1^2(\underset{\sim}{\sigma}) + 12\eta J_2(\underset{\sim}{S}))}}{2\eta(1 - D)} - (\sigma_t + R(\kappa))\left(\frac{\dot{\kappa}}{\dot{\kappa}_0}\right)^n \tag{3.135}$$

where $\dot{\kappa}_0$ and n are material parameters. Following the classic viscoplasticity theory, the equivalent viscoplastic strain rate $\dot{\kappa}$ is defined by

$$\dot{\kappa} = \sqrt{\tfrac{2}{3}\dot{\underset{\sim}{\varepsilon}}^{vp} : \dot{\underset{\sim}{\varepsilon}}^{vp}}. \tag{3.136}$$

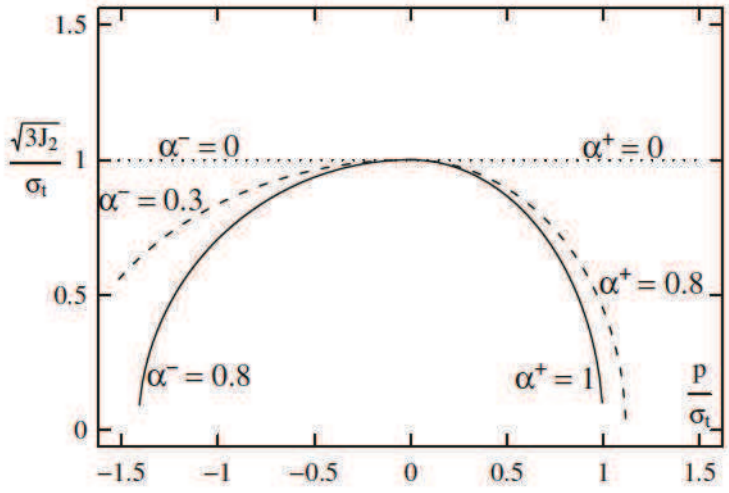

Figure 3.8: *Influence of* α^+ *and* α^- *on the proposed plastic potential.*

Using the normality rule given in Eq. (3.116), the viscoplastic strain rate tensor is defined as follows

$$\dot{\underset{\sim}{\boldsymbol{\varepsilon}}}^{\mathrm{vp}} = \dot{\lambda}\frac{\partial F^{\mathrm{vp}}}{\partial \underset{\sim}{\boldsymbol{\sigma}}} = \dot{\lambda}\,\underset{\sim}{\mathbf{n}} \tag{3.137}$$

where $\underset{\sim}{\mathbf{n}}$ is the direction of the viscoplastic flow expressed as

$$\underset{\sim}{\mathbf{n}} = \frac{1}{g(1-D)}\left(\frac{3}{2}\underset{\sim}{\mathbf{S}} + \frac{1}{3}\left(\alpha^{+} < p > -\alpha^{-} < -p >\right)\underset{\sim}{\mathbf{I}}\right) \tag{3.138}$$

and the scalar g is given by

$$g = \sqrt{3J_2\left(\underset{\sim}{\mathbf{S}}\right) + \alpha^{+} < p >^2 + \alpha^{-} < -p >^2}. \tag{3.139}$$

According to the viscoplastic dissipation potential F^{vp} given in Eq. (3.134), the viscoplastic strain rate tensor becomes

$$\dot{\underset{\sim}{\boldsymbol{\varepsilon}}}^{\mathrm{vp}} = \dot{\lambda}\frac{\partial F^{\mathrm{vp}}}{\partial \underset{\sim}{\boldsymbol{\sigma}}} = \frac{\dot{\lambda}}{g(1-D)}\left(\frac{3}{2}\underset{\sim}{\mathbf{S}} + \frac{1}{3}\left(\alpha^{+} < p > -\alpha^{-} < -p >\right)\underset{\sim}{\mathbf{I}}\right). \tag{3.140}$$

Substituting Eq. (3.136) into the previous definition of the strain rate tensor (Eq. (3.140)), the equivalent viscoplastic strain rate becomes

$$\dot{\kappa} = \dot{\lambda}\sqrt{\tfrac{2}{3}\underset{\sim}{\mathbf{n}} : \underset{\sim}{\mathbf{n}}} = \frac{\dot{\lambda}}{g(1-D)}\sqrt{3J_2(\underset{\sim}{\mathbf{S}}) + \frac{2}{9}(\alpha^{+} < p > -\alpha^{-} < -p >)^2}. \tag{3.141}$$

The rate form of the viscoplastic multiplier $\dot{\lambda}$ is obtained by substituting (Eq. (3.135)) into the viscous yield surface $\mathscr{F}^{\mathrm{vp}}$ (Eq. (3.135)), such as

$$\dot{\lambda} = \begin{cases} 0 & \text{if} \quad f^{\mathrm{vp}} < 0, \\ \dfrac{\dot{\kappa}_0}{\sqrt{\frac{2}{3}\underset{\sim}{\mathbf{n}} : \underset{\sim}{\mathbf{n}}}}\left(\dfrac{(\eta-1)I_1(\underset{\sim}{\boldsymbol{\sigma}}) + \sqrt{(\eta-1)^2 I_1^2(\underset{\sim}{\boldsymbol{\sigma}}) + 12\eta J_2(\underset{\sim}{\mathbf{S}})}}{2\eta(1-D)(\sigma_t + R(\kappa))}\right)^{1/n} & \text{if} \quad f^{\mathrm{vp}} \geqslant 0. \end{cases} \tag{3.142}$$

Finally, The viscoplastic strain rate tensor of the constitutive model is therefore given by

$$\dot{\underset{\sim}{\boldsymbol{\varepsilon}}}^{\mathrm{vp}} = \begin{cases} 0 & \text{if} \quad f^{\mathrm{vp}} < 0, \\ \dfrac{\dot{\kappa}_0}{\sqrt{\frac{2}{3}\underset{\sim}{\mathbf{n}} : \underset{\sim}{\mathbf{n}}}}\left(\dfrac{(\eta-1)I_1(\underset{\sim}{\boldsymbol{\sigma}}) + \sqrt{(\eta-1)^2 I_1^2(\underset{\sim}{\boldsymbol{\sigma}}) + 12\eta J_2(\underset{\sim}{\mathbf{S}})}}{2\eta(1-D)(\sigma_t + R(\kappa))}\right)^{1/n} \underset{\sim}{\mathbf{n}} & \text{if} \quad f^{\mathrm{vp}} \geqslant 0. \end{cases} \tag{3.143}$$

In the constitutive model, the dynamic yield surface (Eq. (3.135)) takes place only if the static yield function Eq. (3.131) is positive or null ($f^{\mathrm{vp}} \geqslant 0$). When the current stress lies in the viscoelastic domain ($f^{\mathrm{vp}} < 0$), the viscoelastic strain rate tensor $\dot{\underset{\sim}{\boldsymbol{\varepsilon}}}^{\mathrm{vp}}$ vanish. The

viscoplastic deformation takes place only when the condition $f^{vp} \geqslant 0$ is satisfied.

3.3.4 Isotropic damage constitutive model

The damage model used in the proposed model is purely phenomenological. This model is based on stress differences between the isochoric and non-isochoric deformation process. For the isochoric plastic deformation, as with some metallic materials, the trace of the (visco)plastic strain tensor is null. On the other hand, the non-isochoric (visco)plastic deformation and the isotropy transverse behaviour characterised in the semi-crystalline polymer studied[¶] lead to some necessary hypotheses to calculate the true stresses. The evolution of the damage variable is postulated as the ratio between the true stresses calculated with the incompressibilty and compressibility assumptions[‖]. As already mentioned, an isotropic damage process represented by a scalar variable D is considered. The damage dissipation potential used in the constitutive model is given by the following relation

$$F^{D}(Y,\kappa,D) = -\frac{Y}{g(1-D)k_c}\sqrt{3J_2(\underset{\sim}{\mathbf{S}}) + \frac{2}{9}(\alpha^{+} < p > -\alpha^{-} < -p >)^2}\exp\left(-\frac{\kappa}{k_c}\right) \tag{3.144}$$

where k_c is a material parameter. Using the normality rule given in Eq. (3.115) with the previous damage dissipation potential F^{D} (Eq. (3.144)), the evolution of the damage internal variable D is expressed as

$$\dot{D} = -\dot{\lambda}\frac{\partial F^{D}}{\partial Y} = \frac{\dot{\lambda}}{g(1-D)k_c}\sqrt{3J_2(\underset{\sim}{\mathbf{S}}) + \frac{2}{9}(\alpha^{+} < p > -\alpha^{-} < -p >)^2}\exp\left(-\frac{\kappa}{k_c}\right). \tag{3.145}$$

Combining with the non-associated evolution of the equivalent viscoplastic strain rate, the damage evolution yields

$$\dot{D} = \frac{\dot{\kappa}}{k_c}\exp\left(-\frac{\kappa}{k_c}\right). \tag{3.146}$$

By obvious integration of Eq. (3.146) and assuming the initial condition $D(\kappa = 0) = 0$, the damage model used in the constitutive model takes the following form

$$D = 1 - \exp\left(-\frac{\kappa}{k_c}\right). \tag{3.147}$$

[¶]The non-isochoric (visco)plastic deformation and the isotropy transverse behaviour of the material studied is presented in the chapter concerning to the experiments (Section 4.2.2).

[‖]The identification of the damage model parameter is developed in Section 4.5.4.

The damage model is therefore only function of the equivalent strain rate. This form of damage is used in the constitutive model to reproduce the experimental measurements**.

3.4 Summary of the constitutive model

The state laws of the viscoelastic-viscoplastic constitutive model are derived from the Helmholtz free energy $\rho\Psi = \rho\Psi_{ve} + \rho\Psi_{vp}$ expressed as

$$\begin{aligned}\rho\Psi &= \frac{1}{2}(1-D)\int_0^t\int_0^t \underset{\approx}{\mathscr{R}}^{ve}(2t-\zeta-\varsigma)\frac{d\underset{\sim}{\varepsilon}^{ve}(\zeta)}{d\zeta}\frac{d\underset{\sim}{\varepsilon}^{ve}(\varsigma)}{d\varsigma}d\zeta d\varsigma \\ &- \frac{Q_1}{b_1}\left(1+\frac{1}{b_1}\right)\exp(-b_1\kappa)+Q_2\left(\kappa+\frac{\exp(-b_2\kappa)}{b_2}\right) \\ &+ s\frac{b_3}{4}\kappa^4+\frac{b_4}{3}\kappa^3+\frac{b_5}{2}\kappa^2.\end{aligned} \tag{3.148}$$

The nominal stress tensor corresponding to the viscoleastic model is therefore given by

$$\underset{\sim}{\sigma}(t) = \rho\frac{\partial\Psi_{ve}}{\partial\underset{\sim}{\varepsilon}^{ve}} = (1-D)\int_0^t \underset{\approx}{\mathscr{R}}^{ve}(t-\zeta)\frac{d\underset{\sim}{\varepsilon}^{ve}(\zeta)}{d\zeta}d\zeta. \tag{3.149}$$

The conjugate force of the hardening variable κ is defined by

$$R = \rho\frac{\partial\Psi_{vp}}{\partial\kappa} = Q_1\kappa\exp(-b_1\kappa)+Q_2(1-\exp(-b_2\kappa))+b_3\kappa^3+b_4\kappa^2+b_5\kappa. \tag{3.150}$$

The evolution laws for the internal variables are derived from the normality rule applied to the dissipation potential $\Theta^* = f^{vp}\left(\underset{\sim}{\sigma},\kappa,D\right)+F^D\left(Y,\kappa,D\right)$ where

$$f^{vp}\left(\underset{\sim}{\sigma},R,D\right) = \frac{(\eta-1)I_1(\underset{\sim}{\sigma})+\sqrt{(\eta-1)^2I_1^2(\underset{\sim}{\sigma})+12\eta J_2(\underset{\sim}{S})}}{2\eta(1-D)}-\sigma_t-R(\kappa), \tag{3.151}$$

$$F^D\left(Y,\kappa,D\right) = -\frac{Y}{g(1-D)k_c}\sqrt{3J_2(\underset{\sim}{S})+\frac{2}{9}(\alpha^+<p>-\alpha^-<-p>)^2}\exp\left(-\frac{\kappa}{k_c}\right). \tag{3.152}$$

Furthermore, the non-associated viscoplasticity used in the constitutive model needs to define another viscoplastic dissipation potential F^{vp} which is different to the yield surface f^{vp} such as

$$F^{vp}\left(\underset{\sim}{\sigma}\right) = \frac{\sqrt{3J_2\left(\underset{\sim}{S}\right)+\alpha^+<p>^2+\alpha^-<-p>^2}}{1-D}. \tag{3.153}$$

**The experimental procedure to measure the damage evolution is detailed in Section 4.5.4

The evolution laws for the viscoplastic strain tensor and damage variable become

$$\dot{\underset{\sim}{\varepsilon}}^{\mathrm{vp}} = \dot{\lambda}\frac{\partial F^{\mathrm{vp}}}{\partial \underset{\sim}{\sigma}} = \dot{\lambda}\underset{\sim}{\mathbf{n}}, \tag{3.154}$$

$$\dot{D} = -\dot{\lambda}\frac{\partial F^{\mathrm{D}}}{\partial Y} = \frac{\dot{\kappa}}{k_c}\exp\left(-\frac{\kappa}{k_c}\right) \tag{3.155}$$

where $\underset{\sim}{\mathbf{n}}$ and $\dot{\kappa}$ are given by

$$\underset{\sim}{\mathbf{n}} = \frac{1}{g(1-D)}\left(\frac{3}{2}\underset{\sim}{\mathbf{S}} + \frac{1}{3}\left(\alpha^{+} < p > -\alpha^{-} < -p >\right)\underset{\sim}{\mathbf{I}}\right), \tag{3.156}$$

$$\dot{\kappa} = \sqrt{\tfrac{2}{3}\dot{\underset{\sim}{\varepsilon}}^{\mathrm{vp}} : \dot{\underset{\sim}{\varepsilon}}^{\mathrm{vp}}} = \frac{\dot{\lambda}}{g(1-D)}\sqrt{3J_2(\underset{\sim}{\mathbf{S}}) + \frac{2}{9}(\alpha^{+} < p > -\alpha^{-} < -p >)^2}. \tag{3.157}$$

The viscoplastic strain rate tensor given by the viscoplastic formulation is defined by

$$\dot{\underset{\sim}{\varepsilon}}^{\mathrm{vp}} = \begin{cases} 0 & \text{if} \quad f^{\mathrm{vp}} < 0, \\ \dfrac{\dot{\kappa}_0}{\sqrt{\frac{2}{3}\underset{\sim}{\mathbf{n}}:\underset{\sim}{\mathbf{n}}}}\left(\dfrac{(\eta-1)I_1(\underset{\sim}{\sigma}) + \sqrt{(\eta-1)^2 I_1^2(\underset{\sim}{\sigma}) + 12\eta J_2(\underset{\sim}{\mathbf{S}})}}{2\eta(1-D)(\sigma_t + R(\kappa))}\right)^{1/n}\underset{\sim}{\mathbf{n}} & \text{if} \quad f^{\mathrm{vp}} \geqslant 0. \end{cases} \tag{3.158}$$

When the viscoplastic process takes place (i.e. $f^{\mathrm{vp}} \geqslant 0$), a set of 3 nonlinear equations, of the 3 variables $\mathcal{W} = \left\{\underset{\sim}{\varepsilon}^{\mathrm{ve}}, D, \lambda\right\}$, needs to be solved in a coupled manner as follows

$$\left\{\begin{array}{l} \dot{\underset{\sim}{\varepsilon}}^{\mathrm{ve}} - \dot{\underset{\sim}{\varepsilon}} + \dot{\lambda}\underset{\sim}{\mathbf{n}} \\ \dot{D} - \dfrac{\sqrt{\frac{2}{3}\underset{\sim}{\mathbf{n}}:\underset{\sim}{\mathbf{n}}}}{k_c}\exp\left(-\frac{\kappa}{k_c}\right)\dot{\lambda} \\ \dot{\lambda} - \dfrac{\dot{\kappa}_0}{\sqrt{\frac{2}{3}\underset{\sim}{\mathbf{n}}:\underset{\sim}{\mathbf{n}}}}\left(\dfrac{(\eta-1)I_1(\underset{\sim}{\sigma}) + \sqrt{(\eta-1)^2 I_1^2(\underset{\sim}{\sigma}) + 12\eta J_2(\underset{\sim}{\mathbf{S}})}}{2\eta(1-D)(\sigma_t + R(\kappa))}\right)^{1/n} \end{array}\right\} = \left\{\begin{array}{c} \underset{\sim}{\mathbf{0}} \\ 0 \\ 0 \end{array}\right\}. \tag{3.159}$$

The resolution of this system in a user-material subroutine for an implicit and explicit finite element codes is described in the next section.

3.5 Implementation of the viscoelastic-viscoplastic constitutive model

The viscoelastic-viscoplastic constitutive model is implemented in FORTRAN 77 in a user-material subroutine for the implicit and explicit finite element codes ABAQUS®and LS-DYNA®, respectively. The implementation into the two finite element codes is similar, the

stress update is performed with an implicit backward-euler scheme. The unique difference between the two implementations is the consistent tangent operator which is not evaluated for the explicit finite element code due to the non integration of the equilibrium iterations at the global level. For the equations developed in the following sections, the subscript $_n$ defines the current time step, $(\cdot)^{\text{tr}}$ corresponds to the data calculated during the viscoelastic prediction, $(\cdot)_n$, $(\cdot)_{n+1}$ and $\Delta(\cdot)$, are respectively, the values at the start, the end of the time step and its increment during the time step. At each time step the subroutine access to the previous values of the viscoelastic strain tensor $\underset{\sim}{\boldsymbol{\varepsilon}}^{\text{ve}}_n$, the stress quantities $\underset{\sim}{\mathbf{h}}_n$ (necessary for the viscoelastic formulation), the damage and the equivalent viscoplastic strain values, respectively, D_n and κ_n and the current incremental total strain tensor $\Delta\underset{\sim}{\boldsymbol{\varepsilon}}$ given by the finite element code.

3.5.1 Implicit viscoelastic predictor/viscoplastic corrector scheme

During the viscoelastic prediction step, the incremental strain tensor $\Delta\underset{\sim}{\boldsymbol{\varepsilon}}$ is considered to be purely viscoelastic. the viscoelastic strain tensor calculated during the viscoelastic prediction is therefore given by

$$\underset{\sim}{\boldsymbol{\varepsilon}}^{\text{ve tr}}_{n+1} = \underset{\sim}{\boldsymbol{\varepsilon}}^{\text{ve}}_n + \Delta\underset{\sim}{\boldsymbol{\varepsilon}}. \tag{3.160}$$

As in classic CDM formulation, the effective stress tensor $\tilde{\underset{\sim}{\boldsymbol{\sigma}}}$ is used in the viscoelastic prediction. Combining the definition of the stress given by the Helmholtz free energy (Eq. (3.149)) and Eq. (3.46) given in the section concerning the implementation of the Wierchet viscoelastic model (Section 3.1.3), the corresponding effective stress tensor calculated during the viscoelastic prediction phase is expressed as

$$\tilde{\underset{\sim}{\boldsymbol{\sigma}}}^{\text{tr}}_{n+1} = \underset{\approx}{\mathscr{L}}^{\text{ve}}_{\infty} : \underset{\sim}{\boldsymbol{\varepsilon}}^{\text{ve tr}}_{n+1} + \sum_{i}^{N} \underset{\sim}{\mathbf{h}}^{\text{tr}}_{i\,n+1} \tag{3.161}$$

where $\underset{\sim}{\mathbf{h}}^{\text{tr}}_{i\,n+1}$ is given by the following relation

$$\underset{\sim}{\mathbf{h}}^{\text{tr}}_{i\,n+1} = \exp\left(-\frac{\Delta t}{\tau_i}\right)\underset{\sim}{\mathbf{h}}^{\text{tr}}_{i\,n} + \Xi_i \frac{1-\exp\left(-\frac{\Delta t}{\tau_i}\right)}{\frac{\Delta t}{\tau_i}}\left[\tilde{\underset{\sim}{\boldsymbol{\sigma}}}^{\text{tr}}_{\infty n+1} - \tilde{\underset{\sim}{\boldsymbol{\sigma}}}_{\infty n}\right]. \tag{3.162}$$

The trial long term effective stress tensor $\tilde{\underset{\sim}{\boldsymbol{\sigma}}}^{\text{tr}}_{\infty n+1}$ is calculated as follow

$$\tilde{\underset{\sim}{\boldsymbol{\sigma}}}^{\text{tr}}_{\infty n+1} = \underset{\approx}{\mathscr{L}}^{\text{ve}}_{\infty} : \underset{\sim}{\boldsymbol{\varepsilon}}^{\text{ve tr}}_{n+1}. \tag{3.163}$$

Using Eqs. (3.82) and (3.129), the effective deviatoric and first invariant of the stress tensor become

$$\tilde{\underset{\sim}{\mathbf{S}}}^{\mathrm{tr}}_{n+1} = \underset{\approx}{\mathbf{I}}_{\mathrm{d}} : \tilde{\underset{\sim}{\boldsymbol{\sigma}}}^{\mathrm{tr}}_{n+1}, \tag{3.164}$$

$$I_1(\tilde{\underset{\sim}{\boldsymbol{\sigma}}}^{\mathrm{tr}}_{n+1}) = \mathrm{tr}(\tilde{\underset{\sim}{\boldsymbol{\sigma}}}^{\mathrm{tr}}_{n+1}) \tag{3.165}$$

The corresponding yield surface used during the viscoelastic prediction step is given by

$$f^{\mathrm{vp\ tr}}_{n+1}\left(\tilde{\underset{\sim}{\boldsymbol{\sigma}}}^{\mathrm{tr}}_{n+1}, \kappa_n\right) = \frac{(\eta-1)I_1(\tilde{\underset{\sim}{\boldsymbol{\sigma}}}^{\mathrm{tr}}_{n+1}) + \sqrt{(\eta-1)^2 I_1^2(\tilde{\underset{\sim}{\boldsymbol{\sigma}}}^{\mathrm{tr}}_{n+1}) + 12\eta J_2(\tilde{\underset{\sim}{\mathbf{S}}}^{\mathrm{tr}}_{n+1}))}}{2\eta} - \sigma_t - R(\kappa_n). \tag{3.166}$$

For a purely viscoelastic deformation (i.e. $f^{\mathrm{tr}}_{n+1} < 0$), the previous viscoelastic strain tensor and the equivalent viscoplastic strain used during the elastic prediction step are solutions of the problem. The new stress tensor is therefore updapted such as

$$\underset{\sim}{\boldsymbol{\sigma}}_{n+1} = (1 - D_n)\tilde{\underset{\sim}{\boldsymbol{\sigma}}}^{\mathrm{tr}}_{n+1}. \tag{3.167}$$

The viscoelastic strain tensor $\underset{\sim}{\boldsymbol{\varepsilon}}^{\mathrm{ve}}_{n+1}$, stress quantities $\underset{\sim}{\mathbf{h}}_{n+1}$, damage D_{n+1} and equivalent viscoplastic strain κ_{n+1} are therefore stored for the next time step, as follow

$$\begin{aligned}
\underset{\sim}{\boldsymbol{\varepsilon}}^{\mathrm{ve}}_{n+1} &= \underset{\sim}{\boldsymbol{\varepsilon}}^{\mathrm{ve\ tr}}_{n+1}, \\
\underset{\sim}{\mathbf{h}}_{n+1} &= \underset{\sim}{\mathbf{h}}^{\mathrm{tr}}_{n+1}, \\
D_{n+1} &= D_n, \\
\kappa_{n+1} &= \kappa_n.
\end{aligned} \tag{3.168}$$

Otherwise the deformation is viscoelastic-viscoplastic and a viscoplastic corrector scheme is needed to evaluate the viscoplastic part of the deformation. The new strain tensor is then an additive decomposition into a viscoelastic and a viscoplastic component as below

$$\underset{\sim}{\boldsymbol{\varepsilon}}_{n+1} = \underset{\sim}{\boldsymbol{\varepsilon}}^{\mathrm{ve}}_{n+1} + \underset{\sim}{\boldsymbol{\varepsilon}}^{\mathrm{vp}}_{n+1} \tag{3.169}$$

or expressed in incremental form as follows

$$\Delta\underset{\sim}{\boldsymbol{\varepsilon}} = \Delta\underset{\sim}{\boldsymbol{\varepsilon}}^{\mathrm{ve}} + \Delta\underset{\sim}{\boldsymbol{\varepsilon}}^{\mathrm{vp}}. \tag{3.170}$$

The new nominal effective stress tensor is therefore calculated such as

$$\tilde{\underset{\sim}{\boldsymbol{\sigma}}}_{n+1} = \tilde{\underset{\sim}{\boldsymbol{\sigma}}}^{\mathrm{tr}}_{n+1} - \underset{\approx}{\mathscr{L}}^{\mathrm{ve}} : \Delta\underset{\sim}{\boldsymbol{\varepsilon}}^{\mathrm{vp}}. \tag{3.171}$$

According to the non-associated viscoplastic flow rule (Eq. (3.140)), the incremental viscoplastic strain tensor is defined by

$$\Delta \underset{\sim}{\boldsymbol{\varepsilon}}^{\mathrm{vp}} = \Delta\lambda \underset{\sim}{\mathbf{n}}_{n+1} \tag{3.172}$$

where $\underset{\sim}{\mathbf{n}}$ is the derivative of the viscoplastic dissipation potential F^{vp} with respect to the nominal stress tensor, as follow

$$\underset{\sim}{\mathbf{n}}_{n+1} = \frac{\partial F^{\mathrm{vp}}_{n+1}}{\partial \underset{\sim}{\boldsymbol{\sigma}}_{n+1}} = \frac{1}{g_{n+1}(1-D_{n+1})}\left(\frac{3}{2}\underset{\sim}{\mathbf{S}}_{n+1} + \frac{1}{3}\left(\alpha^{+} < p_{n+1} > -\alpha^{-} < -p_{n+1} >\right)\underset{\sim}{\mathbf{I}}\right) \tag{3.173}$$

where g_{n+1} is defined such as

$$g_{n+1} = \sqrt{3J_2\left(\underset{\sim}{\mathbf{S}}_{n+1}\right) + \alpha^{+} < p_{n+1} >^2 + \alpha^{-} < -p_{n+1} >^2}. \tag{3.174}$$

Following the constitutive viscoplastic model (Eq. (3.142)), the incremental form of the plastic multiplier $\Delta\lambda$ is given by

$$\Delta\lambda = \frac{\Delta t \dot{\kappa}_0}{\sqrt{\frac{2}{3}\underset{\sim}{\mathbf{n}}_{n+1} : \underset{\sim}{\mathbf{n}}_{n+1}}}\left(\frac{(\eta-1)I_1(\tilde{\underset{\sim}{\sigma}}_{n+1}) + \sqrt{(\eta-1)^2 I_1^2(\tilde{\underset{\sim}{\sigma}}_{n+1}) + 12\eta J_2(\tilde{\underset{\sim}{S}}_{n+1})}}{2\eta\left(\sigma_t + R(\kappa)\right)}\right)^{1/n}. \tag{3.175}$$

The damage increment ΔD and the equivalent viscoplastic strain increment $\Delta\kappa$ arising from Eqs. (3.146) and (3.141) evolve following

$$\Delta D = \frac{\sqrt{\frac{2}{3}\underset{\sim}{\mathbf{n}}_{n+1} : \underset{\sim}{\mathbf{n}}_{n+1}}}{k_c}\exp\left(-\frac{\kappa_{n+1}}{k_c}\right)\Delta\lambda, \tag{3.176}$$

$$\Delta\kappa = \sqrt{\frac{2}{3}\underset{\sim}{\mathbf{n}}_{n+1} : \underset{\sim}{\mathbf{n}}_{n+1}}\,\Delta\lambda \tag{3.177}$$

where

$$\sqrt{\frac{2}{3}\underset{\sim}{\mathbf{n}}_{n+1} : \underset{\sim}{\mathbf{n}}_{n+1}} = \frac{1}{g(1-D_{n+1})}\sqrt{3J_2(\underset{\sim}{\mathbf{S}}_{n+1}) + \frac{2}{9}(\alpha^{+} < p_{n+1} > -\alpha^{-} < -p_{n+1} >)^2}. \tag{3.178}$$

In order to solve the system given in Eq. (3.159), the Newton-Raphson iterative method is used to compute the values $\Delta\mathcal{W} = \left\{\Delta\underset{\sim}{\boldsymbol{\varepsilon}}^{\mathrm{ve}}, \Delta D, \Delta\lambda\right\}$. At the $(k+1)$ iteration, each variable of $\Delta\mathcal{W}$ is calculated as follows

$$\{\Delta\mathcal{W}\}^{k+1} = \{\Delta\mathcal{W}\}^{k} - \left[\frac{\partial\mathcal{R}^k}{\partial\Delta\mathcal{W}^k}\right]^{-1}\{\mathcal{R}\}^{k} \tag{3.179}$$

where $\mathcal{R} = \left\{\underset{\sim}{\mathcal{R}}_{\varepsilon^{ve}}, \mathcal{R}_D, \mathcal{R}_\lambda\right\}$ is a set of 3 residuals which, for the viscoelastic-viscoplastic model coupled with damage, are given by

$$\begin{cases} \underset{\sim}{\mathcal{R}}_{\varepsilon^{ve}} = \Delta\underset{\sim}{\boldsymbol{\varepsilon}}^{ve} - \Delta\underset{\sim}{\boldsymbol{\varepsilon}} + \Delta\lambda\, \underset{\sim}{\mathbf{n}}_{n+1}, \\ \mathcal{R}_D = \Delta D - \dfrac{\sqrt{\frac{2}{3}\underset{\sim}{\mathbf{n}}_{n+1} : \underset{\sim}{\mathbf{n}}_{n+1}}}{k_c} \exp\left(-\dfrac{\kappa_{n+1}}{k_c}\right)\Delta\lambda, \\ \mathcal{R}_\lambda = \Delta\lambda - \Delta t \dfrac{\dot{\kappa}_0}{\sqrt{\frac{2}{3}\underset{\sim}{\mathbf{n}}_{n+1} : \underset{\sim}{\mathbf{n}}_{n+1}}} \left(\dfrac{(\eta-1)I_1(\tilde{\underset{\sim}{\boldsymbol{\sigma}}}_{n+1}) + \sqrt{(\eta-1)^2 I_1^2(\tilde{\underset{\sim}{\boldsymbol{\sigma}}}_{n+1}) + 12\eta J_2(\tilde{\underset{\sim}{\mathbf{S}}}_{n+1})}}{2\eta(1-D_{n+1})(\sigma_t + R(\kappa))} \right)^{1/n}. \end{cases} \tag{3.180}$$

The term $\left[\frac{\partial\mathcal{R}}{\partial\Delta\mathcal{W}}\right]$ is the Jacobian matrix $[J]$ which contains the partial derivatives of each residual $\mathcal{R} = \left\{\underset{\sim}{\mathcal{R}}_{\varepsilon^{ve}}, \mathcal{R}_D, \mathcal{R}_\lambda\right\}$ with respect to each variable $\Delta\mathcal{W} = \left\{\Delta\underset{\sim}{\boldsymbol{\varepsilon}}^{e},\ \Delta D,\ \Delta\lambda\right\}$ as follow

$$[J] = \left[\frac{\partial\mathcal{R}}{\partial\Delta\mathcal{W}}\right] = \begin{bmatrix} \underset{\sim}{\mathcal{R}}_{\varepsilon^{ve},\Delta\varepsilon^{ve}} & \underset{\sim}{\mathcal{R}}_{\varepsilon^{ve},\Delta D} & \underset{\sim}{\mathcal{R}}_{\varepsilon^{ve},\Delta\lambda} \\ \underset{\sim}{\mathcal{R}}_{D,\Delta\varepsilon^{ve}} & \mathcal{R}_{D,\Delta D} & \mathcal{R}_{D,\Delta\lambda} \\ \underset{\sim}{\mathcal{R}}_{\lambda,\Delta\varepsilon^{ve}} & \mathcal{R}_{\lambda,\Delta D} & \mathcal{R}_{\lambda,\Delta\lambda} \end{bmatrix}. \tag{3.181}$$

The Newton-Raphson iterative scheme is performed until the residuals $\mathcal{R}$ reach the tolerance values $\mathcal{T} = \{\mathcal{T}_\varepsilon, \mathcal{T}_D, \mathcal{T}_{\Delta\lambda}\}$ such as

$$\begin{Bmatrix} \mathcal{T}_\varepsilon \\ \mathcal{T}_D \\ \mathcal{T}_{\Delta\lambda} \end{Bmatrix} = \begin{Bmatrix} \varkappa_\varepsilon \left\|\underset{\sim}{\boldsymbol{\varepsilon}}^{ve\,tr}_{n+1}\right\| \\ \varkappa_D \\ \varkappa_\lambda \end{Bmatrix}. \tag{3.182}$$

$\varkappa_\varepsilon$, $\varkappa_D$ and $\varkappa_\lambda$ are tolerances chosen according to the quantities of the concerned values. When the set of nonlinear equations (Eq. (3.159)) is solved, the state variables D_{n+1}, κ_{n+1} and the converged viscoelastic strain tensor $\underset{\sim}{\boldsymbol{\varepsilon}}^{ve}_{n+1}$ are stored for the next time step. The stress quantities $\underset{\sim}{\mathbf{h}}_{i\ n+1}$ need to be updated in order to be stored for the next time step as well. $\underset{\sim}{\mathbf{h}}_{i\ n+1}$ becomes

$$\underset{\sim}{\mathbf{h}}_{in+1} = \exp\left(-\frac{\Delta t}{\tau_i}\right)\underset{\sim}{\mathbf{h}}_{in} + \Xi_i \frac{1-\exp\left(-\frac{\Delta t}{\tau_i}\right)}{\frac{\Delta t}{\tau_i}}\left[\tilde{\underset{\sim}{\boldsymbol{\sigma}}}_{\infty n+1} - \tilde{\underset{\sim}{\boldsymbol{\sigma}}}_{\infty n}\right], \tag{3.183}$$

where

$$\tilde{\underset{\sim}{\boldsymbol{\sigma}}}_{\infty n+1} = \underset{\approx}{\mathscr{L}}^{ve}_{\infty} : \underset{\sim}{\boldsymbol{\varepsilon}}^{ve}_{n+1}. \tag{3.184}$$

Finally, the new nominal stress tensor is then updated

$$\underset{\sim}{\boldsymbol{\sigma}}_{n+1} = (1 - D_{n+1})\tilde{\underset{\sim}{\boldsymbol{\sigma}}}_{n+1} \tag{3.185}$$

Table 3.1: *Stress return algorithm of the viscoelastic-viscoplastic constitutive model.*

(i) Compute the effective viscoelastic trial stress

$$\tilde{\boldsymbol{\sigma}}^{\mathrm{tr}}_{n+1} = \underset{\approx}{\mathscr{L}}^{\mathrm{ve}}_{\infty} : \boldsymbol{\varepsilon}^{\mathrm{tr}\ 1} + \sum_i^N \mathbf{h}^{\mathrm{tr}}_{i\ n+1}$$

(ii) Check viscoplastic admissibility

$$\text{IF } f^{\mathrm{vp\ tr}}_{n+1}\left(\tilde{\boldsymbol{\sigma}}^{\mathrm{tr}}_{n+1}, \kappa_n\right) < 0$$

$$\text{THEN } (.)_{n+1} = (.)^{\mathrm{tr}}_{n+1} \text{ and GOTO (vi)}$$

(iii) Viscoplastic stress return

$$\{\mathcal{W}\}^{k+1} = \{\mathcal{W}\}^{k} - \left[\frac{\partial \mathcal{R}^k}{\partial \Delta \mathcal{W}^k}\right]^{-1} \{\mathcal{R}\}^{k}$$

(iv) Check convergence

$$\text{IF } \{\mathcal{R}\}^{k} \leq \{\mathcal{T}\} \text{ THEN GOTO (v)}$$

$$\text{GOTO (iii)}$$

(v) Update stresses

$$\boldsymbol{\sigma}_{n+1} = (1 - D_{n+1})\tilde{\boldsymbol{\sigma}}_{n+1}$$

$$\mathbf{h}_{in+1} = \exp\left(-\frac{\Delta t}{\tau_i}\right)\mathbf{h}_{in} + \Xi_i \frac{1-\exp\left(-\frac{\Delta t}{\tau_i}\right)}{\frac{\Delta t}{\tau_i}}\left[\tilde{\boldsymbol{\sigma}}_{\infty n+1} - \tilde{\boldsymbol{\sigma}}_{\infty n}\right]$$

(vi) Store $\boldsymbol{\varepsilon}^{\mathrm{ve}}_{n+1}$, κ_{n+1}, D_{n+1} , $\boldsymbol{\sigma}_{n+1}$, $\mathbf{h}_{in+1}$

The complete algorithm for the viscoelastic-viscoplastic stress return is presented in Table 3.1.

3.5.2 Consistent tangent operator

For the implementation into the implicit finite element code ABAQUS/Standard®, the fourth order consistent tangent tensor of the constitutive model needs to be calculated to evaluate the equilibrium at the global level. The consistent tangent operator $\underset{\approx}{\mathscr{L}}$ is given by the well known relation (Simo and Taylor, 1985)

$$\underset{\approx}{\mathscr{L}} = \frac{\partial \boldsymbol{\sigma}}{\partial \boldsymbol{\varepsilon}}. \tag{3.186}$$

If the yield surface corresponding to the viscoelastic trial prediction lies inside the viscoelastic domain (i.e. $f^{\mathrm{vp\ tr}}_{n+1} < 0$), the closed form of the consistent tangent operator is given

by the damaged viscoelatic combined with Eq. (3.48), such as

$$\underset{\approx}{\mathscr{L}} = (1 - D_{n+1})\underset{\approx}{\mathscr{L}}^{\text{ve}} = (1 - D_{n+1}) \left\{ 1 + \sum_{j=1}^{N} \frac{1 - \exp\left(\frac{\Delta t}{\tau_j}\right)}{\frac{\Delta t}{\tau_j}} \right\} \underset{\approx}{\mathscr{L}}^{\text{ve}}_{\infty}. \tag{3.187}$$

Under viscoplastic loading, the consistent tangent operator is extracted directly from the jacobian matrix $[J]$ (Eq. (3.181)) calculated during the viscoplastic corrector scheme. When the system given by Eq. (3.159) is solved, the resolution of the constitutive equations by Newton-Raphson iterations leads to

$$\left[\begin{array}{c} \Delta \underset{\sim}{\boldsymbol{\varepsilon}}^{\text{ve}} \\ \hline - \end{array} \right] = \left[\begin{array}{c|c} \underset{\approx 11}{\mathbf{J}^{\star}} & - \\ \hline - & - \end{array} \right] \cdot \left[\begin{array}{c} \Delta \underset{\sim}{\boldsymbol{\varepsilon}} \\ \hline 0 \end{array} \right], \tag{3.188}$$

where $\underset{\approx 11}{\mathbf{J}^{\star}}$ is the upper left part of the inverse of the jacobian matrix $[J]^{-1}$. The incremental viscoelastic strain tensor extracted from Eq. (3.188) reads

$$\Delta \underset{\sim}{\boldsymbol{\varepsilon}}^{\text{ve}} = \underset{\approx 11}{\mathbf{J}^{\star}} : \Delta \underset{\sim}{\boldsymbol{\varepsilon}}. \tag{3.189}$$

By combining Eq. (3.189) with the definition of the tangent operator (Eq. (3.186)), the consistent tangent operator of the constitutive model is defined by

$$\underset{\approx}{\mathscr{L}} = (1 - D_{n+1})\underset{\approx}{\mathscr{L}}^{\text{ve}} : \underset{\approx 11}{\mathbf{J}^{\star}}. \tag{3.190}$$

Due to the coupling of damage and non-associated viscoplasticity, the consistent tangent operator of the constitutive model is not symmetric.

3.6 Implementation of the constitutive model with shell elements

To implement this viscoelastic-viscoplastic model with shell elements, the thickness stress must vanish. In shell element, the stress tensor possesses 5 components and the strain tensor is the same as the three-dimensional case. Furthermore, the transverse shear stress components, σ_{xz} and σ_{yz}, are computed outside of the viscoelastic-viscoplastic stress return, by using the shear factor parameter χ such as

$$\begin{aligned} \sigma_{xz} &= \chi \varepsilon_{xz}, \\ \sigma_{yz} &= \chi \varepsilon_{yz}. \end{aligned} \tag{3.191}$$

During the viscoelastic predictor/viscoplastic return mapping scheme, the stress and strain tensors for shell elements are composed of 3 and 4 components, respectively and a plane stress viscoelastic-viscoplastic problem is assumed. In plane stress viscoplasticity, the implicit backward-euler scheme needs to take the zero-normal-stress condition into account, and a number of techniques have been proposed to achieve this objective.
The solution of the constitutive plane stress problem was proposed by Schreyer *et al.* (1979), Jetteur (1986) and Simo and Taylor (1986), where the return mapping is projected in the plane stress space. However plane stress projected equations can only really be used for relatively simple models. For more complex models, other solution methods have therefore been developed. Borst (1991) proposed a procedure without any change to the classic three-dimensional return mapping by introducing the plane stress constraint in the global finite element equations. The enforcement of the plane stress constraint at the structural level is only compatible with implicit finite element codes. This procedure cannot be used with explicit finite element codes due to the non-integration of the equilibrium iterations. In this paper a double iteration scheme at the local level is considered. In this method, introduced by Dodds (1987), the zero-normal-stress constraint is enforced iteratively by computing the out of plane strain component at the end of the viscoplastic stress return. Like the previous procedure, the classic viscoelastic predictor/viscoplastic return mapping scheme is not modified and can also be used for a wide range of constitutive models.
In the developed model, the axisymmetric viscoelastic predictor/viscoplastic return mapping scheme is used to solve the viscoelastic-viscoplastic problem (Section 3.5). The unknown out of plane strain, ε_{zz}, is computed iteratively until the respect of the zero-normal-stress condition. The axisymmetric stress and strain tensors are defined respectively by

$$\underset{\sim}{\sigma} = \begin{Bmatrix} \sigma_{xx} & \sigma_{xy} & 0 \\ \sigma_{xy} & \sigma_{yy} & 0 \\ 0 & 0 & \sigma_{zz} \end{Bmatrix} \text{ and } \underset{\sim}{\varepsilon} = \begin{Bmatrix} \varepsilon_{xx} & \varepsilon_{xy} & 0 \\ \varepsilon_{xy} & \varepsilon_{yy} & 0 \\ 0 & 0 & \varepsilon_{zz} \end{Bmatrix}. \tag{3.192}$$

First of all, an initial value of the out of plane strain is used, this value can be the out of plane strain component calculated at the previous time step. In the constitutive model the Hooke law is used for the initial value of ε_{zz}^{tr} such as

$$\varepsilon_{zz}^{tr\,1} = -\left(\frac{\nu}{1-\nu}\right)\left(\varepsilon_{xx}^{tr} + \varepsilon_{yy}^{tr}\right) \tag{3.193}$$

where ν is the Poisson ratio. At the end of the axisymmetric predictor/return mapping scheme, the out of plane stress component σ_{zz} is checked and if the plane stress condition is not respected (i.e. $\sigma_{zz} \neq 0$), the value of the component ε_{zz}^{tr} is updated by using the

following relation

$$\varepsilon_{zz}^{\text{tr } i+1} = \varepsilon_{zz}^{\text{tr } i} - \frac{\sigma_{zz}^{i}}{\mathscr{L}_{22}^{i}}. \tag{3.194}$$

Another axisymmetric predictor/return mapping scheme starts and the procedure is repeated until the plane stress condition is reached. The term $\mathscr{L}_{22}$ used in Eq. (3.194) is the lower right component of the axisymmetric consistent tangent operator[††] $\underset{\sim}{\mathscr{L}}$ such as

$$\left[\begin{array}{c} \Delta\sigma_{xx} \\ \Delta\sigma_{yy} \\ \Delta\sigma_{xy} \\ \hline \Delta\sigma_{zz} \end{array}\right] = \left[\begin{array}{c|c} \underset{\sim}{\mathscr{L}}_{11} & \mathscr{L}_{12} \\ \hline \mathscr{L}_{21} & \mathscr{L}_{22} \end{array}\right] \left[\begin{array}{c} \Delta\varepsilon_{xx} \\ \Delta\varepsilon_{yy} \\ 2\Delta\varepsilon_{xy} \\ \hline \Delta\varepsilon_{zz} \end{array}\right]. \tag{3.195}$$

The consistent tangent operator of the constitutive model arising of the viscoelastic or viscoelastic-viscoplastic state are given in Eqs. (3.187) and (3.190), respectively.

This methodology involves two iteration loops. The first one is for the classic stress return where the plastic multiplier $\Delta\lambda$, the damage variable D and the viscoelastic strain tensor $\underset{\sim}{\boldsymbol{\varepsilon}}^{\text{ve}}$ are unknown. The second iteration is for the plane stress condition enforcement where the unknown variable is $\varepsilon_{zz}^{\text{tr}}$. The complete algorithm of the viscoelastic-viscoplastic model implemented is described in Table 3.2.

The main advantage of this method is the non-modification of the viscoelastic predictor/viscoplastic return mapping scheme. With the implemented model, the cost of the solution is higher than the plane stress projected method, but it is more suitable for complex elastoplastic or viscoelastic-viscoplastic models. In order to highlight the efficiency of the implemented procedure with continuum shell elements, an example with analysis of the plane stress convergence is presented in the section concerning the validation of the constitutive model (Section 5.1).

[††]The following consistent tangent operator is written in matrix form.

Table 3.2: *Stress return algorithm (plane stress case).*

(i) Compute the initial trial thickness strain

$$\varepsilon^{\text{tr}\ 1}_{zz\ n+1} = -\left(\frac{\nu}{1-\nu}\right)\left(\varepsilon^{e}_{xx\ n+1} + \varepsilon^{e}_{yy\ n+1}\right)$$

(ii) Compute the effective viscoelastic trial stress

$$\tilde{\boldsymbol{\sigma}}^{\text{tr}}_{n+1} = \overset{\approx}{\mathscr{L}}{}^{\text{ve}}_{\infty} : \boldsymbol{\varepsilon}^{\text{tr}\ 1}_{n+1} + \sum_{i}^{N} \mathbf{h}^{\text{tr}}_{i\ n+1}$$

(iii) Check viscoplastic admissibility

$$\text{IF } f^{\text{vp tr}}_{n+1}\left(\tilde{\boldsymbol{\sigma}}^{\text{tr}}_{n+1}, \kappa_n\right) < 0$$

$$\text{THEN } (.)_{n+1} = (.)^{\text{tr}}_{n+1} \text{ and GOTO (vi)}$$

(iv) Viscoplastic stress return

$$\{\mathcal{W}\}^{k+1} = \{\mathcal{W}\}^{k} - \left[\frac{\partial \mathcal{R}^{k}}{\partial \Delta \mathcal{W}^{k}}\right]^{-1} \{\mathcal{R}\}^{k}$$

(v) Check convergence

$$\text{IF } \{\mathcal{R}\}^{k} \leq \{\mathcal{T}\} \text{ THEN GOTO (vi)}$$

$$\text{GOTO (iv)}$$

(vi) Check plane stress condition

$$\text{IF } \sigma_{zz\ n+1} \neq 0 \text{ THEN } \varepsilon^{\text{tr}\ i+1}_{zz\ n+1} = \varepsilon^{\text{tr}\ i}_{zz\ n+1} - \frac{\sigma^{i}_{zz\ n+1}}{\mathscr{L}^{i}_{22}} \text{ and GOTO (ii)}$$

(vii) Update stresses

$$\boldsymbol{\sigma}_{n+1} = (1 - D_{n+1})\tilde{\boldsymbol{\sigma}}_{n+1}$$

$$\mathbf{h}_{i\,n+1} = \exp\left(-\frac{\Delta t}{\tau_i}\right)\mathbf{h}_{i\,n} + \Xi_i \frac{1-\exp\left(-\frac{\Delta t}{\tau_i}\right)}{\frac{\Delta t}{\tau_i}}\left[\tilde{\boldsymbol{\sigma}}_{\infty\,n+1} - \tilde{\boldsymbol{\sigma}}_{\infty\,n}\right]$$

(viii) Store $\boldsymbol{\varepsilon}^{\text{ve}}_{n+1}$, κ_{n+1}, D_{n+1} , $\boldsymbol{\sigma}_{n+1}$, $\mathbf{h}_{i\,n+1}$

3.7 Extension of the constitutive model in finite strain

For infinitesimal deformations with small rotations, constitutive equations for elasto-plastic (or viscoelastic-viscoplastic) materials can be formulated in a rate form established by the material time derivative of the Cauchy stress tensor and the rate form of the deformation tensor. However, in the case of finite deformation with large deformations and rotations, objective stress rates retaining material frame indifference should be used instead of material time derivative of the stress tensor. The constitutive model described in the previous section is implemented in the large deformation finite element codes ABAQUS/Standard®(NLGEOM=yes) and LS-DYNA®. In this work, an hypoelas-

tic formulation is used in order to extend the constitutive model at finite strain. In this case, the constitutive equations are given on the additive decomposition of the rate of deformation tensor under the assumption that the elastic part (or viscoelastic) of the rate of deformation may be characterised with an hypoelastic law by using a fourth order constant isotropic tensor. Many objective stress rates are proposed in the literature and in the same large deformation finite element code, different stress rates can be used for different element formulations (e.g. in ABAQUS/Standard®, the Jaumann stress rate is used for solid elements and the Green-Naghdi stress rate is employed for continuum shell elements). In this work an unified stress update procedure in finite strain framework using the Green-Naghdi stress rate is established for the two finite element codes and for all the elements used.

3.7.1 Kinematics for large deformation continuum mechanics

A material point in reference configuration Ω_0 (not necessary the initial configuration) with position vector $\vec{\mathbf{X}}$ occupies position $\vec{\mathbf{x}}$ at time t in a deformed configuration Ω. The locations of the material point described by $\vec{\mathbf{X}}$ (Lagrangian description) and $\vec{\mathbf{x}}$ (Eulerian description) are related by the mapping ϕ as

$$\vec{\mathbf{x}} = \phi\left(\vec{\mathbf{X}}, t\right). \tag{3.196}$$

To describe the motion from the initial to the deformed configuration, the second order deformation gradient tensor is defined such as

$$\underset{\sim}{\mathbf{F}} = \frac{\partial \vec{\mathbf{x}}}{\partial \vec{\mathbf{X}}}. \tag{3.197}$$

The polar decomposition of the deformation gradient is given by

$$\underset{\sim}{\mathbf{F}} = \underset{\sim}{\mathbf{R}}\underset{\sim}{\mathbf{U}} = \underset{\sim}{\mathbf{V}}\underset{\sim}{\mathbf{R}} \tag{3.198}$$

where $\underset{\sim}{\mathbf{V}}$ and $\underset{\sim}{\mathbf{U}}$ are the left and right symmetric, positive definite stretch tensors, respectively. $\underset{\sim}{\mathbf{R}}$ is the rotation tensor which is an orthogonal tensor, resulting

$$\underset{\sim}{\mathbf{R}}^{\mathrm{T}}\underset{\sim}{\mathbf{R}} = \underset{\sim}{\mathbf{I}}. \tag{3.199}$$

The velocity gradient tensor $\underset{\sim}{\mathbf{L}}$ is defined by

$$\underset{\sim}{\mathbf{L}} = \frac{\mathrm{d}\phi\left(\vec{\mathbf{X}}, t\right)}{\mathrm{d}t} = \dot{\underset{\sim}{\mathbf{F}}}\underset{\sim}{\mathbf{F}}^{-1}. \tag{3.200}$$

The velocity gradient tensor can be decomposed into a symmetric $\underset{\sim}{\mathbf{D}}$ and antisymmetric $\underset{\sim}{\mathbf{W}}$ part, respectively, called rate of deformation and spin tensors as

$$\underset{\sim}{\mathbf{L}} = \underset{\sim}{\mathbf{D}} + \underset{\sim}{\mathbf{W}}. \tag{3.201}$$

The definition of the rate of deformation and spin tensors (symmetric and antisymmetric) leads to

$$\underset{\sim}{\mathbf{D}} = \frac{1}{2}\left(\underset{\sim}{\mathbf{L}} + \underset{\sim}{\mathbf{L}}^{\mathrm{T}}\right) \text{ and } \underset{\sim}{\mathbf{W}} = \frac{1}{2}\left(\underset{\sim}{\mathbf{L}} - \underset{\sim}{\mathbf{L}}^{\mathrm{T}}\right). \tag{3.202}$$

3.7.2 Hypoelastic formulation of the constitutive model

The major requirement in large deformation continuum mechanics is to achieve incremental objectivity. Many objective rates are introduced in literature, such as Jaumann, Truesdell or Green-Naghdi. The choice of an objective rate has been widely studied (Dienes, 1979; Johnson and Bammann, 1984; Nemat-Nasser, 1982). It results, that spurious stress oscillations under large shear elastic deformation is observed with the Jaumann rate based model. This problem can be overcome by using the Trusdell or Green-Naghdi rate models. Moss (1984) has shown the stress responses under finite shear deformation for the finite hypoelastic models defined by the Jaumann, Green-Naghdi and Truesdell rates. The general form of a hypoelastic relation is given by

$$\overset{\circ}{\underset{\sim}{\mathbf{T}}} = f\left(\underset{\sim}{\mathbf{T}}, \underset{\sim}{\mathbf{D}}\right) \tag{3.203}$$

where $\overset{\circ}{\underset{\sim}{\mathbf{T}}}$ represents any objective rate of a stress tensor. Let $\underset{\sim}{\boldsymbol{\Omega}}^*$ be a given spin tensor and $\underset{\sim}{\mathbf{T}}$ be a time-differentiable symmetric tensor, such as a stress tensor, the corotational rate of $\underset{\sim}{\mathbf{T}}$ defined by $\underset{\sim}{\boldsymbol{\Omega}}^*$ is given by

$$\overset{\circ}{\underset{\sim}{\mathbf{T}}} = \dot{\underset{\sim}{\mathbf{T}}} - \underset{\sim}{\boldsymbol{\Omega}}^*\underset{\sim}{\mathbf{T}} + \underset{\sim}{\mathbf{T}}\underset{\sim}{\boldsymbol{\Omega}}^*. \tag{3.204}$$

The corotational rates defined by the two spin tensors $\underset{\sim}{\boldsymbol{\Omega}}^* = \underset{\sim}{\mathbf{W}}$ and $\underset{\sim}{\boldsymbol{\Omega}}^* = \underset{\sim}{\boldsymbol{\Omega}}^{\mathrm{R}} = \dot{\underset{\sim}{\mathbf{R}}}\underset{\sim}{\mathbf{R}}^{\mathrm{T}}$, i.e.

$$\overset{\circ^{\mathrm{Z}}}{\underset{\sim}{\mathbf{T}}} = \dot{\underset{\sim}{\mathbf{T}}} - \underset{\sim}{\mathbf{W}}\underset{\sim}{\mathbf{T}} + \underset{\sim}{\mathbf{T}}\underset{\sim}{\mathbf{W}}, \tag{3.205}$$

$$\overset{\circ^{\mathrm{R}}}{\underset{\sim}{\mathbf{T}}} = \dot{\underset{\sim}{\mathbf{T}}} - \underset{\sim}{\boldsymbol{\Omega}}^{\mathrm{R}}\underset{\sim}{\mathbf{T}} + \underset{\sim}{\mathbf{T}}\underset{\sim}{\boldsymbol{\Omega}}^{\mathrm{R}} \tag{3.206}$$

provide two of several known examples of objective corotational rates, called the Zaremba-Jaumann and Green-Naghdi (polar) rate, respectively. In the two above relations, $\underset{\sim}{\mathbf{W}}$ is given in Eq. (3.201) and $\underset{\sim}{\mathbf{R}}$ arise from the polar decomposition of the deformation gradient (Eq. (3.198)). In the constitutive model, the Green-Naghdi objective corotational rate of the Cauchy stress is used. The corotational Green-Naghdi derivative of the Cauchy stress tensor is therefore defined such as

$$\overset{\circ}{\underset{\sim}{\sigma}} = \dot{\underset{\sim}{\sigma}} - \underset{\sim}{\Omega}^{R}\underset{\sim}{\sigma} + \underset{\sim}{\sigma}\underset{\sim}{\Omega}^{R}. \tag{3.207}$$

3.7.3 Incrementally objective stress integration of the constitutive model

In this work, the algorithm proposed by Simo and Hughes (1998) is extended to the visco-hypoelastic case in order to achieve the incremental objectivity with the viscoelastic-viscoplastic constitutive model. Let us define the Cauchy stress tensor and the rate deformation tensor rotated in the local configuration $\hat{\underset{\sim}{\sigma}}$ and $\hat{\underset{\sim}{\mathbf{D}}}$, respectively, such as

$$\hat{\underset{\sim}{\sigma}} = \underset{\sim}{\Lambda}^{T}\underset{\sim}{\sigma}\underset{\sim}{\Lambda}, \tag{3.208}$$

$$\hat{\underset{\sim}{\mathbf{D}}} = \underset{\sim}{\Lambda}^{T}\underset{\sim}{\mathbf{D}}\underset{\sim}{\Lambda} \tag{3.209}$$

where $\underset{\sim}{\Lambda}$ is the rotation tensor that solves the initial value problem

$$\begin{cases} \dot{\underset{\sim}{\Lambda}} = \underset{\sim}{\Omega}^{*}\underset{\sim}{\Lambda}, \\ \underset{\sim}{\Lambda}_{|t=0} = \underset{\sim}{\mathbf{I}}. \end{cases} \tag{3.210}$$

In the case of the Green-Naghdi stress rate, $\underset{\sim}{\Omega}^{*}$ is the polar spin tensor, i.e. $\underset{\sim}{\Omega}^{*} = \underset{\sim}{\Omega}^{R}$ and the exact solution is $\underset{\sim}{\Lambda} = \underset{\sim}{\Omega}^{R}$. In the developed model, the Henky strain (logarithmic) is used as strain measurement. Furthermore, the temporal integration of the rate deformation tensor $\underset{\sim}{\mathbf{D}}$ in the corotational frame gives a good approximation of the logarithmic strain measurement (Mora, 2004). The additive decomposition of the rate deformation tensor and of the Henky strain tensor $\underset{\sim}{\mathbf{e}}$ in a viscoelastic and viscoplastic part, in the local configuration, is assumed such as

$$\hat{\underset{\sim}{\mathbf{D}}} = \hat{\underset{\sim}{\mathbf{D}}}^{ve} + \hat{\underset{\sim}{\mathbf{D}}}^{vp}, \tag{3.211}$$

$$\hat{\underset{\sim}{\mathbf{e}}} = \hat{\underset{\sim}{\mathbf{e}}}^{ve} + \hat{\underset{\sim}{\mathbf{e}}}^{vp}. \tag{3.212}$$

Applying the generalised midpoint rule yields to

$$\begin{aligned}\hat{\underset{\sim}{\mathbf{e}}}_{n+1} &= \hat{\underset{\sim}{\mathbf{e}}}_{n} + \Delta t\, \hat{\underset{\sim}{\mathbf{D}}}_{n+1/2} \\ &= \hat{\underset{\sim}{\mathbf{e}}}_{n} + \Delta t \underset{\sim}{\boldsymbol{\Lambda}}^{\mathrm{T}}_{n+1/2} \underset{\sim}{\mathbf{D}}_{n+1/2} \underset{\sim}{\boldsymbol{\Lambda}}_{n+1/2}\end{aligned} \tag{3.213}$$

where $\underset{\sim}{\mathbf{D}}_{n+1/2}$ is defined by

$$\underset{\sim}{\mathbf{D}}_{n+1/2} = \frac{1}{2}\left(\underset{\sim}{\mathbf{L}}_{n+1/2} + \underset{\sim}{\mathbf{L}}^{\mathrm{T}}_{n+1/2}\right) \tag{3.214}$$

with

$$\underset{\sim}{\mathbf{L}}_{n+1/2} = \dot{\underset{\sim}{\mathbf{F}}}_{n+1/2} \underset{\sim}{\mathbf{F}}^{-1}_{n+1/2} \tag{3.215}$$

and

$$\underset{\sim}{\mathbf{F}}_{n+1/2} = \frac{1}{2}\left(\underset{\sim}{\mathbf{F}}_{n} + \underset{\sim}{\mathbf{F}}_{n+1}\right). \tag{3.216}$$

The total strain tensor rotated in the local configuration computed at the previous time step, $\hat{\underset{\sim}{\mathbf{e}}}_{n}$, is given following

$$\hat{\underset{\sim}{\mathbf{e}}}_{n} = \underset{\sim}{\boldsymbol{\Lambda}}^{\mathrm{T}}_{n} \underset{\sim}{\mathbf{e}}_{n} \underset{\sim}{\boldsymbol{\Lambda}}_{n}. \tag{3.217}$$

According to the viscoelastic model presented in the previous section, the visco-hypoelastic relation of the constitutive model rotated in the local configuration is given by[‡‡]

$$\begin{aligned}\tilde{\hat{\underset{\sim}{\boldsymbol{\sigma}}}}_{n+1} &= \underset{\approx}{\mathscr{L}}^{\mathrm{ve}}_{\infty} : \hat{\underset{\sim}{\mathbf{e}}}^{\mathrm{ve}}_{n+1} + \sum_{i=1}^{N} \hat{\underset{\sim}{\mathbf{h}}}_{i\,n+1} \\ &= \underset{\approx}{\mathscr{L}}^{\mathrm{ve}}_{\infty} : \left(\underset{\sim}{\boldsymbol{\Lambda}}^{\mathrm{T}}_{n} \underset{\sim}{\mathbf{e}}^{\mathrm{ve}}_{n} \underset{\sim}{\boldsymbol{\Lambda}}_{n} + \Delta t \underset{\sim}{\boldsymbol{\Lambda}}^{\mathrm{T}}_{n+1/2} \underset{\sim}{\mathbf{D}}^{\mathrm{ve}}_{n+1/2} \underset{\sim}{\boldsymbol{\Lambda}}_{n+1/2}\right) + \sum_{i=1}^{N} \hat{\underset{\sim}{\mathbf{h}}}_{i\,n+1}\end{aligned} \tag{3.218}$$

where the stress quantities $\hat{\underset{\sim}{\mathbf{h}}}_{i\,n+1}$ are defined as

$$\begin{aligned}\hat{\underset{\sim}{\mathbf{h}}}_{i\,n+1} &= \exp\left(-\frac{\Delta t}{\tau_i}\right) \hat{\underset{\sim}{\mathbf{h}}}_{i\,n} + \Xi_i \frac{1 - \exp\left(-\frac{\Delta t}{\tau_i}\right)}{\frac{\Delta t}{\tau_i}} \left[\tilde{\hat{\underset{\sim}{\boldsymbol{\sigma}}}}_{\infty\,n+1} - \tilde{\hat{\underset{\sim}{\boldsymbol{\sigma}}}}_{\infty\,n}\right] \\ &= \exp\left(-\frac{\Delta t}{\tau_i}\right) \underset{\sim}{\boldsymbol{\Lambda}}^{\mathrm{T}}_{n} \hat{\underset{\sim}{\mathbf{h}}}_{i\,n} \underset{\sim}{\boldsymbol{\Lambda}}_{n} + \Xi_i \frac{1 - \exp\left(-\frac{\Delta t}{\tau_i}\right)}{\frac{\Delta t}{\tau_i}} \left[\tilde{\hat{\underset{\sim}{\boldsymbol{\sigma}}}}_{\infty\,n+1} - \tilde{\hat{\underset{\sim}{\boldsymbol{\sigma}}}}_{\infty\,n}\right]\end{aligned} \tag{3.219}$$

with $\tilde{\hat{\underset{\sim}{\boldsymbol{\sigma}}}}^{n+1}_{\infty}$ and $\tilde{\hat{\underset{\sim}{\boldsymbol{\sigma}}}}^{n}_{\infty}$ are given by

$$\tilde{\hat{\underset{\sim}{\boldsymbol{\sigma}}}}^{n+1}_{\infty} = \underset{\approx}{\mathscr{L}}^{\mathrm{ve}}_{\infty} : \hat{\underset{\sim}{\mathbf{e}}}^{\mathrm{ve}}_{n+1} = \underset{\approx}{\mathscr{L}}^{\mathrm{ve}}_{\infty} : \left(\underset{\sim}{\boldsymbol{\Lambda}}^{\mathrm{T}}_{n} \underset{\sim}{\mathbf{e}}^{\mathrm{ve}}_{n} \underset{\sim}{\boldsymbol{\Lambda}}_{n} + \Delta t \underset{\sim}{\boldsymbol{\Lambda}}^{\mathrm{T}}_{n+1/2} \underset{\sim}{\mathbf{D}}^{\mathrm{ve}}_{n+1/2} \underset{\sim}{\boldsymbol{\Lambda}}_{n+1/2}\right), \tag{3.220}$$

$$\tilde{\hat{\underset{\sim}{\boldsymbol{\sigma}}}}^{n}_{\infty} = \underset{\approx}{\mathscr{L}}^{\mathrm{ve}}_{\infty} : \hat{\underset{\sim}{\mathbf{e}}}^{\mathrm{ve}}_{n} = \underset{\approx}{\mathscr{L}}^{\mathrm{ve}}_{\infty} : \underset{\sim}{\boldsymbol{\Lambda}}^{\mathrm{T}}_{n} \underset{\sim}{\mathbf{e}}^{\mathrm{ve}}_{n} \underset{\sim}{\boldsymbol{\Lambda}}_{n}. \tag{3.221}$$

[‡‡] $\tilde{\hat{\underset{\sim}{\boldsymbol{\sigma}}}}_{n+1}$ defines the effective stress tensor rotated in the local configuration.

The effective Cauchy stress tensor at t_{n+1} is then obtained simply by rotating back to the spatial configuration as follows

$$\tilde{\boldsymbol{\sigma}}_{n+1} = \boldsymbol{\Lambda}_{n+1}\tilde{\tilde{\boldsymbol{\sigma}}}_{n+1}\boldsymbol{\Lambda}^{\mathrm{T}}_{n+1}. \tag{3.222}$$

Finally, substituting Eqs. (3.220)-(3.222) into Eq. (3.219), the visco-hypoelastic relation of the constitutive model can be formulated entirely in the spatial configuration such as

$$\tilde{\boldsymbol{\sigma}}_{n+1} = \mathcal{L}^{\mathrm{ve}}_{\infty} : \left(\boldsymbol{\Lambda}_{\Delta}\mathbf{e}^{\mathrm{ve}}_{n}\boldsymbol{\Lambda}^{\mathrm{T}}_{\Delta} + \Delta t\boldsymbol{\Lambda}_{\delta}\mathbf{D}^{\mathrm{ve}}_{n+1/2}\boldsymbol{\Lambda}^{\mathrm{T}}_{\delta}\right) + \sum_{i=1}^{N}\mathbf{h}_{i\,n+1}, \tag{3.223}$$

$$\mathbf{h}_{i\,n+1} = \exp\left(-\frac{\Delta t}{\tau_i}\right)\boldsymbol{\Lambda}_{\Delta}\mathbf{h}_{i\,n}\boldsymbol{\Lambda}^{\mathrm{T}}_{\Delta} + \Xi_i\frac{1-\exp\left(-\frac{\Delta t}{\tau_i}\right)}{\frac{\Delta t}{\tau_i}}\left[\tilde{\boldsymbol{\sigma}}_{\infty\,n+1} - \tilde{\boldsymbol{\sigma}}_{\infty\,n}\right], \tag{3.224}$$

$$\tilde{\boldsymbol{\sigma}}^{n+1}_{\infty} = \mathcal{L}^{\mathrm{ve}}_{\infty} : \left(\boldsymbol{\Lambda}_{\Delta}\mathbf{e}^{\mathrm{ve}}_{n}\boldsymbol{\Lambda}^{\mathrm{T}}_{\Delta} + \Delta t\boldsymbol{\Lambda}^{\mathrm{T}}_{\delta}\mathbf{D}^{\mathrm{ve}}_{n+1/2}\boldsymbol{\Lambda}^{\mathrm{T}}_{\delta}\right), \tag{3.225}$$

$$\tilde{\boldsymbol{\sigma}}^{n}_{\infty} = \mathcal{L}^{\mathrm{ve}}_{\infty} : \boldsymbol{\Lambda}_{\Delta}\mathbf{e}^{\mathrm{ve}}_{n}\boldsymbol{\Lambda}^{\mathrm{T}}_{\Delta} \tag{3.226}$$

where $\boldsymbol{\Lambda}_{\Delta}$ and $\boldsymbol{\Lambda}_{\delta}$ are given by

$$\boldsymbol{\Lambda}_{\Delta} = \boldsymbol{\Lambda}_{n+1}\boldsymbol{\Lambda}^{\mathrm{T}}_{n}, \tag{3.227}$$

$$\boldsymbol{\Lambda}_{\delta} = \boldsymbol{\Lambda}_{n+1}\boldsymbol{\Lambda}^{\mathrm{T}}_{n+1/2}. \tag{3.228}$$

The visco-hypoelastic prediction is therefore given by assuming the total rate deformation tensor $\mathbf{D}$ like purely viscoelastic and if the current stress does not lie in the yield surface, as in the small strain framework, the classic viscoplastic stress return algorithm takes place. In this case, the aim is to evaluate the viscoplastic part of the rate deformation tensor $\mathbf{D}^{\mathrm{vp}}$ and the new damage variable D_{n+1} in order to compute the new effective stress tensor such as

$$\tilde{\boldsymbol{\sigma}}_{n+1} = \tilde{\boldsymbol{\sigma}}^{\mathrm{tr}}_{n+1} - \mathcal{L}^{\mathrm{e}} : \Delta t\mathbf{D}^{\mathrm{vp}}. \tag{3.229}$$

With the proposed implementation in finite strain framework by means of an hypoelastic formulation with a Green-Naghdi objective stress rate, the viscoplastic stress return algorithm developed previously under infinitesimal strain remains unchanged. The difference is in the viscoelastic prediction where the previous tensors ($\mathbf{e}^{\mathrm{ve}}_{n}$ and $\mathbf{h}_{i\,n}$) are rotated in the spatial configuration by using the rotation tensor $\boldsymbol{\Lambda}_{\Delta}$ and the incremental strain tensor arise from the rate deformation tensor $\mathbf{D}$ (Eq. (3.214)) which is rotated in the spatial configuration by using the rotation tensors $\boldsymbol{\Lambda}_{\delta}$ as well. The rotation tensor are computed from

Table 3.3: *Stress return algorithm (finite strain case).*

(i) Compute $\underset{\sim}{\mathbf{R}}_n$, $\underset{\sim}{\mathbf{R}}_{n+1/2}$, $\underset{\sim}{\mathbf{R}}_{n+1}$ by polar decomposition.

(ii) Compute $\underset{\sim}{\Omega}^{\mathrm{R}}_n$, $\underset{\sim}{\Omega}^{\mathrm{R}}_{n+1/2}$, $\underset{\sim}{\Omega}_{n+1^{\mathrm{R}}}$

$$\underset{\sim}{\Omega}^{\mathrm{R}}_n = \dot{\underset{\sim}{\mathbf{R}}}_n \underset{\sim}{\mathbf{R}}^{\mathrm{T}}_n, \quad \underset{\sim}{\Omega}^{\mathrm{R}}_{n+1/2} = \dot{\underset{\sim}{\mathbf{R}}}_{n+1/2} \underset{\sim}{\mathbf{R}}^{\mathrm{T}}_{n+1/2}, \quad \underset{\sim}{\Omega}^{\mathrm{R}}_{n+1} = \dot{\underset{\sim}{\mathbf{R}}}_{n+1} \underset{\sim}{\mathbf{R}}^{\mathrm{T}}_{n+1}$$

(iii) Compute the rotation tensors $\underset{\sim}{\Lambda}_{\Delta}$, $\underset{\sim}{\Lambda}_{\delta}$.

$$\underset{\sim}{\Lambda}_{\Delta} = \underset{\sim}{\Lambda}_{n+1} \underset{\sim}{\Lambda}^{\mathrm{T}}_n, \quad \underset{\sim}{\Lambda}_{\delta} = \underset{\sim}{\Lambda}_{n+1} \underset{\sim}{\Lambda}^{\mathrm{T}}_{n+1/2}$$

(iv) Compute the viscoelastic trial strain tensor in spatial configuration

$$\underset{\sim}{\mathbf{e}}^{\mathrm{ve\ tr}}_{n+1} = \underset{\sim}{\Lambda}_{\Delta} \underset{\sim}{\mathbf{e}}^{\mathrm{ve}}_n \underset{\sim}{\Lambda}^{\mathrm{T}}_{\Delta} + \Delta t \underset{\sim}{\Lambda}_{\delta} \underset{\sim}{\mathbf{D}}^{\mathrm{ve}}_{n+1/2} \underset{\sim}{\Lambda}^{\mathrm{T}}_{\delta}$$

(v) Small strain algorithm

GOTO Table 3.2 (Shell elements)

GOTO Table 3.1 (Solid elements)

the polar decomposition[§§] of the deformation gradient tensor at time t_n, t_{n+1} and t_n. The complete algorithm of the implemented constitutive model at finite strain is given in Table 3.3

3.8 Nonlocal formulation of the damage model

The nucleation and growth of micro-voids and micro-cracks during the deformation of filled polymer materials under tensile loading induce a softening behaviour. The decrease of the stress at increasing strain leads to well known numerical problem where the deformation is localised in a narrow zone. The numerical response arising from finite element simulation using standard continuum plasticity with material exhibiting softening leads to a spurious mesh dependence phenomenon. The mesh dependence problem is due to the loss of ellipticity of the governing equilibrium equations in the static case and of hyperbolicity in the dynamic case. In order to overcome the spurious mesh dependency, a viscoplastic formulation can be used as in the works of Voyiadjis and Abed (2006). Viscoplastic formulation can reduce the mesh dependency pathology even for slightly viscous material. Further example presented in Chapter 5 shows that the proposed viscoplastic model

[§§]The closed form algorithm of the polar decomposition given by Simo and Hughes (1998) is used for the implementation of the model.

is able to obtain a mesh-independent solution when the deformations are not so localised as in a straight specimen loaded in tension. Nevertheless, for more localised deformations, as in a notched specimen, the viscoplastic model does not overcome the mesh-dependent problem. These results are in accordance with Besson *et al.* (2001) where the authors have noted that the problem of simulation of localisation phenomena in not really solved by introducing viscosity. In order to overcome the spurious mesh dependency, an integral-type nonlocal model (Pijaudier-Cabot and Bažant, 1987; Strömberg and Ristinmaa, 1996; Jirásek and Rolshoven, 2003), where a damage variable defined by a spacial averaging, is used in the constitutive model.

3.8.1 Concept of nonlocality

The nonlocal variable in a material point $\vec{x}$ is mathematically defined as a weighted average of the local values a in all material points of the body Ω such as,

$$\bar{a}(\vec{x}) = \frac{1}{\psi(\vec{x})} \int_{\Omega} \psi(\vec{x};\vec{y}) a(\vec{y}) \mathrm{d}\Omega(\vec{y}) \tag{3.230}$$

where $\bar{a}$ denotes the nonlocal quantity and $\vec{y}$ is the position vector of the small volume Ω (or area in the two dimensional case). $\psi(\vec{x};\vec{y})$ is a Gaussian type weight function given by

$$\psi(\vec{x};\vec{y}) = \frac{1}{c} \exp\left(-\frac{r^2}{2l^2}\right) \tag{3.231}$$

where the scaling factor c depends on the problem dimension. c is defined by $\sqrt{2\pi}l$ for one dimension, $2\pi l^2$ for two dimensions and $\sqrt{\frac{\pi^3}{2}}l^3$ for the three dimensional case. The weight function depends only on the distance $r = \|\vec{x}-\vec{y}\|$. The intrinsic length l determines the size of the volume which effectively contributes to the nonlocal quantity. In the above integral, the local continuum viscoplasticity is retrieved if l tends towards zero. In order to have a nonlocal quantity $\bar{a}$ equals to its corresponding local quantity a for homogeneous local values, the normalizing factor $\psi(\vec{x})$ introduced in Eq. (3.230) is given by

$$\psi(\vec{x}) = \int_{\Omega} \psi(\vec{y};\vec{x}) \mathrm{d}\Omega. \tag{3.232}$$

In the nonlocal theory, the assumption of an averaging operator $\psi(\vec{y};\vec{x})$ which is independent of the history of the deformation is assumed,

$$\frac{\partial \psi(\vec{x};\vec{y})}{\partial t} = 0. \tag{3.233}$$

Under infinitesimal strain framework, the nonlocal averaging is independent of the configuration due to the negligible difference between the undeformed and the deformed configuration. However, under finite strains the definition of the averaging operator on the deformed or undeformed configuration leads to different results. In this case, three different strategies for the nonlocal averaging can be considered: Eulerian type, total Lagrangian type and updated Lagrangian type. In the Eulerian type, the averaging operator is evaluated on the deformed configuration. In the total Lagrangian type, the averaging operator is evaluated on the undeformed configuration and the updated Lagrangian method considers constant the averaging operator but only over the increment of the deformation. In a computational point of view, the choice of the type of averaging has a strong influence on the efficiency. In the total Lagrangian type, the averaging operator $\psi(\vec{x};\vec{y})$ is evaluated once contrary to the Eulerian and updated Lagrangian methods which need to compute $\psi(\vec{x};\vec{y})$ at each time step. Andrade *et al.* (2011) have shown that all the three definitions, Eulerian type, total Lagrangian type and updated Lagrangian type lead to distinct but regularised solutions. In this work, a total Lagrangian type averaging is considered for the significant computational time saved in comparison to the two other theories.

3.8.2 Nonlocal isotropic damage model

In the nonlocal theory, different nonlocal variables which affect the softening can be considered like the equivalent plastic strain or the damage variable. In the constitutive model, a nonlocal damage $\bar{D}$ is considered in order to enhance the numerical response with a material exhibiting softening. In a classic nonlocal isotropic damage model, the local damage variable D is replaced by its nonlocal value $\bar{D}$ calculated by Eq. (3.230). The numerical implementation of an integral-type nonlocal model requires to have access to all the integration points of the finite element mesh in order to satisfy the consistency conditions of the material model in all the material points at the end of the time step. Unfortunately, in a user-material provided by most of commercial finite element codes, the informations of all the integration points are not available at the same time. Furthermore, from the nonlocal nature of the constitutive equations, the calculus of the tangent modulus becomes complex. An alternative nonlocal formulation proposed by Tvergaard and Needleman (1995); Needleman and Tvergaard (1998) is used in order to overcome these difficulties. The above authors have proposed a nonlocal version of the Gurson model where the local variable representing the void volume fraction $\dot{f}$ is replaced by $\mathbb{K}\dot{f}$, where $\mathbb{K} = \dot{\bar{f}}/\dot{f}$. The penalty factor $\mathbb{K}$ is therefore the ratio between a local and a nonlocal quantity calculated at the previous time step. With this nonlocal formulation, the above authors have noted that the mesh sensitivity have been completely removed for a sufficiently fine mesh relative to the

material intrinsic length.
Following the above concept, the nonlocal damage variable used in the constitutive model is therefore defined by substituting the nonlocal quantity $\mathbb{K}\dot{D}_{n+1}$ instead of the local damage rate $\dot{D}_{n+1}$. The quantity $\mathbb{K}$ is also computed by

$$\mathbb{K} = \frac{\dot{\bar{D}}_n}{\dot{D}_n} \tag{3.234}$$

where $\dot{\bar{D}}_n$ is the nonlocal damage rate calculated with the averaging operator (Eq. (3.230)) from the local damage rate $\dot{D}_n$ arising of the previous time step. With this formulation, only the scalar $\mathbb{K}$ is introduced in the constitutive equations and the viscoelastic-viscoplastic return scheme and the tangent modulus are similar to the local material model (Section. 3.5). By using the isotropic damage model introduced in Section. 3.3 (Eq. (3.144)), the residual linked to the damage which needs vanish during the viscoplastic stress return becomes

$$\mathcal{R}_D = \Delta D - \mathbb{K}\frac{\sqrt{\frac{2}{3}\underset{\sim}{\mathbf{n}}_{n+1} : \underset{\sim}{\mathbf{n}}_{n+1}}}{k_c} \exp\left(-\frac{\kappa_{n+1}}{k_c}\right)\Delta\lambda. \tag{3.235}$$

All the other equations of the system (Eq. (3.180)) which need to be solved during the viscoplastic stress return remain unchanged.

3.8.3 Implementation of the nonlocal damage model

According the definition of the nonlocal damage rate variable of a material point x written in incremental form $\Delta\bar{D}(x)$, the averaging operator is equal to the sum of the integrals over the individual finite elements over all the volume of the structure such as

$$\Delta\bar{D}(x) = \frac{1}{\psi(x)}\sum_{i=1}^{ne}\sum_{j=1}^{ng}\psi(x; y_{ij})\Delta D(y_{ij})V_y \tag{3.236}$$

where ne and ng are the number of elements and integration points on each element, respectively. V_y is the volume of the element which contains the material point y. In the same way $\psi(x)$ is computed following

$$\psi(x) = \sum_{i=1}^{ne}\sum_{j=1}^{ng}\psi(x; y_{ij})V_y. \tag{3.237}$$

The calculus of the nonlocal quantity can therefore be fulfilled in matrix form such as

$$[\Delta\bar{D}] = [\mathscr{X}][\Delta D] \tag{3.238}$$

Table 3.4: *Stress return algorithm of the constitutive model (nonlocal case).*

(i) **First time step only:**

$$[\mathscr{X}] = \frac{1}{\psi(x)} \sum_{i=1}^{ne} \sum_{j=1}^{ng} \psi(x; y_{ij})(y_{ij}) V_y$$

(ii) **After the first time step:**

$$[\Delta \bar{D}_n] = [\mathscr{X}][\Delta D_n]$$

$$\mathbb{K} = \frac{\Delta \bar{D}_n}{\Delta D_n}$$

(iii) Local stress return algorithm with $\Delta D - \mathbb{K} \frac{\sqrt{\frac{2}{3} \underset{\sim}{\mathbf{n}}_{n+1} : \underset{\sim}{\mathbf{n}}_{n+1}}}{k_c} \exp\left(-\frac{\kappa_{n+1}}{k_c}\right) \Delta\lambda = 0$

GOTO Table 3.3 (Finite strains)

where the matrix $[\mathscr{X}]$ is given by

$$[\mathscr{X}] = \frac{1}{\psi(x)} \sum_{i=1}^{ne} \sum_{j=1}^{ng} \psi(x; y_{ij})(y_{ij}) V_y. \tag{3.239}$$

In a numerical point of view, the matrix $[\mathscr{X}]$ is computed once at the first time step since the type of averaging formulation adopted in the constitutive model is totally Lagrangian. With this procedure, few modifications of the local constitutive model are performed to obtain a nonlocal regularisation which enhance the results of finite element simulations carried out which a material exhibiting softening. The complete implementation procedure of the constitutive model with the nonlocal damage model is summarised in Table 3.4.

3.9 Conclusions

In this chapter, the non-associated viscoelastic-viscoplastic model coupled with isotropic continuum damage has been presented. The constitutive model presents an hydrostatic pressure dependent yield surface able to reproduce different behaviours under tensile and compressive loadings. The increase of the stiffness at increasing strain rate are modelled by using the linear viscoelastic Wiechert model. The viscoplastic formulation ensures the influence of the strain rate on the yield stress and the hardening/softening of the material. Since the material being studied is a mineral filled polymer, the nucleation and growth of micro-voids and micro-cracks leads to a non-isochoric viscoplastic deformation which is taken into account with the nonassociativeness coupled with isotropic damage. The implementation of the constitutive model under finite strain framework in the implicit and

the explicit finite element codes ABAQUS/Standard® and LS-DYNA®, respectively, in a user-material subroutine written in FORTRAN® 77 is developed. Due to the large deformations and/or rotations induced under finite strain, the hypoelastic formulation based on the Green-Naghdi stress rate is used in the constitutive model in order to achieve the incremental objectivity. The particular implementation of the constitutive equations with continuum shell elements where the zero-stress condition needs to be fulfilled, is carried out by using a second iteration loop where the out of plane strain component is updated until the plane stress condition is reached. Furthermore in order to overcome the mesh dependence pathology caused by the softening, a nonlocal extension of the damage model in a integral-type form is proposed. The implementation of the nonlocal constitutive equations is carried out in a simple manner by introducing a scalar relating the nonlocal averaging computed from the values which arise to the previous time step. With this method, the local viscoelastic-viscoplastic return scheme remains unchanged.

Chapter 4

Experimental procedure and parameter identification

In order to characterise the viscoelastic-viscoplastic behaviour of the material, some experimental tests are carried out at various loading conditions and speed loadings. The viscoelastic parameters are deduced from DMA analysis where the material is loaded with an imposed sinusoidal strain. The non-isochoric viscoplastic behaviour, the pressure dependency and the damage evolution of the polymer being studied are characterised by monotonic tests at various strain rates and loading conditions (tension and compression). Some measurement techniques using optical extensometry and Digital Image Correlation are used for the displacement measurements. The identification of the model parameters (damage, plastic flow, hydrostatic pressure and behaviour law) is performed directly from experimental data. The identification of the behaviour law is done in tension by using the SEĖ method (Lauro *et al.*, 2010). With this measurement technique, the true stress-strain laws at constant strain rate are calculated for a large strain rate range. The flow and damage parameters used in the constitutive model are deduced from the SEĖ method results as well. Furthermore, a comparison between the damage characterised from the SEĖ method with a classic measurement by loss of stiffness during an uniaxial tensile test with repeated unloadings is presented in this chapter. Finally an in-situ X-ray microtomography tensile test is presented at the end of this chapter where the aim is to measure the real and effective cross sections of the specimen loaded in order to measure the damage occurring during the deformation.

4.1 Presentation of the material

The material under investigation is a 20% mineral filled polypropylene co-polymer, currently used for automotive applications. The polypropylene (PP) is a semi-crystalline polymer composed by the following repetition of chemical units

$$\left[\begin{array}{cccc} & & CH_3 & \\ & & | & \\ -CH_2 & - & CH & \end{array} \right]_N .$$

Its glass transition temperature (T_g) is −18°C and its melting point (T_m) is between 160 and 168°C. In this work, the adiabatic deformation of the material is considered and all the material investigations are done between T_g and T_m. Nevertheless, the auto-heating of the material during the deformation is introduced directly in the behaviour law of the material by using the SEÈ method (Lauro *et al.*, 2010) for its identification. The polypropylene is filled with around 20% of mineral charges. Table 4.1 shows the mechanical properties of the material studied given by the manufacturer, characterised from uniaxial tensile tests carried out at 50 mm.min^{-1} and at constant temperature 20°C.

Table 4.1: *Mechanical properties of the mineral filled polypropylene studied.*

Density (g/cm^3)	Young modulus (MPa)	Yield stress (MPa)	Yield strain(%)
1.04	2200	27	5.0

4.2 Experimental procedure

Polypropylene (PP) behaviour is well known to be highly sensitive to relative humidity of the air and temperature. The material is therefore conserved at a constant humidity of the air (50 %) and at a constant temperature (20°C). Excepted for the DMA analysis, where only one specimen is used per frequency, for each loading (tension and compression) and each speed loading, 5 specimens are tested. Only the most representative test is used for the result analysis.

4.2.1 Dynamic Mechanical Analysis

The viscoelastic properties of the polypropylene being studied are measured by means of small amplitude tensile experiments*. The deformation is applied sinusoidally with an an-

*For convenience, in the two sections concerning the DMA tests (Section. 4.2.1 and 4.3) the small strain notation is used. The different definitions of strains become equivalent at very small deformations.

gular frequency ω. The input is of the form,

$$\varepsilon(t) = \varepsilon_0 \cos(\omega t) = \varepsilon_0 R_e \{\exp(i\omega t)\} \tag{4.1}$$

where ε_0 is the strain amplitude and t is the time. R_e represents only the real part. When the amplitude is small, the stress will be sinusoidal with frequency ω, but with a different amplitude and not in phase with the strain input (Fig. 4.1) such as,

$$\sigma(t) = \sigma_0 \cos((\omega t) + \delta) = \sigma_0 R_e \{\exp(i(\omega t + \delta))\}. \tag{4.2}$$

The ratio of stress and strain gives the complex modulus E^* which is frequency dependent,

$$E^*(i\omega) = \frac{\sigma_0}{\varepsilon_0} \exp(i\delta). \tag{4.3}$$

E^* can be split into a real component E', so-called storage modulus, which is in phase with the strain (elastic response) and an imaginary component E'', i.e. the loss modulus, which is $\frac{\pi}{2}$ radians out of phase with the strain input (viscous response) as follows

$$E^* = E' + iE''. \tag{4.4}$$

The storage and loss modulus are defined by

$$E' = \frac{\sigma_0}{\varepsilon_0} \cos(\delta), \tag{4.5}$$

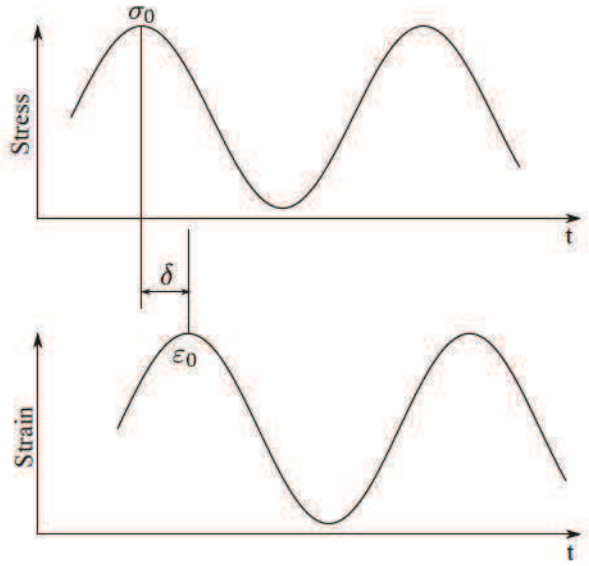

Figure 4.1: *Input and output for a steady state vibration test.*

$$E'' = \frac{\sigma_0}{\varepsilon_0} \sin(\delta). \tag{4.6}$$

The ratio of the loss modulus to the storage modulus (i.e. $\tan\delta$) is a measurement of the elastic and/or viscous response of the material. The loss angle δ is defined by

$$\tan\delta = \frac{E''}{E'}. \tag{4.7}$$

When δ approaches zero the viscoelastic material behaviour tends towards to an elastic rubber, when δ approaches $\frac{\pi}{2}$ it tends towards to a simple liquid.
The dynamic moduli are measured by means of small amplitude oscillatory tension experiments, conducted on an electromagnetic device (INSTRON E3000) with a 3 kN cell force. For these tests, flat rectangular shape specimens (50*10 mm) with a thickness of 3.2 mm are used. The experiments were conducted at room temperature (20°C) at several frequencies between 0.01 and 40 H_z. One specimen per frequency is used for these tests. The experimental data are shown in Figs. 4.2-4.4. As expected, the storage modulus increases with increasing frequency. On the other hand the loss modulus and the loss angle decreases with increasing frequency.

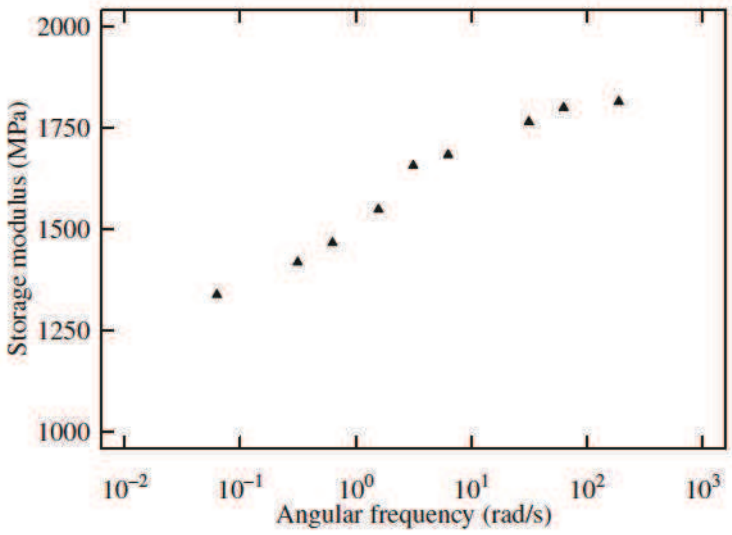

Figure 4.2: *Storage modulus versus angular frequency.*

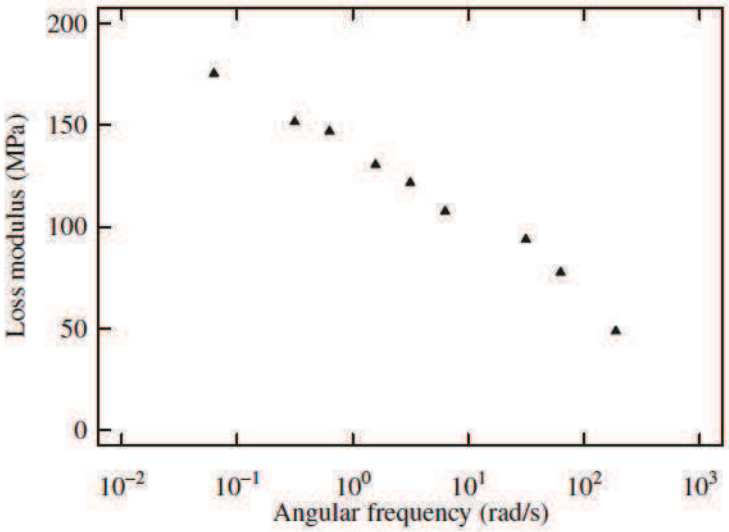

Figure 4.3: *Loss modulus versus angular frequency.*

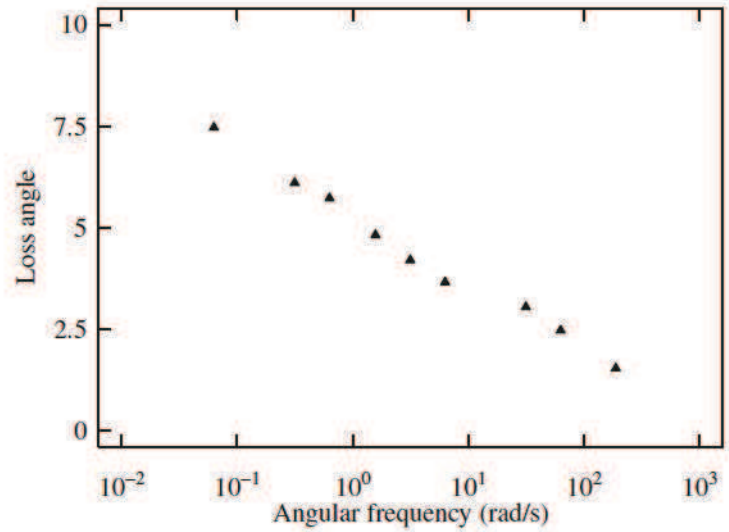

Figure 4.4: *Loss angle versus angular frequency.*

4.2.2 Tensile tests with normalised specimens

The uniaxial tensile tests are carried out at room temperature on an electromagnetic device (INSTRON E3000) for the quasi-static case with a 3 kN cell force. An hydraulic high speed device (INSTRON 65/20) is used for the dynamic loadings with a 5 kN cell force. The tensile specimens are cut using the water-jet technique, their shape and dimensions, given by the norm AM 3 510, are shown in Fig. 4.5. In quasi-static, 2 speed loadings are carried out (1 and 100 mm.min^{-1}) and 3 speed loadings in dynamic (0.08, 0.8 and 4 m.s^{-1}) which correspond

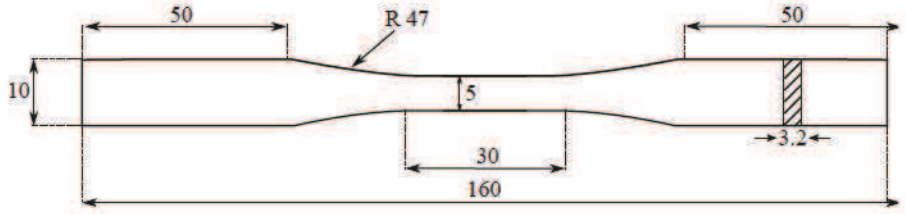

Figure 4.5: *Tensile specimen geometry (all dimensions are in mm).*

to approximate equivalent strain rates of respectively 5.5 10^{-4}, 5.5 10^{-2}, 2.6, 26.6 and 133 s^{-1}. The 2D Digital Image Correlation is employed for the strain field measurement with high speed cameras (PHOTRON APX 3000) (Fig. 4.6(a)). The Digital Image Correlation measures the displacement fields on the surface of the specimens between two pictures, by using an artificial texture obtained by painting the surface of the specimen with black and white colors in order to obtain different grey scale levels (Fig. 4.6(b)). In order to make the comparison between the different tests, the results are given in terms of engineering stress-strain. The engineering stress (Σ) is obtained by (considering $\vec{y}$ the longitudinal axis)

$$\Sigma_{yy} = \frac{F}{S_0} \tag{4.8}$$

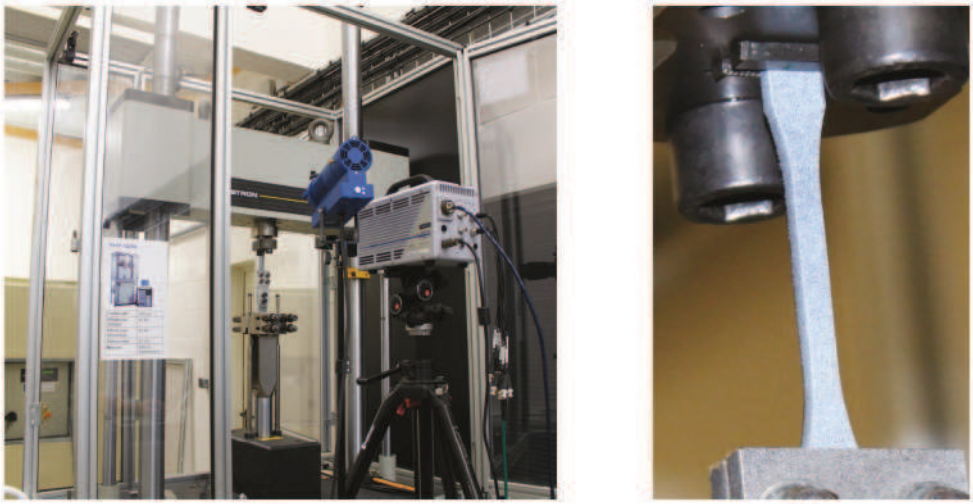

(a) (b)

Figure 4.6: *Displacement field measurements by DIC in tension: uniaxial tensile test on hydraulic high speed device with high speed camera (a) and artificial texture on uniaxial tensile specimen for DIC measurement (b).*

where F is the force given by the cell and S_0 is the initial cross-section of the specimen. The engineering strain (Γ) is given by

$$\Gamma_{yy} = \frac{U_{yy}}{l_0} \tag{4.9}$$

where U_{yy} is the displacement and l_0 is the initial length of the specimen.
The engineering stress-strain curves of the polypropylene studied in uniaxial tensile loading are shown in Fig. 4.7.

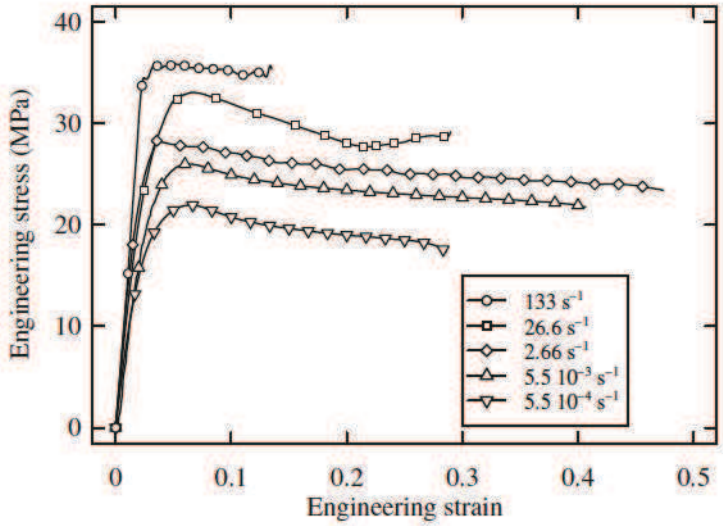

Figure 4.7: *Strain rate sensitivity on uniaxial tensile loading.*

The stress response increases non-linearly as the strain rate increases. The yield stress increases clearly with the strain rate but the hardening slope is relatively similar for all the loading speeds. Due to the oscillations produced by the high speed hydraulic device, the response of the cell force gives noisy results. A numerical smooth is therefore applied as illustrated in Fig. 4.8. This numerical smooth is based on a local regression using weighted linear least squares and a 2nd degree polynomial model, the method assigns lower weight to outliers in the regression and zero weight to data outside six mean absolute deviations. The uniaxial quasi-static tensile tests at 1 mm.min^{-1} are carried out with two cameras, one for the front and the other for the thickness specimen measurement. This procedure is used to measure the volume variation during the tests.
In order to be consistent with the constitutive model where the Cauchy stress and the Henky (logarithmic) strain measurement are used, the true strains coming from the digital image software VIC 2D®(Fig. 4.9(a)) are calculated such as

$$\underset{\sim}{\mathbf{e}} = \frac{1}{2}\log\left(\underset{\sim}{\mathbf{F}}^{\mathrm{T}}\underset{\sim}{\mathbf{F}}\right) \tag{4.10}$$

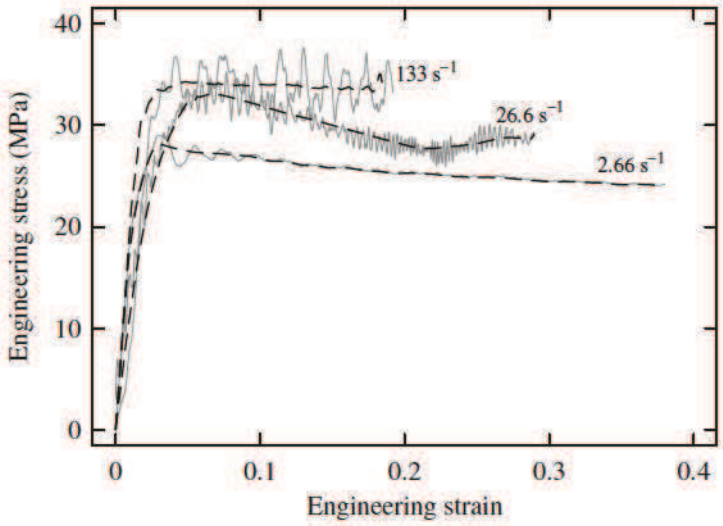

Figure 4.8: *Comparison between noisy and smoothed data.*

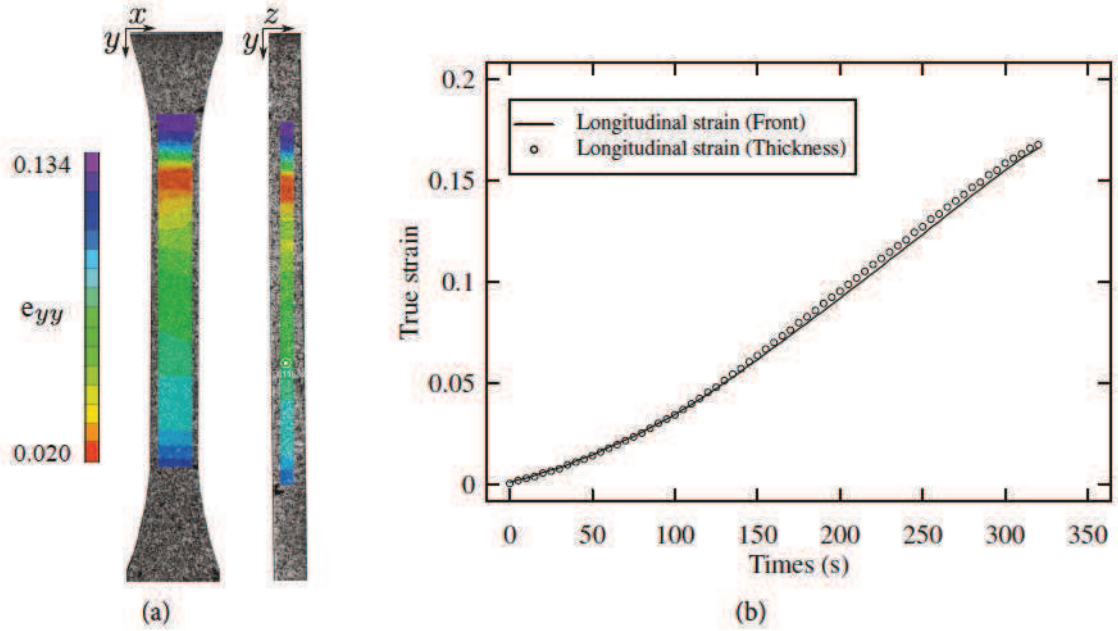

Figure 4.9: *Henky strain measurements by DIC in tension with 2 cameras: axial logarithmic strain measurements on the both side of the specimen (a) and comparison of true longitudinal strains measured on the front and the thickness of the specimen (b).*

where $\underset{\sim}{F}$ is the deformation gradient. For the Digital Image Correlation measurements, the Region Of Interest (ROI) is divided in Zone Of Interest (ZOI) and the size of the ZOI influences the calculus of the strain value. The same size of ZOI is used in the front and the thickness analysis in order to make the comparison. The longitudinal strains are measured

on the both sides of the specimen (front and thickness) at the same vertical position on the specimen (where the longitudinal strain is higher). Fig. 4.9(b) shows the comparison of true axial strains measured on the front and on the thickness of the specimen. The two strains calculated are very close, this base of measurement is also used for the following non-isochoric characterisation. A transverse isotropy is observed during the tensile test, indeed, as shown in Fig. 4.10, the transverse strain (e_{xx}) is very close to the out of plane strain component (e_{zz}). Fig. 4.11 shows the true volumetric strain (i.e. $tr(\underline{\mathbf{e}})$) in function

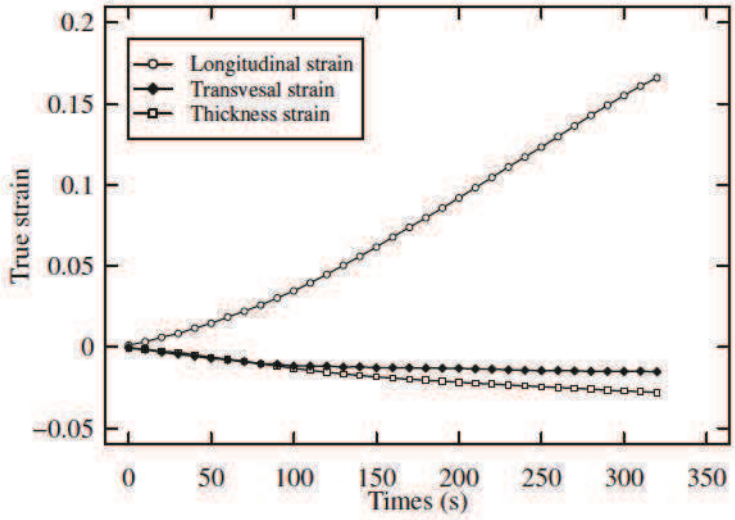

Figure 4.10: *True strains measured by DIC in uniaxial tensile loading on a PP at 1 mm.min*$^{-1}$.

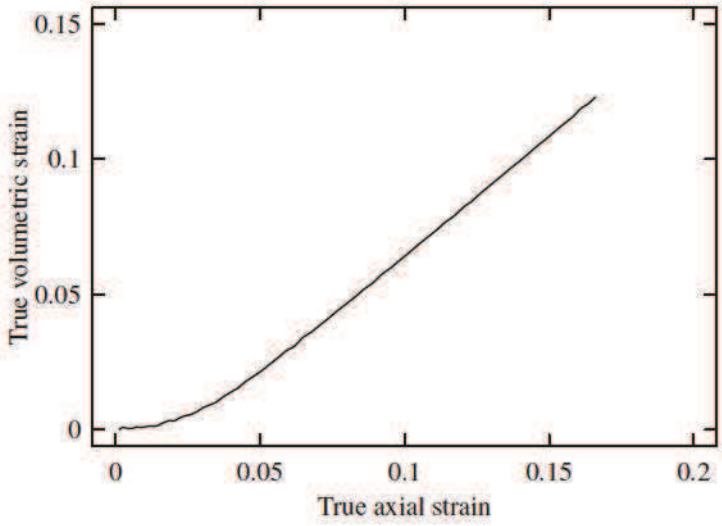

Figure 4.11: *Volumetric strain vs. true axial strain measured by DIC in uniaxial tensile loading on a PP at 1 mm.min*$^{-1}$.

of the true axial strain during the test. With this measurement technique, the non-isochoric viscoplastic deformation is well captured. This common behaviour of the polypropylene needs to be taken into account in the constitutive model.

4.2.3 Hopkinson tensile tests

The testing technique using direct Hopkinson bars is carried out with an input and output aluminum bars (diameter 20 mm) and a polyamide striker (PA66). The length of the input, output bar and the striker are respectively 5.96, 4 and 1 m. The input bar is instrumented by 3 strain gauges and the output by an other one. For these tests, a special specimen with the associated clamping system was developed for this kinds of materials (Figs. 4.12(a) and 4.12(b)). The specimen has a length gauge shorter than the normative tensile specimen to obtain higher strain rate. To increase the output signal, the specimen is larger than the classic tensile specimen.

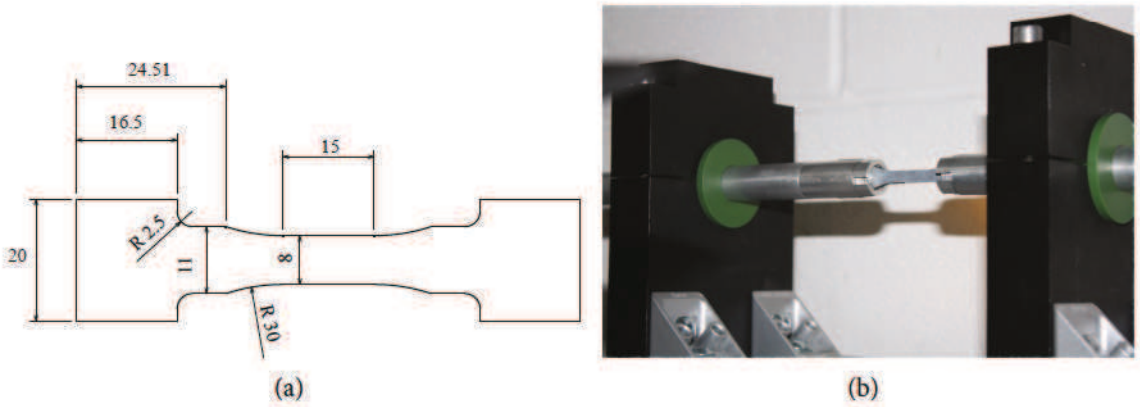

Figure 4.12: *Direct hopkinson bars testing technique: Hopkinson tensile specimen geometry (a) and Hopkinson tensile specimen in the clamping system (b).*

For these tests, two input pressures are used 9 and 17 bars, which correspond in term of velocities of the striker of 6.7 and 11.5 $m.s^{-1}$. These velocities allow to obtain two approximate strain rates during the tests of 350 and 600 s^{-1}. As in classic tensile test, the displacements are measured by 2D Digital Image Correlation. The signals given by the strain gauges are used with the DAVID®software to obtain the resultant forces of the tests. Fig. 4.13 shows the Hopkinson tensile test results in term of engineering stress-strain. For the two different tests, no viscous effect is observed for this range of strain rates on the yield stress and on the hardening of the material, as well. In comparison with the other tests carried out in tensile loadings (quasi-static and dynamic), the two responses obtained by the Hopkinson

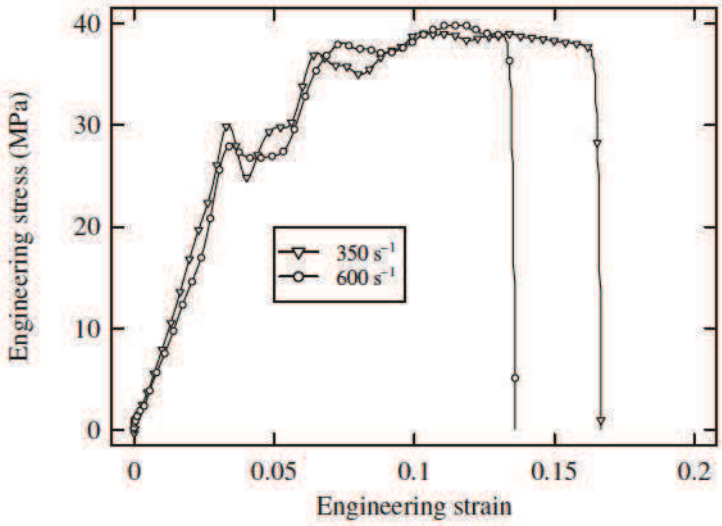

Figure 4.13: *Hopkinson tensile test responses for the two input pressures.*

tensile tests are relatively close. A saturation of the strain rate effect may occurs for hight strain rates.

4.2.4 Compression tests

The shape of the compression specimens are cylindrical (diameter 5 mm) and they have been cut using the water-jet technique in the thickness of the plates (3.2 mm). The uniaxial compression tests are carried out at 5 speed loadings. The tests at 1 mm.min^{-1} are performed on the electromagnetic device (INSTRON E3000) with a 3 kN cell force, two other speed loadings (1 and 150 mm.s^{-1}) are carried out on the hydraulic high speed device (INSTRON 65/20) with a 5 kN cell force. The corresponding equivalent strain rates of these tests are 5.2 10^{-3}, 0.3 and 46 s^{-1}. The non-contact measurement technique is used to obtain the displacement fields. An optical extensometer (Rudolph 200XR) with 250 kHz bandwidth is used for the displacement field measurements. This device determines in real time the current displacement by following two black/white transition markers made on the clamping system exposed to a homogenous lighting (Figs. 4.14(a) and 4.14(b)). The two last speed loadings are carried out on viscoelastic Hopkinson bars where the striker, input and output are made in polyamide (PA66). Two input pressures are used to obtain two different strain rates : 1900, 3800 s^{-1}. The same geometry (cylinder diameter 5 mm) is used to perform these tests. The non-contact measurement technique with the optical extensometer is used for displacement field measurements. Fig. 4.15 shows the compression test responses in term of engineering stress-strain curves for all the strain rates. As in

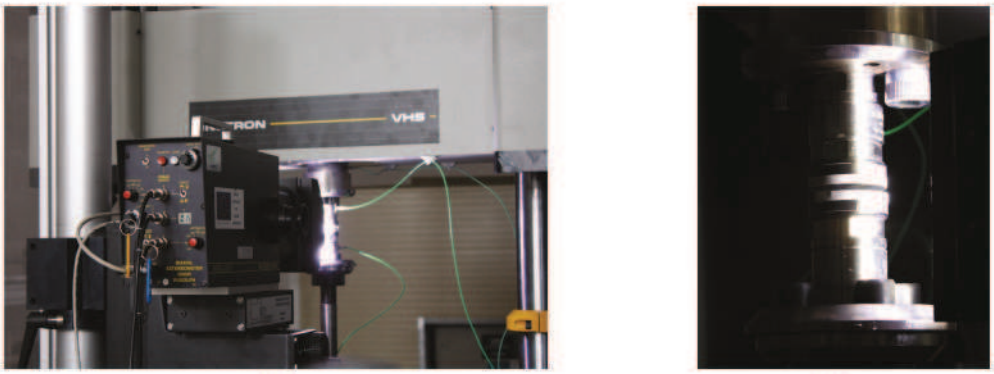

(a) (b)

Figure 4.14: *Displacement measurements in compression: optical extensometry for displacement field measurements (a) and clamping system with black/white transition markers (b).*

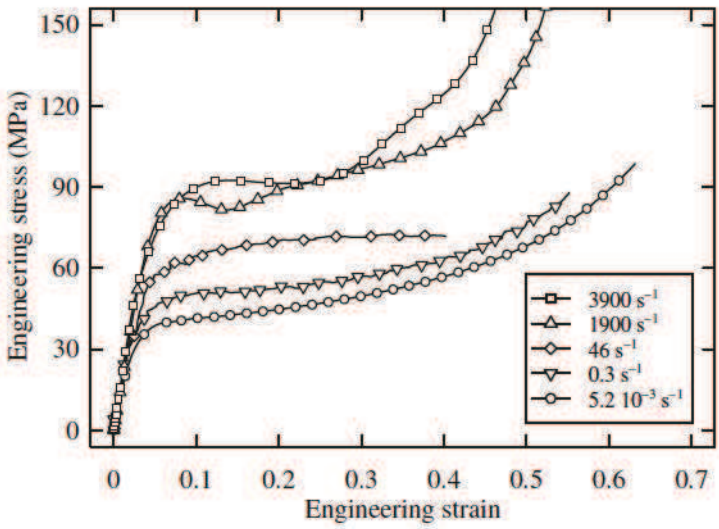

Figure 4.15: *Strain rate sensitivity on uniaxial compression loading.*

tensile loading, the stress response increases non-linearly as the strain rate increases.

4.3 Identification of the viscoelastic parameters

In a viscoelastic material, the relation between the stress and strain is described by a constitutive equation in a hereditary integral form (Section 3.1), such as

$$\sigma(t) = \int_{-\infty}^{t} E(t-\zeta)\frac{d\varepsilon(\zeta)}{d\zeta}d\zeta \tag{4.11}$$

where $E(t)$ is the linear relaxation modulus. In the constitutive model, the time dependent modulus $E(t)$ is modeled by the linear viscoelastic Wiechert model (Section 3.1). In this model, a finite number of separate Maxwell-elements are arranged in parallel with an elastic Hooke-element. In uniaxial tension loading, the relaxation modulus is given by

$$E(t) = E_\infty + \sum_{i=1}^{N} E_i \exp\left(-\frac{t}{\tau_i}\right) \tag{4.12}$$

where each spring i corresponds to a rigidity E_i and each newton element to a viscosity μ_i. The relaxation times τ_i are therefore defined as $\frac{\mu_i}{E_i}$. E_∞ represents the long term modulus of the material. In order to obtain a relationship between the time dependent modulus $E(t)$ and the complex modulus $E^*(i\omega)$, the input sinusoidal deformation (Eq. (4.1)) is substituted into the hereditary integral (Eq. (4.11)), as follow

$$\sigma(t) = i\omega\varepsilon_0 \int_{-\infty}^{t} E(t-\zeta)\exp(i\omega\zeta)\mathrm{d}\zeta. \tag{4.13}$$

Changing variables such as, $u = t - \zeta$ and noting that if $\zeta = -\infty$, $u = \infty$ and if $\zeta = t$, $u = 0$ yields to

$$\sigma(t) = \varepsilon_0 \exp(i\omega t) i\omega \int_0^{\infty} E(u)\exp(-i\omega u)\mathrm{d}u. \tag{4.14}$$

Noting that $\sigma(t) = \varepsilon_0 E^*(i\omega)\exp(i\omega t)$ and replacing the variable u by t, the complex modulus can be extracted such as

$$E^*(i\omega) = i\omega \int_0^{\infty} E(t)\exp(-i\omega t)\mathrm{d}t. \tag{4.15}$$

Using the time dependent modulus of the material, $E(t)$, expressed in a Prony series representation (Eq. (4.12)), the algebraic form of the function leads to explicit expressions for the storage and loss moduli, as follow

$$E^* = E' + iE'' = E_\infty + \sum_{i=1}^{N} E_i \frac{(\omega\tau_i)^2}{1+(\omega\tau_i)^2} + i\sum_{i=1}^{N} E_i \frac{\omega\tau_i}{1+(\omega\tau_i)^2}. \tag{4.16}$$

The storage and loss modulus are therefore expressed as

$$E'(\omega) = E_\infty + \sum_{i=1}^{N} E_i \frac{(\omega\tau_i)^2}{1+(\omega\tau_i)^2}, \tag{4.17}$$

$$E''(\omega) = \sum_{i=1}^{N} E_i \frac{\omega\tau_i}{1+(\omega\tau_i)^2}. \tag{4.18}$$

The parameters of a discrete relaxation spectrum are found by determining Eqs. (4.17) and (4.18) with the measured values of E' and E''. The coefficients E_i and the relaxation times τ_i are determined such that the average square deviation between the predicted and measured moduli (i.e. E' and E'') is minimum, such as

$$\min_{E_i,\tau_i} \sum_{i=1}^{M} \left[\left(\frac{E'(\omega_j)}{E'_M(\omega_j)} - 1 \right)^2 + \left(\frac{E''(\omega_j)}{E''_M(\omega_j)} - 1 \right)^2 \right] \tag{4.19}$$

where E'_M and E''_M are measured data at M frequency ω_j, E' and E'' are calculated from Eqs. (4.17) and (4.18). The result of the viscoelastic parameter identification with a model composed of 7 Maxwell-elements is listed in Table 4.2. The comparison between the viscoelastic model responses and the experimental data are shown in Figs. 4.16-4.18.

Table 4.2: *Linear viscoelastic parameters.*

Mode	$E_i(MPa)$	τ_i
i=1	495.7825	$1e^{+3}$
i=2	267.5181	$1e^{+2}$
i=3	249.6803	$1e^{+1}$
i=4	195.6641	1
i=5	151.5905	$1e^{-1}$
i=6	94.0675	$1e^{-2}$
i=7	59.1297	$1e^{-3}$
$E_\infty(MPa)$	486.932	

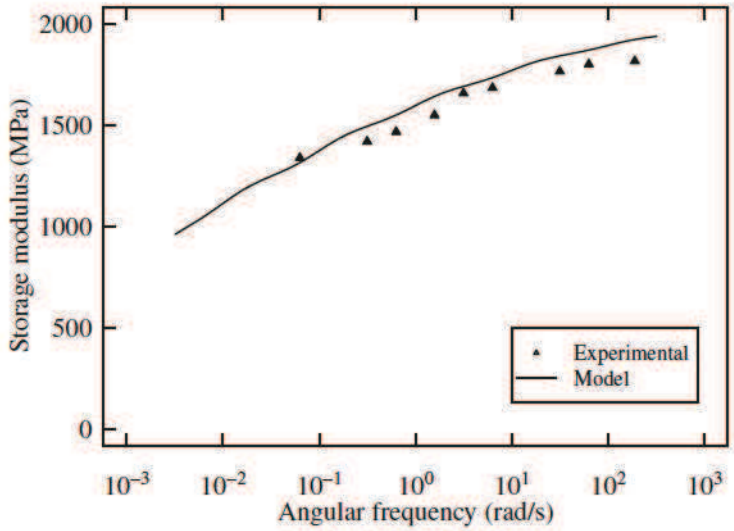

Figure 4.16: *Measured storage modulus and the Prony series fit.*

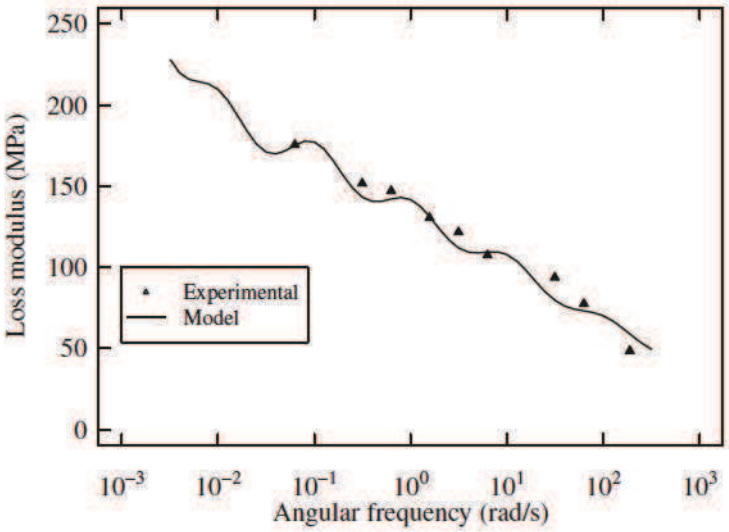

Figure 4.17: *Measured loss modulus and the Prony series fit.*

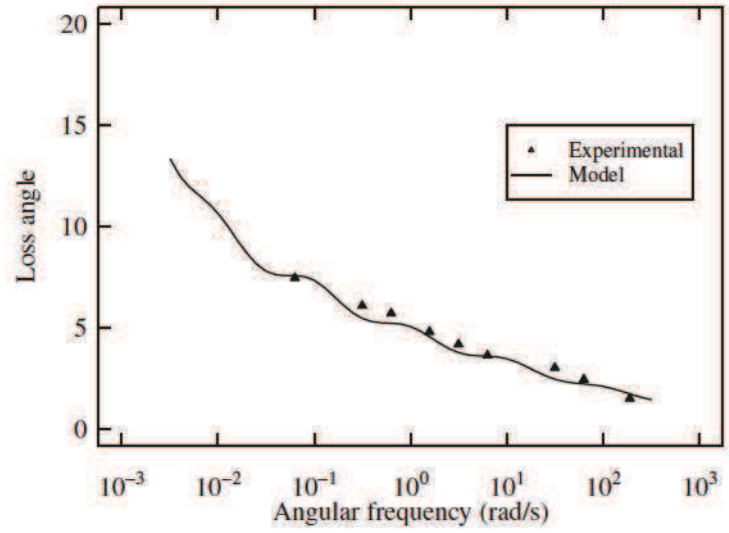

Figure 4.18: *Measured loss angle and the Prony series fit.*

4.4 Behaviour characterisation by the SEĖ method

The definition of the viscoplastic strain rate tensor used in the constitutive model (Eq. (3.158)) leads to a multiplicative form of the viscous behaviour law. Uniaxial tensile tests at constant strain rate are required for the identification of the behaviour law parameters. Unfortunately, the uniaxial tensile tests are not carried out at a constant strain rate. A video-controlled testing system developed by G'Sell and Jonas (1979) can be used for a uniaxial tensile test at a constant strain rate. Unfortunately, this experimental procedure

is not able to control the strain rate during the test in dynamic loading. The SEÈ method was developed to calculate the true behaviour laws in uniaxial tensile loading at a constant strain rate for a large strain rate range (i.e. quasi-static and dynamic). This technique, previously developed in the LAMIH laboratory, uses the heterogeneity of the strain fields during a tensile test to establish a viscoplastic behaviour law. In this method, the Digital Image Correlation measurement is used to calculate the true stress-strain laws of the material, by combining them with the true strain rates of each speed loading (not constant), it results a true behaviour surface. By cutting this behaviour surface at the desired strain rate, the behaviour laws at constant strain rate are also obtained (Lauro *et al.*, 2010; Epee *et al.*, 2011).

4.4.1 Compressibility versus incompressibility hypothesis

The true stress (Cauchy), which takes the reduction of the cross-sectional area into account, is given by[†] (G'Sell *et al.*, 2002)

$$\sigma_{yy} = \frac{F}{S_0} \exp(-e_{xx}) \exp(-e_{zz}) \tag{4.20}$$

where S_0 is the initial cross-sectional area. By assuming the isotropic transverse behaviour, as shown in Fig. 4.10, the true stress, given by Eq. 4.20 becomes

$$\sigma_{yy}^{\text{com}} = \frac{F}{S_0} \exp(-2e_{xx}). \tag{4.21}$$

On the other hand, the true stress calculated for an incompressible material (i.e. $\text{tr}(\underset{\sim}{\mathbf{e}}) = 0$) is given by

$$\sigma_{yy}^{\text{inc}} = \frac{F}{S_0} \exp(e_{yy}). \tag{4.22}$$

With the SEÈ method, the true stress is not calculated with the raw force given by the cell force of the testing device. Due to the heterogeneity of the deformation along the length of the specimen, the strain and strain rate are not constant in all the specimen. The displacement field measurements by DIC are done in all the Region Of Interest (ROI), which is the length gauge of the tensile specimen, on each Zone Of Interest (ZOI) included in the ROI (Fig. 4.19(a)). It results various strains and strain rates measured in each ZOI. The cross section is therefore divided in n ZOI and the total resultant force is the sum of the forces of each ZOI, as follow

$$F = \sum_{i}^{n} F_i. \tag{4.23}$$

[†] For the following relations, the loading direction is $\bar{y}$.

In the Digital Image Correlation technique, all the ZOI have the same size. Since the section is equivalently divided into n areas, the resultant force of each ZOI is given by

$$F_i = \frac{F}{n}. \tag{4.24}$$

The true stress for each ZOI is therefore calculated by following Eq. (4.21) for the compressibility hypothesis or Eq. (4.22) for the incompressibility hypothesis.

$$\sigma_{yy_i}^{com} = \frac{F_i}{S_{0_i}} \exp(-2e_{xx_i}), \tag{4.25}$$

$$\sigma_{yy_i}^{inc} = \frac{F_i}{S_{0_i}} \exp(e_{yy_i}) \tag{4.26}$$

where S_{0_i}, e_{xx_i} and e_{yy_i} are respectively, the initial cross section, transversal and axial Henky strain components of each ZOI. These different hypothesis have a strong impact on the behaviour laws deduced from the experimental tests. Fig. 4.19(b) shows the true behaviour laws (compressible and incompressible) calculated with the SEÈ method for the uniaxial tensile test at 1 mm.min^{-1} in function of the true equivalent strain.

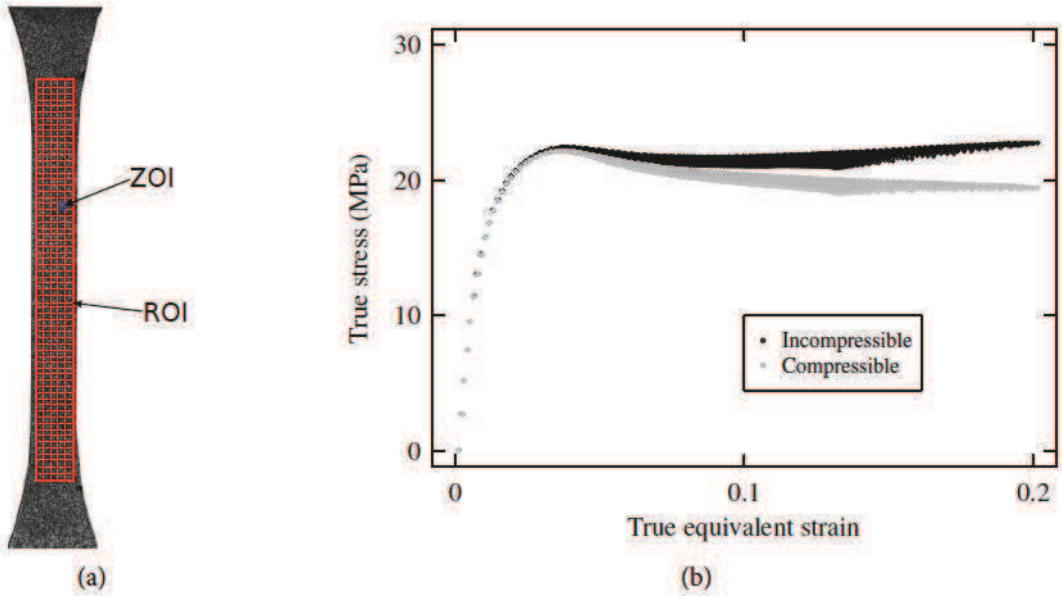

Figure 4.19: *Determination of the true behaviour laws by the SEÈ method: definition of ZOI and ROI for the strain field measurements by DIC (a) and true behaviour laws obtained with the SEÈ method at 1 mm.min^{-1}(b).*

The obvious hypothesis influence is illustrated in Fig. 4.19(b). A decrease of the stresses

at increasing strains (i.e. strain-softening) is obtained after the "hook" with the compressible assumption. On the other hand, the incompressible hypothesis produce an increase stresses at increasing strains (i.e. strain-hardening) on the behaviour laws.
In the proposed model, the behaviour law is function of the equivalent viscoplastic strain κ, the identification of its parameters is therefore performed with the equivalent true strain measurement. In the constitutive model, the yield stress is voluntary chosen when the true stress-strain curves begin to be nonlinear (6MPa) leading to a true equivalent viscoplastic threshold of 0.32 %. Consequently, the identification procedure is fulfilled with the total equivalent strain which is very close to the equivalent viscoplastic strain. Figs. 4.20 and 4.21 shows the true behaviour laws (not at constant strain rates) obtained with the SEÈ method for all the speed loadings. The compressible and incompressible laws, represented respectively in grey and black are plotted in the true strain-strain rate-stress space (e-ė-σ) in Fig. 4.20 and in the e-log10(ė)-σ space in Fig. 4.21. For each test some behaviour laws are also obtained. With the SEÈ method the true law with their corresponding true strain rates are therefore calculated by taking the heterogeneity of the deformation into account.

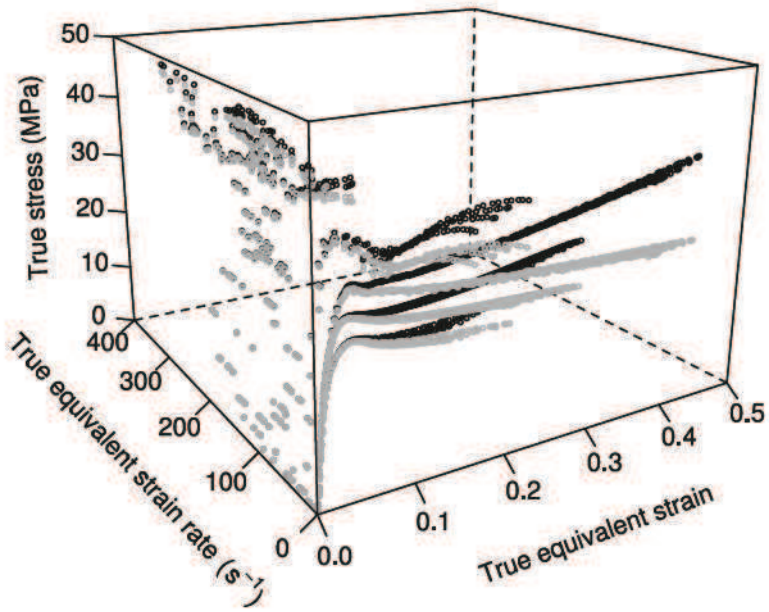

Figure 4.20: *True behaviour laws obtained with the SEÈ method: difference between compressible (grey) and incompressible (black) true behaviour laws in the e-ė-σ space.*

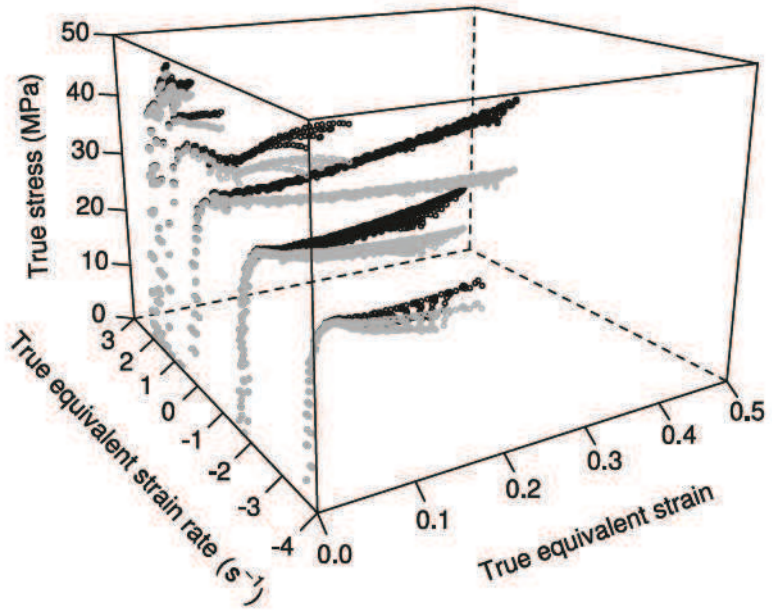

Figure 4.21: *True behaviour laws obtained with the SEÉ method: difference between compressible (grey) and incompressible (black) true behaviour laws in the e-*$\log 10(\dot{e})$*-*σ *space.*

4.4.2 Identification of the behaviour parameters

In the constitutive model, the behaviour law used (i.e. $\sigma_y = \sigma_t + R(\kappa)$) arise from the true stresses calculated with the incompressibility assumption which is corrected by the damage model[‡]. The multiplicative form of the viscous behaviour law σ_y^v coming from the viscoplastic formulation used in the constitutive model (Eq. (3.158)) can be expressed as

$$\sigma_y^v = (\sigma_t + R(\kappa))\left(\frac{\dot{\kappa}}{\dot{\kappa}_0}\right)^n \tag{4.27}$$

where the hardening variable $R(\kappa)$ is defined by

$$R = \rho\frac{\partial\Psi}{\partial\kappa} = Q_1\kappa\exp(-b_1\kappa) + Q_2(1-\exp(-b_2\kappa)) + b_3\kappa^3 + b_4\kappa^2 + b_5\kappa. \tag{4.28}$$

The form of the rate-dependent behaviour law (Eq. (4.27)) is close to the multiplicative law proposed by the G'Sell-Jaunas model (G'Sell and Jonas, 1979; G'sell *et al.*, 1983). The main difference is in the introduction of the parameter σ_t which corresponds to the initial yield stress in quasi-static. The effect of this modification is to represent only the viscoplastic part of the behaviour. The introduction of the term κ_0 is another modification which allows one to use the elastoviscoplastic model with a wide range of strain rates (i.e. quasi-

[‡]The identification of the damage model is detailed in Section 4.5

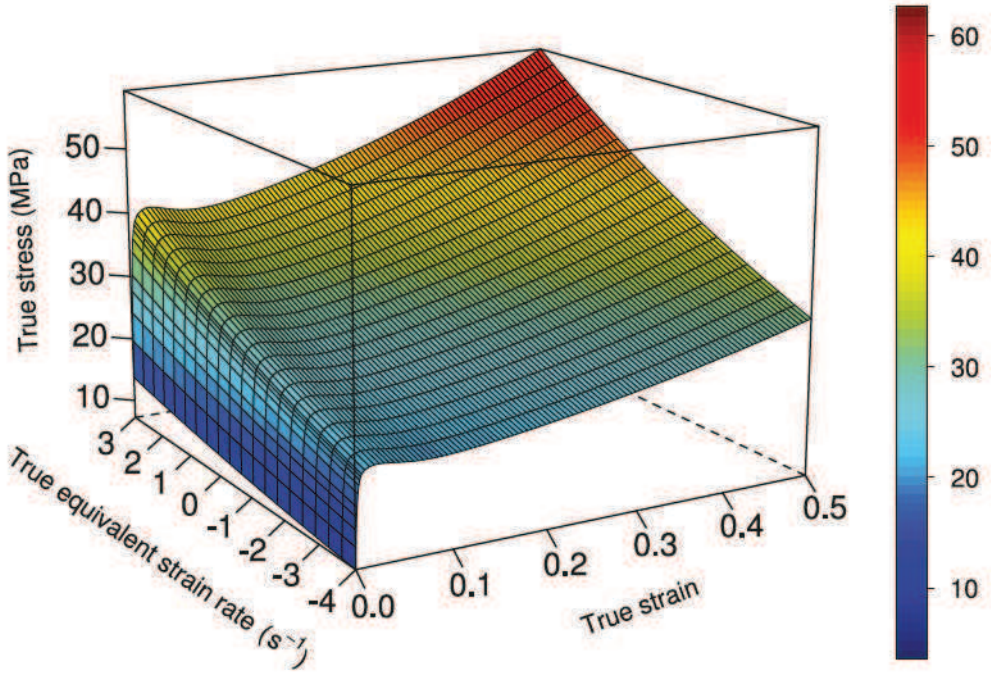

Figure 4.22: *True behaviour surface obtained by the SEĖ method is the e-ė-σ space.*

static and dynamic). This mathematical model can describe the "hook" (i.e. hardening softening cold-drawing) which is typical of the polypropylene behaviour. The parameters of the three-dimensional function are deduced by surface fitting using a least squares algorithm. Fig. 4.22 shows the true behaviour surface deduced by the SEĖ method in the e-log10(ė)-σ space. The behaviour parameters used in the yield surface f^{vp}, hardening variable $R(\kappa)$ and in the viscoplastic model (Eqs. (3.127), (4.28) and (3.158)) are given in Table 4.3. The behaviour laws at constant strain rate are therefore extracted by a numerical

Table 4.3: *Behaviour parameters used in the constitutive model.*

Parameter	Equation	Value
σ_y	(3.127)	6 (MPa)
Q_1	(4.28)	200 (MPa)
Q_2	(4.28)	10 (MPa)
b_1	(4.28)	50
b_2	(4.28)	570
b_3	(4.28)	0 (MPa)
b_4	(4.28)	20 (MPa)
b_5	(4.28)	9.5 (MPa)
b_5	(4.28)	9.5 (MPa)
$\dot{\kappa}_0$	(3.158)	$1\,10^{-6}$ (s^{-1})
n	(3.158)	0.04

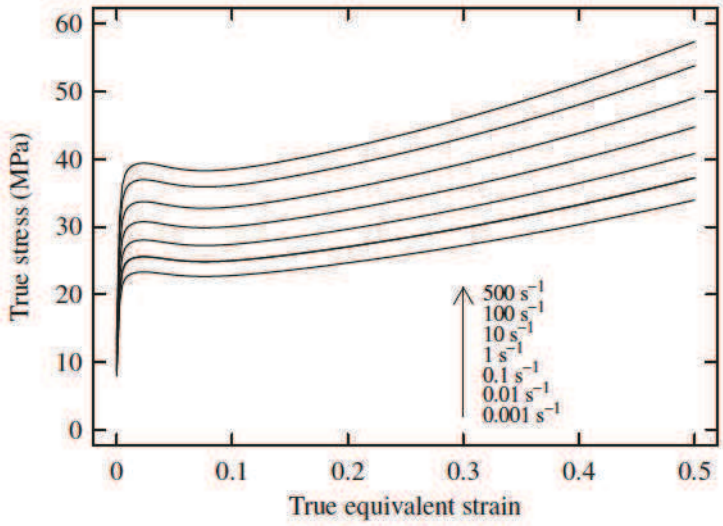

Figure 4.23: *True behaviour laws at constant strain rates obtained by the SEĖ method.*

cut of this 3D behaviour surface. Fig. 4.23 shows the true behaviour laws at constant strain rates obtained by the SEĖ method.

4.4.3 Identification of the flow parameters

As shown in Fig. 4.11, the trace of the strain tensor during the deformation is not null. This common behaviour of polymeric materials means that the viscoplastic deformation does not take place at constant volume. The non-associated viscoplasticity is used to take this non-isochoric deformation into account. As defined in Section 3.3.3, the non-associated viscoplastic flow (Eq. (3.134)) proposed in the constitutive model depends on the parameters α^+ and α^-. By influencing the viscoplastic flow, these parameters define the dilatation and the compaction present in tension and compression, respectively. The dilatation can be characterised by the plastic Poisson ratio ν_p which is a ratio between the transversal (e_{xx}) and axial (e_{yy}) strain components, such as

$$\nu_p{}^{\S} = -\frac{e_{xx}}{e_{yy}} = -\frac{e_{zz}}{e_{yy}}. \tag{4.29}$$

During a unique tensile test, one longitudinal and traversal strain is calculated by ZOI. The plastic Poisson ratio is therefore calculated for all the ZOI and all the speed loadings (i.e. quasi-static and dynamic). Fig. 4.24 shows the evolution of the plastic Poisson ratios

[§]Due to the presence of the transversal isotropy, the plastic Poisson ratio can be calculated with the thickness strain e_{zz} as well.

in function of the true axial strains for all the speed loadings and for all the ZOI. Due to the scattered responses for the very low strain values, only the plastic Poisson ratio values which corresponds to a true axial strain higher than 0.015 are plotted on this figure. No strain rate influence is observed on the plastic Poisson ratio evolution. A very fast decrease of the plastic Poisson ratio is observed until the value of 0.1.

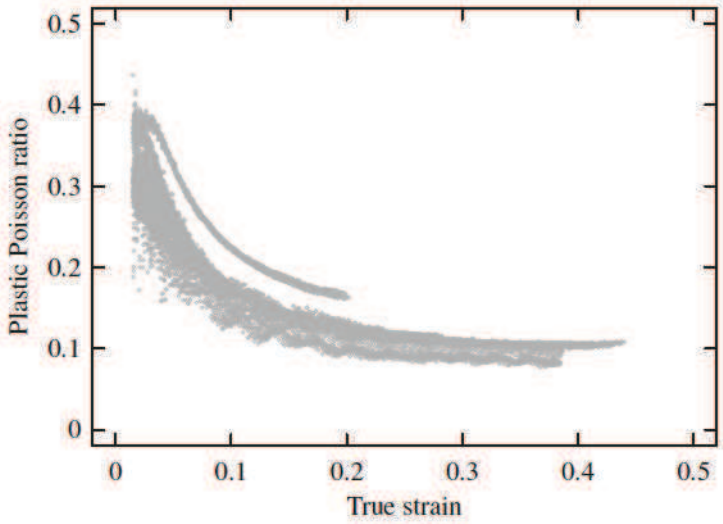

Figure 4.24: *Evolution of the plastic Poisson ratio versus true axial strain.*

During a uniaxial tensile test where $\vec{y}$ is the loading direction, the Cauchy stress and the logarithmic strain tensor are defined by

$$\underset{\sim}{\sigma} = \begin{Bmatrix} 0 & 0 & 0 \\ 0 & \sigma_{yy} & 0 \\ 0 & 0 & 0 \end{Bmatrix} \quad \text{and} \quad \underset{\sim}{\mathbf{e}} = \begin{Bmatrix} e_{xx} & 0 & 0 \\ 0 & e_{yy} & 0 \\ 0 & 0 & e_{zz} \end{Bmatrix}. \tag{4.30}$$

By considering that the viscoelastic part of the strain is very small in front of the viscoplastic part, the plastic Poisson ratio can therefore be calculated from the components of the viscoplastic tensor. According to the definition of the postulated viscoplastic potential F^{vp} given in Eq. (3.134), the incremental form of viscoplastic strain tensor of the constitutive model is given by

$$\Delta \underset{\sim}{\mathbf{e}}^{vp} = \Delta\lambda \frac{\partial F^{vp}}{\partial \underset{\sim}{\sigma}} = \frac{\Delta\lambda}{g(1-D)} \left(\frac{3}{2} \underset{\sim}{\mathbf{S}} + \frac{1}{3} \left(\alpha^{+} < p > -\alpha^{-} < -p > \right) \underset{\sim}{\mathbf{I}} \right). \tag{4.31}$$

Substituting Eq. (4.31) into Eq. (4.29) and noting that $\Delta\lambda$, g and D are constant, the plastic

Poisson ratio under tensile loading (i.e. $< -p >= 0$) is defined by

$$\nu_p = -\frac{\frac{3}{2}S_{xx} + \frac{1}{3}\alpha^+ p}{\frac{3}{2}S_{yy} + \frac{1}{3}\alpha^+ p}. \tag{4.32}$$

Recalling the definition of the deviatoric stress tensor $\underset{\sim}{\mathbf{S}}$, Eq. (4.32) becomes

$$\nu_p = -\frac{\frac{3}{2}(-p) + \frac{1}{3}\alpha^+ p}{\frac{3}{2}(\sigma_{yy} - p) + \frac{1}{3}\alpha^+ p} = -\frac{-\frac{3}{2}p + \frac{1}{3}\alpha^+ p}{3p + \frac{1}{3}\alpha^+ p} = -\frac{-\frac{3}{2} + \frac{1}{3}\alpha^+}{3 + \frac{1}{3}\alpha^+}. \tag{4.33}$$

After straightforward manipulations, the expression of the dilatation parameter α^+ is given by

$$\alpha^+ = \frac{9}{2}\left(\frac{1 - 2\nu_p}{1 + \nu_p}\right). \tag{4.34}$$

By setting the plastic Poisson ratio to 0.1, the value of the dilatation parameter α^+ is 3.272. A similar analysis can be fulfilled under uniaxial compression loading in order to define the compaction parameter α^-, unfortunately the small size of the specimen used for the uniaxial compression tests does not allow the use of the Digital Image Correlation. Furthermore, the optical extensometry measures only the axial displacement. The value of α^- is set to 0.5 according the numerical responses which is close to the incompressibility under uniaxial compression loading (i.e. $\alpha^- = 0$).

4.4.4 Hydrostatic pressure parameter identification

The engineering stress-strain curves obtained from uniaxial tensile and compression tests at respectively $5.5\,10^{-3}$ and $5.2\,10^{-3}$ s^{-1} are shown in Fig. 4.25. The obvious hydrostatic pressure dependency of the material is highlighted with this comparison. The stress response of the uniaxial compression test carried out at $5.2\,10^{-3}$ s^{-1} is much higher than the uniaxial tensile response at $5.5\,10^{-3}$ s^{-1} . The parameter η of the Raghava yield surface which takes the hydrostatic pressure dependence into account is deduced from the ratio between the compression and tension yield stresses (Eq. (3.127)). Due to the strain rate sensitivity of the material, the yield stresses in tension and compression need to be evaluate at the same strain rate. Unfortunately, the difference between the geometries of the tensile and compression specimens brings the previous condition infeasible. However, the two tests chosen (tension and compression) with their associated strain rates are relatively close. In the proposed model, the quasi-static yield stress in tension is voluntary chosen lower than the "hook" of the behaviour law. For better results, it is more convenient to work with the upper part of this "hook" instead of the yield stress. The calculus of the parameters η

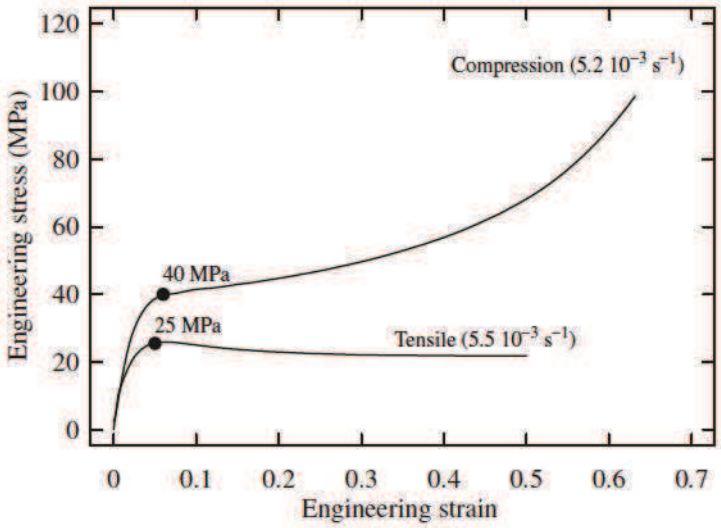

Figure 4.25: *Hydrostatic pressure influence on the response of the material.*

is done from stresses ratio, therefore only the engineering stresses are required. Fig. 4.25 shows the values of the upper part of the "hooks" given by the tensile and the compression tests. These results lead to a ratio between compression and tension of 1.6.

4.5 Damage characterisation

The damage of material is the degradation of its properties when the material is subjected to loading. Damage in Continuum Damage Mechanics is the nucleation and growth of micro-voids and micro-cracks in a medium considered as continuous at a larger scale. As the viscoplastic deformation, the damage is an irreversible process which evolves during the deformation. Furthermore, the deformation of mineral filled semi-crystalline polymers induces decohesion at charge-matrix interface. In this case, the viscoelastic-viscoplastic response of the material is accompanied by damage in the form of nucleation, growth and coalescence of cavities. Low and hight magnifications SEM micrograph of the fracture surface of mineral filled polypropylene under tensile loading at 1 mm.min^{-1} are shown in Figs. 4.26(a) and 4.26(b). A ductile fracture is observed with filament structure. The fibrillation observed is due to the cavitation phenomenon which occurs in the material. Nucleation of cavities around the mineral fillers is observed.

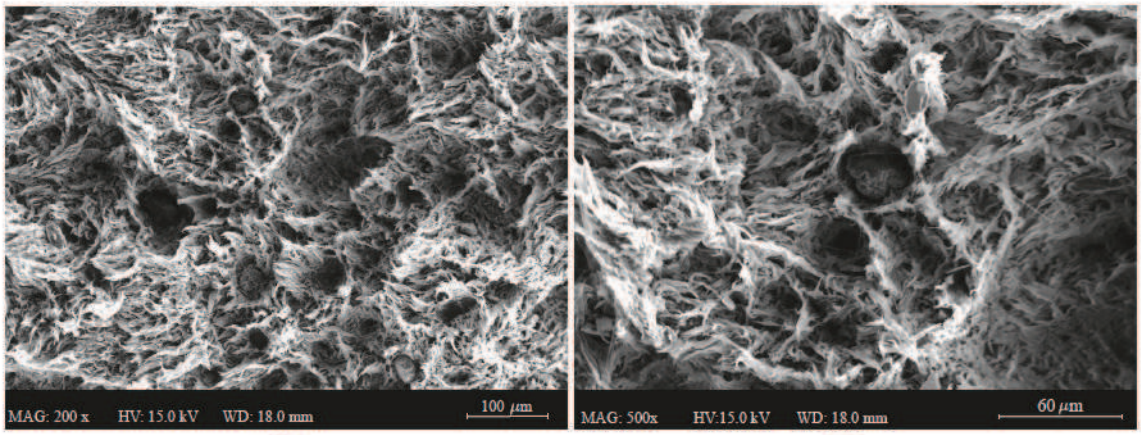

(a) (b)

Figure 4.26: *Low magnification SEM micrograph of the fracture surface of mineral filled polypropylene under tensile loading at 1 mm.min^{-1} (a) and hight magnification SEM micrograph of the fracture surface of mineral filled polypropylene under tensile loading at 1 mm.min^{-1} (b).*

4.5.1 Definition of the damage variable

In the CDM approach, the damage variable (D) is defined by the surface density of micro-voids and micro-cracks lying on a plane cutting the Representative Volume Element (RVE) of cross section S. The RVE, introduced in mechanics of continuous media, represents a volume where all properties are represented by homogenised variables. For the plane with normal $\vec{n}$, the damage variable is given by

$$D_{(\vec{n})} = \frac{S_D}{S} \tag{4.35}$$

where S_D is the area of the intersection of all micro-cracks and micro-voids which lie in S. For an isotropic damage, the damage variable $D_{\vec{n}}$ does not depend on the normal. This variable is therefore a scalar (Kachanov, 1958) such as

$$D = \frac{S_D}{S}. \tag{4.36}$$

In the CDM theory, the cross section of the VER (S) is replaced by a resisting area given by

$$\tilde{S} = S - S_D = S(1 - D). \tag{4.37}$$

The effective stress introduced in Eq. (3.126) arises from the above equation (Eq. (4.37)) such as

$$\tilde{\sigma} = \frac{F}{\tilde{S}} = \frac{F}{S(1-D)} = \frac{\sigma}{1-D}. \tag{4.38}$$

4.5.2 Characterisation of the damage variable with the SEĖ method

In this first procedure no additional tests are required. The damage variable is identified directly by the results given by the SEĖ method. The damage variable is deduced from the ratio between the compressible behaviour law σ_y^{com} and the incompressible behaviour law σ_y^{inc} as follow

$$D = 1 - \frac{\sigma_y^{com}}{\sigma_y^{inc}}. \tag{4.39}$$

As described previously (Section 4.4.1), one behaviour law per hypothesis (compressible and incompressible) is given for each ZOI of the specimen and for all speed loadings. It results an important number of damage evolutions. Fig. 4.27 shows the evolution of the damage variables from all the speed loadings and for all the ZOI. The first observation is the strain rate independence on the damage evolution. All the strain rates, between 5.5 10^{-4} and 600 s^{-1} have a very similar evolution. The strain value which corresponds with the start of damage called damage threshold is very low. The damage increases non linearly as function of the true equivalent strain.

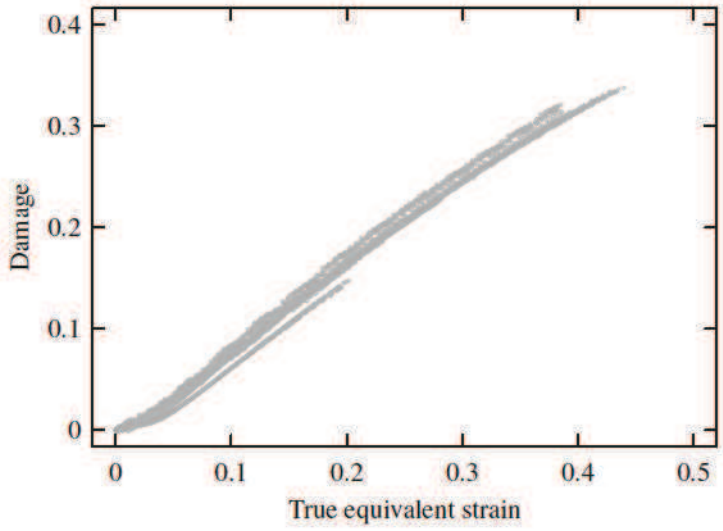

Figure 4.27: *Evolution of the damage variable for all the speed loadings.*

4.5.3 Characterisation of the damage variable by loss of stiffness

In uniaxial tensile loading, the elastic law coupled with damage (Eq. (4.38)) leads to the expression of the damage in function of the loss of stiffness given by

$$D = 1 - \frac{\tilde{E}}{E} \tag{4.40}$$

where $\tilde{E}$ is the Young modulus of the damaged material. A uniaxial tensile test with repeated unloadings is therefore used to evaluate the evolution of the damage parameter. For this kind of measurement, Lemaitre (1985a) recommends the following procedure:

- A specimen with weaken section in its middle in order to localise the deformation (damage).
- Due to localisation of the damage, the deformation measurement needs to be done by small strain gauges.
- The elasticity modulus is evaluated during the unloading between a lower and upper value of stress in order to eliminate the non linearities on the stress-strain curve.

The damage measurement of the polymeric material under investigation is fulfilled on a notched specimen in order to localise the deformation in the notch (Fig. 4.28). The displacements are measured by optical extensometer with a base of measurement of 2 mm (Fig. 4.29). This uniaxial tensile test with repeated unloadings is carried out in quasi-static, the electromagnetical device with a cell force of 3kN (INSTRON E3000) is therefore used. The specimen is loaded with a prescribed displacement at 1 mm.min^{-1} for its loads and unloads. Fig. 4.30 shows the imposed displacement in function of the time. Some preliminary tests were done to evaluate the unload path in order to avoid the compression loading during the unload phase of the test.

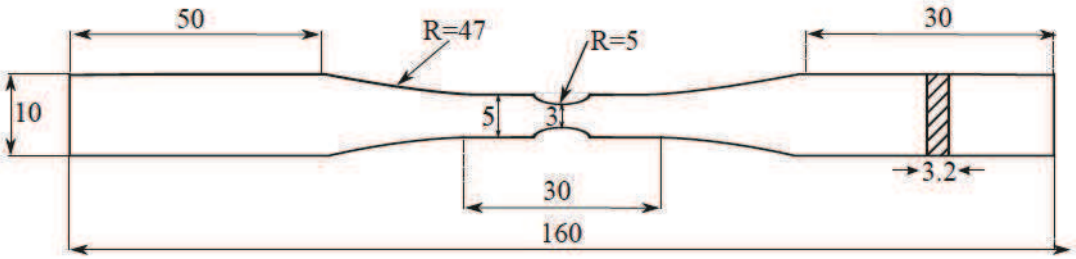

Figure 4.28: *Geometry of the notched specimen for the damage measurement.*

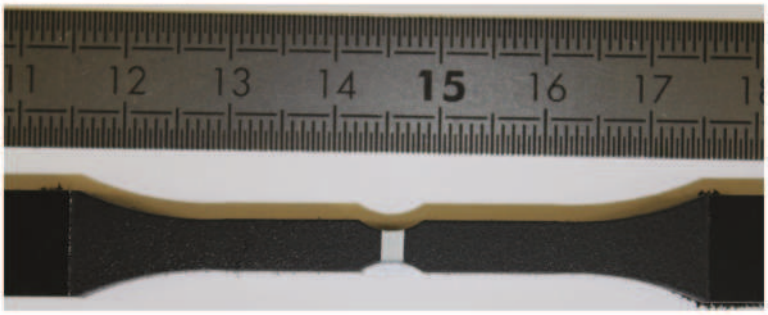

Figure 4.29: *Preparation of the notched specimen for displacement measurements by optical extensometry.*

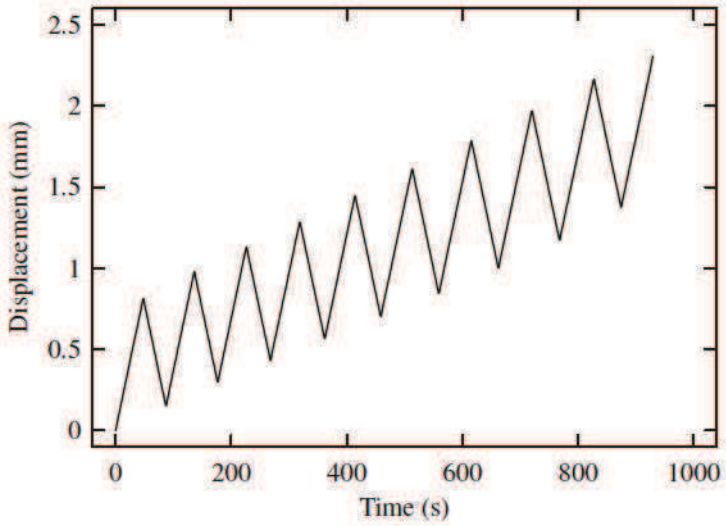

Figure 4.30: *Imposed displacement for the uniaxial tensile test with repeated unloadings.*

The response of the material in term of engineering stress-strain is presented in Fig. 4.31. The expected viscoelastic behaviour with its characteristic hysteresis is well captured. Due to the viscoelasticity of the material being studied the load and unload phase are not linear. The stiffness is therefore taken between the upper and lower point of the hysteresis caused by the viscoelastic behaviour. The stiffness evaluated with this method is not similar to the Young modulus, it is more an indicator of the rigidity. However, for convenience, the term of modulus is employed in this section to designate this rigidity. The damaged modulus $\tilde{E}$ is evaluated for each hysteresis and the non damaged modulus E by the first loading path.

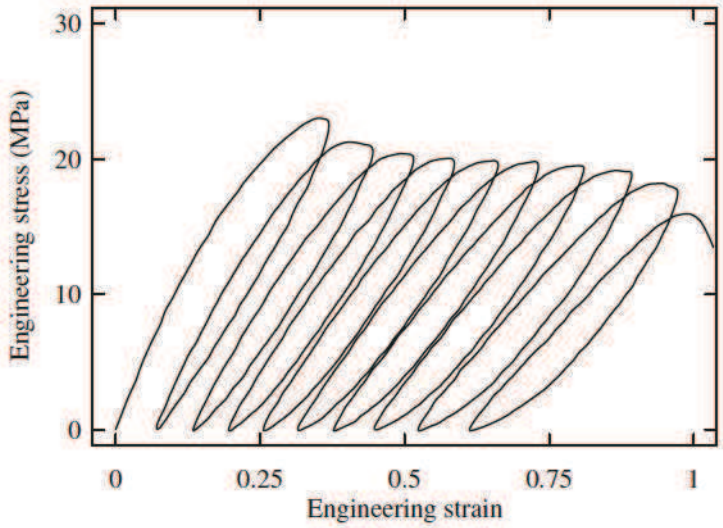

Figure 4.31: *Engineering stress-strain response in uniaxial tensile test with repeated unloadings.*

The damage variable D is therefore calculated by Eq. (4.40) for each value of $\check{E}$. The complete procedure for the damage measurement by loss of stiffness is summarised in Fig. 4.32. The evolution of the damage parameter calculated by the loss of stiffness procedure in function of the true equivalent strain is presented in Fig. 4.33. In order to make the comparison with the previous results, the damage evolution characterised with the SEĖ method is plotted on the same figure. The two evaluation techniques have results very close. As shown with the characterisation fulfilled with the SEĖ method, the degradation of the material occurs at the start of the deformation.

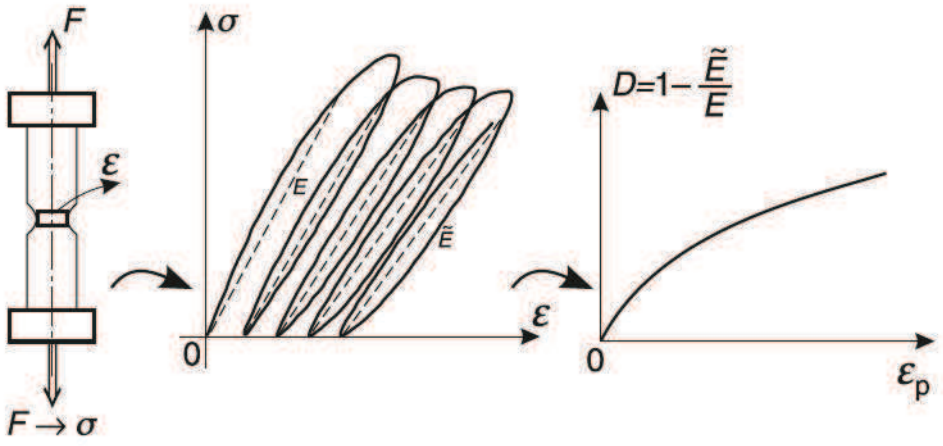

Figure 4.32: *Procedure for damage measurement by loss of stiffness.*

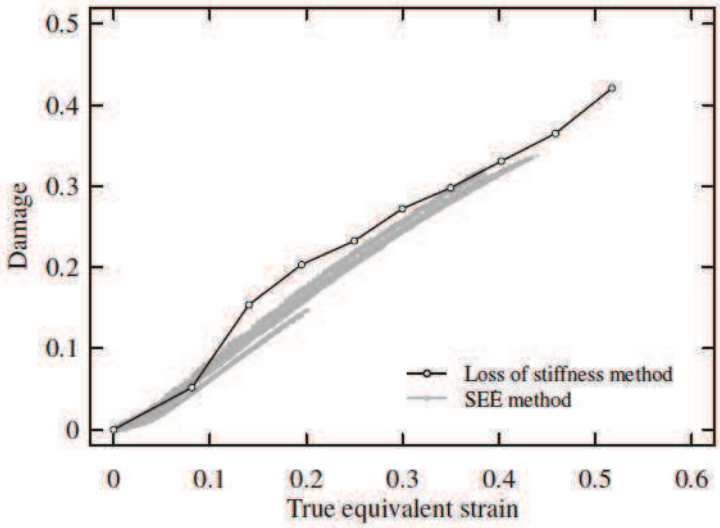

Figure 4.33: *Comparison of the damage evolution between the SEE̊ and loss of stiffness method.*

4.5.4 Identification of the damage model parameter

As shown in Fig. 4.27, the damage evolution does not depend of the strain rate. The proposed damage model is therefore only function of the equivalent viscoplastic strain. The damage model used to represent the experimental observations is given by (Eq. (3.147))

$$D = 1 - \exp\left(-\frac{\kappa}{k_c}\right). \tag{4.41}$$

The unique parameter k_c of the damage evolution law is deduced by fitting the experimental data with a least squares algorithm. The optimal value for k_c found is 0.95. Fig. 4.34 shows the comparison between the damage model and the experimental results.

4.5.5 Damage visualisation by tensile test in-situ X-ray microtomography

In order to visualise the evolution of the damage during the deformation, i.e. the nucleation and growth of voids and cracks, a tensile test is carried out in a microtomograph. A small tensile specimen with a geometry of 6.35x1.78x1 mm in the length gauge is used. µCT scanning was performed thanks to an 1172 SKYSCAN system, with 40 kV and 100 µA settings. The voxel size for all µCT data was adjusted to 3.97 µm. This choice was carried out in order to have enough accuracy in the porosity measurement regarding the scanning

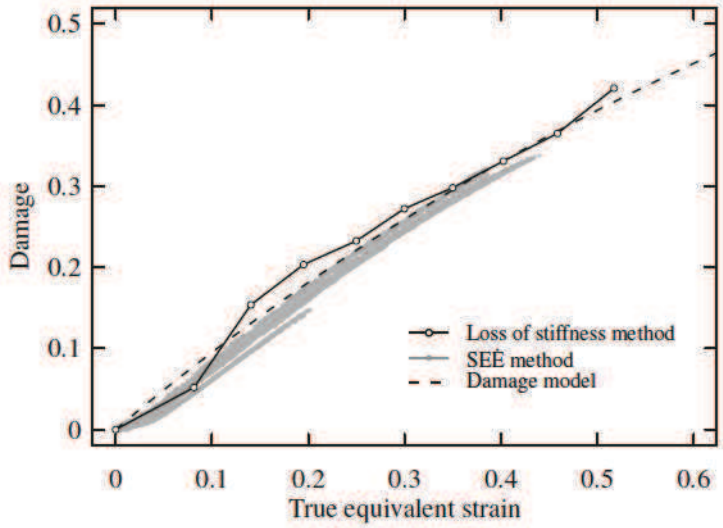

Figure 4.34: *Comparison of the damage evolution observed experimentally and the damage model.*

time. Under these conditions, the duration of acquisition is about 8 hours for a sample of 7 mm height. A first µCT-scan is carried out at the initial state (i.e. undamaged material) and two other µCT-scans are performed to follow the evolution of the real cross sections at different positions during the loading. In order to quantify the damage evolution during the deformation of the specimen, the real and effective cross-sections along the length gauge of the specimen are presented in Figs. 4.35 and 4.36 for the initial and two deformed states.

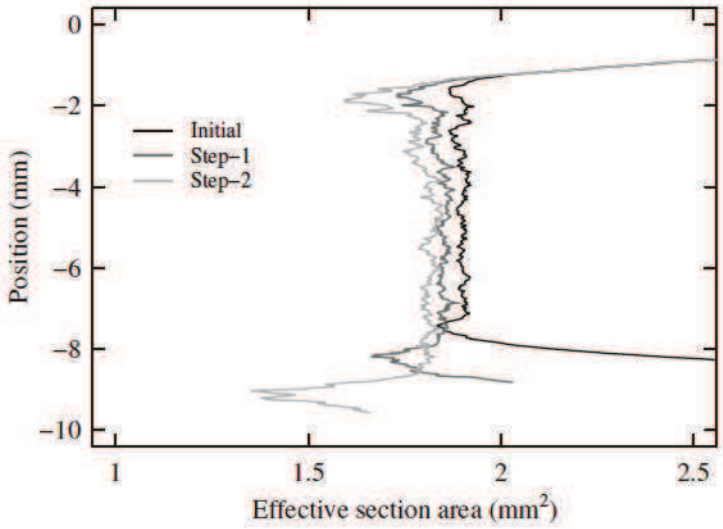

Figure 4.35: *Evolution of the effective cross section measured by µCT.*

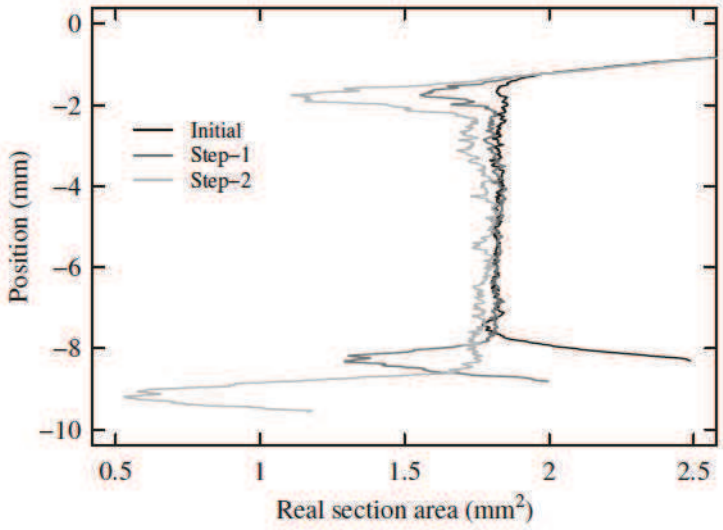

Figure 4.36: *Evolution of the real cross section measured by* µ*CT.*

These cross-sections are obtained by imaging treatment, for each step, a set of grey scale images is obtained along the principal direction of the sample. Each slice is then transformed to a binary image by applying a grey level threshold. This threshold is chosen to ensure a realistic description of both the porosity and the polymer matrix. In this test, the deformation occurs mainly at the extremities of the length gauges. At the bottom of the specimen, where the displacement is applied, the real and effective cross-sections decrease strongly. Another decrease of the two cross-sections is observed at the top of the specimen. Recalling the definition of the damage variable in Continuum Damage Mechanics, i.e. $D = 1 - \frac{\tilde{S}}{S}$, the damage variable evolution is calculated along the length gauge of the specimen. These results are presented in Fig. 4.37. No damage occurs in the centre of the specimen between the two localised deformation zones. A fast increase of the damage in the two zones where the deformations takes place until the critical value of 0.6 at the bottom of the specimen.

The tensile test in-situ X-ray microtomography is a well technical solution to visualise the evolution of the porosities during the deformation, unfortunately, the localisation of the deformations in two very small parts of the specimen makes hard the deformation measurement. The damage value calculated is therefore, in this case, not reliable with the deformation.

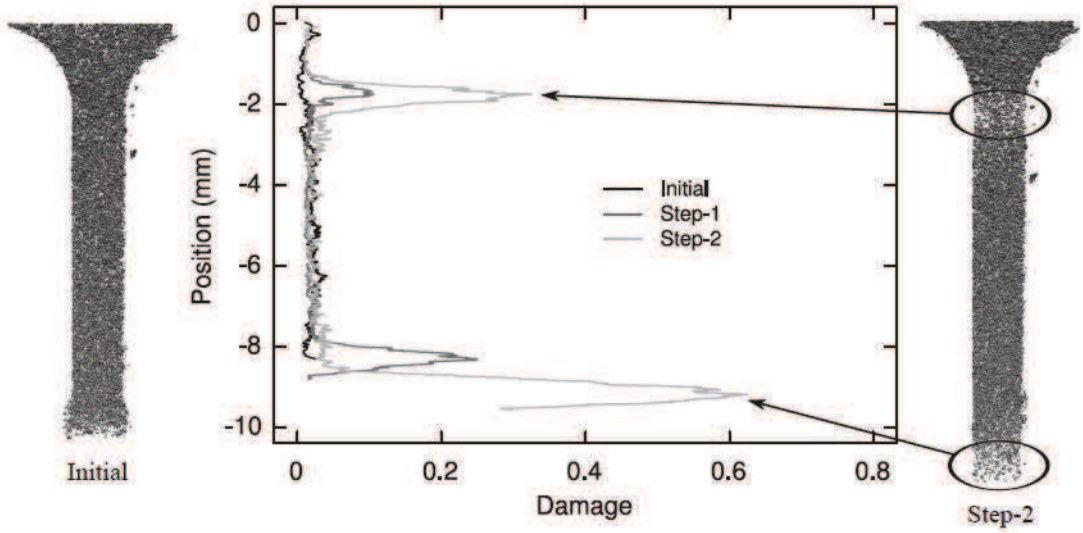

Figure 4.37: *Evolution of the damage measured by* µ*CT.*

4.6 Conclusions

The procedure for the material parameter identification from experimental tests have been presented in this chapter. The viscoleastic parameters are identified with Dynamic Mechanical Analysis. The uniaxial tensile tests conducted at several speed loadings are used for the identification of the behaviour, flow and damage parameters. The identification of the behaviour law is fulfilled with the SEĖ method which is able to produce the behaviour laws at constant strain rate on a large strain rate range. The compression tests give the ratio between the compression and tension "yield stresses" necessary for the pressure dependent yield surface. Several techniques have been presented in order to evaluate the evolution of the damage variable during the deformation. The classic measurement by loss of stiffness is compared with the evaluation resulting to the SEĖ method. The two characterisation procedures lead to the same damage evolution. All the material parameters involved in the constitutive model are listed in Table 4.4 The visualisation of the porosities by microtomography during an in-situ tensile test have been used to quantify the damage induced by the deformation. Unfortunately, this kind of specimen does not allow to link the damage variable with a deformation measurement. A uniaxial tensile test in-situ X-ray microtomography with a notched specimen can be a solution to have a better control of the deformation in order to obtain the evolution of the damage variable in function of the deformation.

Table 4.4: *Material parameters involved in the constitutive model.*

	Parameter	Equation	Value
Viscoelastic	E_∞	(4.12)	486.932 (MPa)
	E_1	(4.12)	495.7825 (MPa)
	E_2	(4.12)	267.5181 (MPa)
	E_3	(4.12)	249.6803 (MPa)
	E_4	(4.12)	195.6641 (MPa)
	E_5	(4.12)	151.5905 (MPa)
	E_6	(4.12)	94.0675 (MPa)
	E_7	(4.12)	59.1297 (MPa)
	τ_1	(4.12)	$1e^{+3}$ (s^{-1})
	τ_2	(4.12)	$1e^{+2}$ (s^{-1})
	τ_3	(4.12)	$1e^{+1}$ (s^{-1})
	τ_4	(4.12)	1 (s^{-1})
	τ_5	(4.12)	$1e^{-1}$ (s^{-1})
	τ_6	(4.12)	$1e^{-2}$ (s^{-1})
	τ_7	(4.12)	$1e^{-3}$ (s^{-1})
Behaviour	σ_y	(3.127)	6 (MPa)
	Q_1	(4.28)	200 (MPa)
	Q_2	(4.28)	10 (MPa)
	b_1	(4.28)	50
	b_2	(4.28)	570
	b_3	(4.28)	0 (MPa)
	b_4	(4.28)	20 (MPa)
	b_5	(4.28)	9.5 (MPa)
	b_5	(4.28)	9.5 (MPa)
	$\dot{\kappa_0}$	(3.158)	$1\,10^{-6}$ (s^{-1})
	n	(3.158)	0.04
Viscoplastic flow	α^+	(3.134)	3.272
	α^-	(3.134)	0.5
Pressure	η	(3.127)	1.6
Damage	k_c	(3.147)	0.95

Chapter 5

Validation of the constitutive model

In this chapter, the robustness and the accuracy of the developed viscoelastic-viscoplastic model coupled with damage is tested. Firstly, some comparisons between the implementation of the user material subroutine in the implicit and the explicit finite element codes are presented. In the same way, the numerical responses of the constitutive model used with shell and solid elements are confronted. The nonlocal regularisation in order to obtain mesh independent results is verified with some numerical simulations under different kinds of loadings and for various element types. An analysis of the intrinsic length influence is carried out on a notched tensile specimen. Finally, some comparisons between the numerical responses of the constitutive model and the experimental data are presented. In order to validate the constitutive model, uniaxial tension, with straight and notched specimens and compression tests at several speed loadings are simulated. The strain rate sensitivity and the pressure dependency are verified by these different simulations. The validation of the volume variation which is modelled by the non-associated viscoplastic model is pointed out.

5.1 Verification of the constitutive model implementation

In order to test the robustness and the accuracy of the constitutive model, some verifications are made in order to compare the numerical responses of the implemented model in the implicit and the explicit finite element codes, ABAQUS/Standard® and LS-DYNA®, respectively. Moreover, a comparison between the implementation with shell and eight-node hexahedral elements is presented at the same time. For the following and for all the

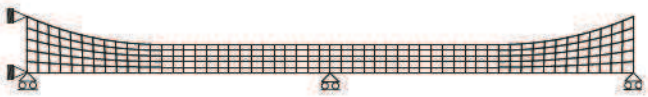

Figure 5.1: *Finite element mesh and boundary conditions of the tensile specimen.*

simulations carried out in this chapter, the material parameters used are given in Table 4.4* (Section. 4.6). Furthermore, a thickness of 3.2 mm is assumed in all the simulations carried out with shell elements. The numerical case under investigation is the tensile test with the geometry defined in Chapter. 4 (Fig. 4.5). The simulations of the tensile tests are carried out with reduced integrated eight-node hexaedral and reduced integrated shell elements where 3 integration points through the thickness are used. For symmetry reasons, only the half specimen is meshed with shell elements and the quarter with eight-node hexaedral elements with the appropriate boundary conditions. The finite element mesh with shell elements is represented in Fig. 5.1. The same finite element mesh is used for the three-dimensional model where two elements in the half of the thickness is assumed. The loading consists of a prescribed monotonic velocity of 1 $m.s^{-1}$ of the nodes on the right edge of the mesh up to a total axial elongation of 5 mm. The four simulations are carried out with the constitutive model where the local damage model is used (i.e. the intrinsic length is set to 0 mm)†. Fig. 5.2 shows the reaction forces at the left of the specimens versus the

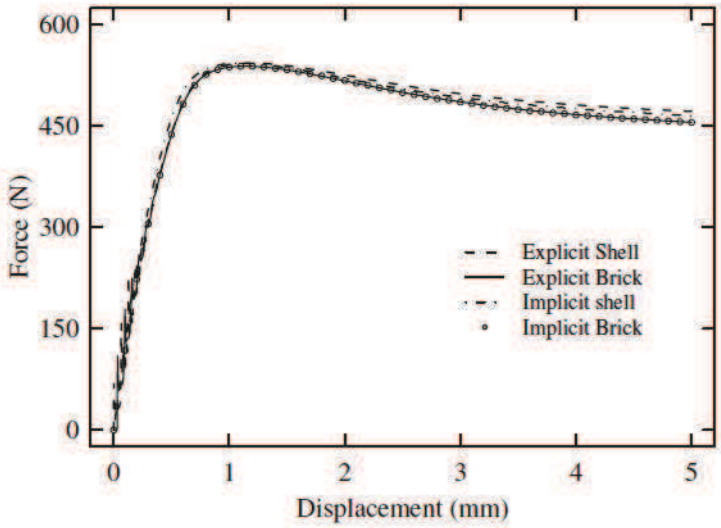

Figure 5.2: *Reaction force responses given by the constitutive model by implicit and explicit uniaxial tensile simulations with eight-node hexaedral and shell elements.*

*In some particular simulations of this chapter, one or more parameters explicitly detailed can differ than in Table 4.4.

†The analysis of the nonlocal damage model under uniaxial tensile loading is detailed in the next section.

Table 5.1: *Residual out of plane stress* (σ_{zz}) *in Pa.*

Iteration	step 1	step 2	step 3
1	4981.47	10647.565	8355.295
2	-0.494	-3.5831	-2.084
3	4.976e-05	1.217e-03	5.235e-04
4	-4.918e-09	-4.135e-07	-1.315e-07

displacements enforced at the right boundaries for all the simulations. The reaction forces predicted by the numerical model for the four simulations are very close. The simulations carried out with the implicit and the explicit finite element codes using eight-hexaedral elements have exactly the same responses. The numerical responses with shell elements exhibit a small difference with the three-dimensional analysis for the two finite element codes. By taking the three-dimensional result as the reference, the maximal deviation arising with the explicit finite element code is 3.5 % and 2.2 % is observed with the implicit finite element code. In order to illustrate the efficiency of the implementation with shell elements, Table 5.1 shows the number of iterations with the residual out of plane stress component values for three time steps which arise from one element situated in length gauge of the specimen during the implicit simulation with shell elements. The implemented procedure proves to be efficient, the out of plane stress value decreases quite quickly and a very low value at the fourth iteration is observed.

The previous results highlight the efficiency of the implementation of the constitutive model with shell elements. The simulations performed with the implicit and the explicit finite element codes with solid and shell elements give similar results. Consequently, all results presented in this chapter are performed with the implicit finite element code ABAQUS/Standard®using the developed constitutive model implemented in FORTRAN®77 in a user-material subroutine.

5.2 Validation of the mesh independence

5.2.1 Mesh dependency under uniaxial tensile loading

In order to evaluate the mesh dependency of the constitutive model under uniaxial tensile loading, numerical tests are performed on a square with a length of 40 mm loaded in uniaxial tension. Three different meshes are used for the numerical simulations: 25, 100 and 400 elements. For symmetry reasons, the analysis is carried out on the quarter of the geometry with appropriate boundary conditions. The geometry of the problem, boundary conditions and the finite element meshes adopted are given in Fig. 5.3. The loading

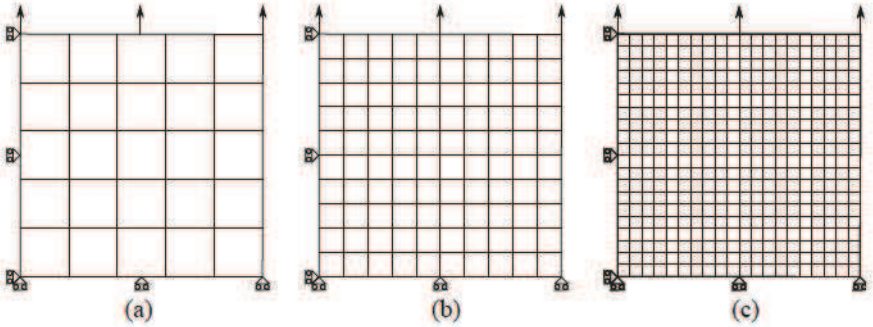

Figure 5.3: *Finite element meshes and boundary conditions for the uniaxial tensile simulations with three different meshes: 25 elements (a), 100 elements (b) and 400 elements (c).*

consists of a prescribed monotonic velocity (with free vertical displacement) on the nodes of the top edge of the meshes up to a total axial elongation of 10 mm (with a velocity of 1 mm.s^{-1}). The simulations are carried out with reduced integrated shell elements where 3 integration points through the thickness are used. The simulations are performed with the constitutive model described in chapter 3 where an internal length of 2mm is assumed in the nonlocal damage model. In a second time, the nonlocal regularisation is deactivated in order to evaluate the regularisation by the viscoplastic formulation. The reaction forces in the middle of the three meshes versus the displacements at the top boundaries are shown in 5.4. The six simulations have exactly the same responses, the reaction forces are exactly the same for the three different meshes and with or without the nonlocal damage averaging. The final deformed shapes of the square meshed with three different number

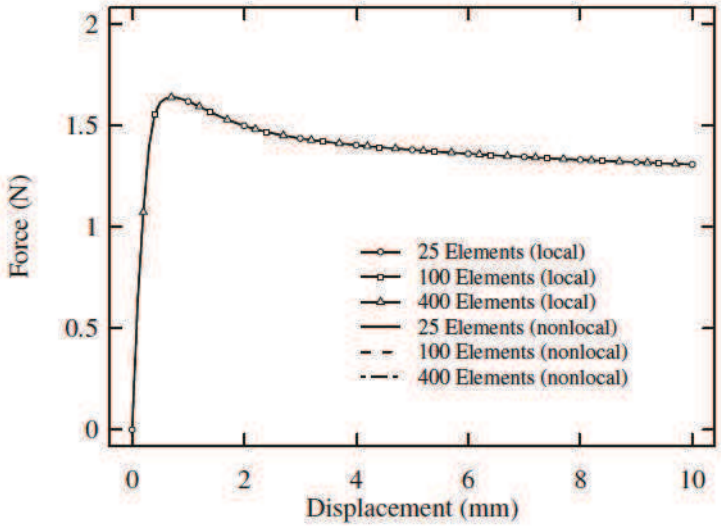

Figure 5.4: *Force response on the uniaxial tensile test for the 3 different meshes and with the two damage models (local and nonlocal).*

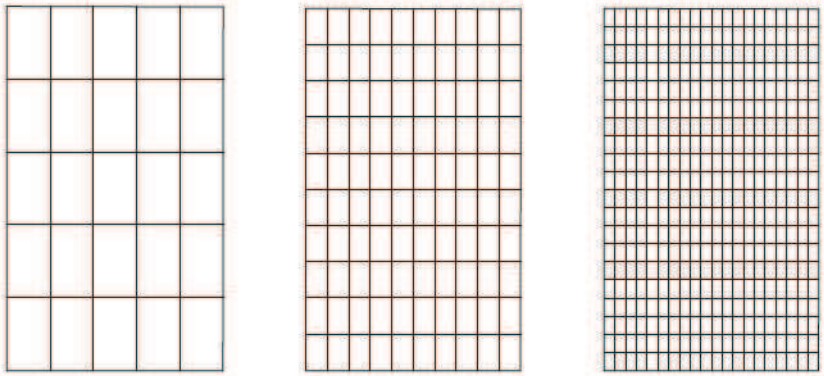

Figure 5.5: *Uniaxial tensile loading on square. Deformed shape for three different meshes: 25 elements (a), 100 elements (b) and 400 elements (c) simulated without the nonlocal regularisation.*

of elements with the local damage model[‡] are shown in Fig. 5.5. Under uniaxial tensile loading, the viscoplastic formulation of the constitutive model is enough to overcome the mesh dependency problem due to the softening behaviour of the material being studied. In this loading case, the nonlocal averaging does not provide better solution than the local damage model.

5.2.2 Rectangular bar localisation analysis under plane strain

The mesh independence of the constitutive model is verified on a simulation of the necking of a rectangular bar in tension. A rectangular bar under plane strain condition with a length of 53.334 mm and a width of 12.826 mm is subjected to uniaxial tensile loading up to a total axial elongation of 8 mm (with a velocity of 1 $mm.s^{-1}$). Due to obvious symmetry, only the quarter of the bar is modelled with the appropriate boundary conditions. For the simulations, three different meshes are used in order to evaluate the sensitivity of the mesh on the numerical response. Meshes of 200, 800 and 1800 four node quadrilateral elements under plane strain condition shown in Fig. 5.6 are used. Reduced numerical integration is adopted in order to avoid locking effects. The three meshes contain a geometric imperfection of 1.8 % at the bottom in order to trig the necking in the centre of the rectangular bar. Due to the low value of the plastic Poisson ratio identified in the investigated material under positive hydrostatic pressure, for this simulation, the material parameters α^+ is set to 0.5. With this modification, a value of 0.4 is therefore obtained for the plastic Poisson ratio under tensile loading. This modification is made to easily trig the necking.

[‡]The deformed shapes of the square with and without the nonlocal damage model are identical.

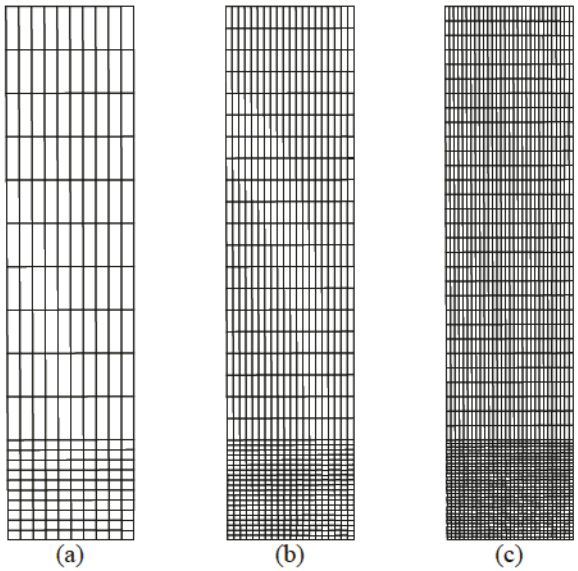

Figure 5.6: *Necking of a rectangular bar in plane strain. Finite element meshes of 200 (a), 800 (b) and 1800 (c) elements.*

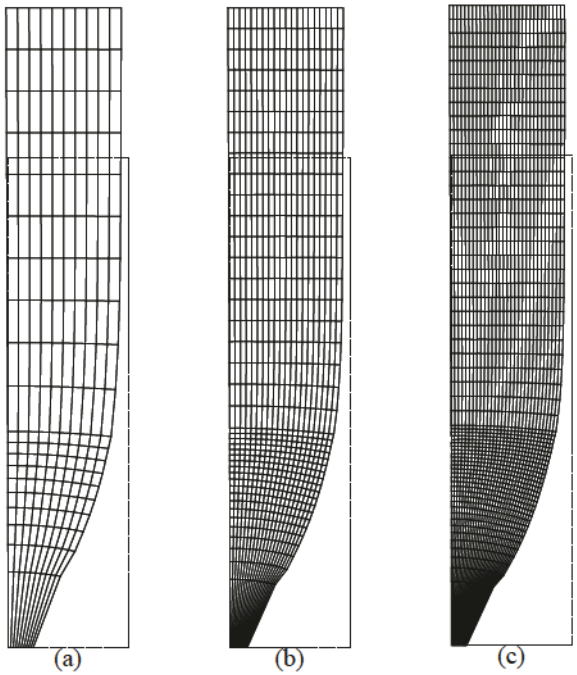

Figure 5.7: *Necking of a rectangular bar in plane strain. Initial and deformed shape for three different meshes with 200 (a), 800 (b) and 1800 (c) elements simulated without the nonlocal regularisation.*

In order to evaluate the accuracy of the nonlocal damage formulation used in the constitutive model, the three different simulations are performed with and without the nonlocal

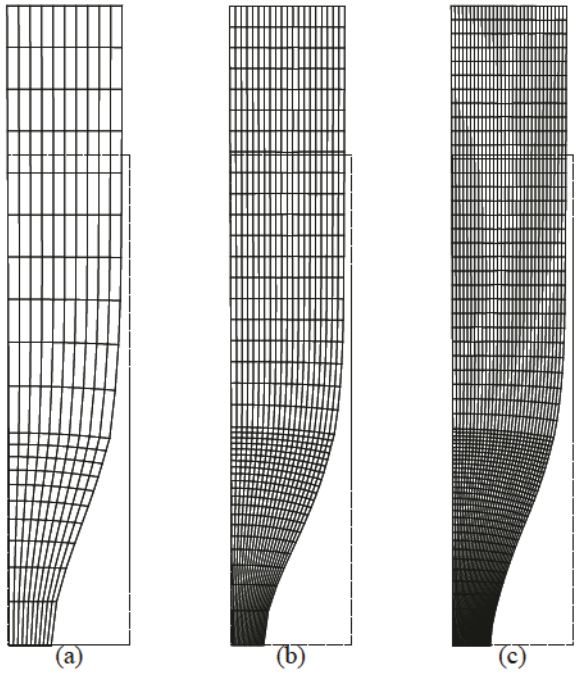

Figure 5.8: *Necking of a rectangular bar in plane strain. Initial and deformed shape for three different meshes with 200 (a), 800 (b) and 1800 (c) elements simulated with the nonlocal regularisation.*

damage regularisation. The nonlocal damage model is used with an intrinsic length of 1 mm. The corresponding initial and final deformed shapes of the rectangular bar simulated with the local damage model are shown in Fig. 5.7. For the three meshes simulated with the local model, larger deformations of the elements in the centre of the bar is observed. A localisation of the deformations in the elements where the necking occurs takes place. Fig. 5.8 shows the initial and final deformed shapes of the rectangular bar simulated with the nonlocal damage regularisation. The spurious localisation of the deformation in the elements at the necking does not occur. The deformations of the elements in the centre of the bar are not over-estimated in comparison with the around elements. The reaction forces at the bottom of the three meshes versus the displacements at the top boundaries are shown in Fig. 5.9. The three reaction forces obtained with the nonlocal formulation of the constitutive model are very close. In other way, the results carried out with the local damage model are mesh dependent, the spurious localisation of the deformations increases with the number of elements. It results a decrease of the reaction force in function of the number of elements. All the simulations have the same results in term of force until an axial elongation of 2mm. Unfortunately for an elongation larger than 2mm, the viscoplastic formulation is not enough to overcome the mesh dependency problem due to the softening behaviour. These results highlight the advantage of the nonlocal formulation in order

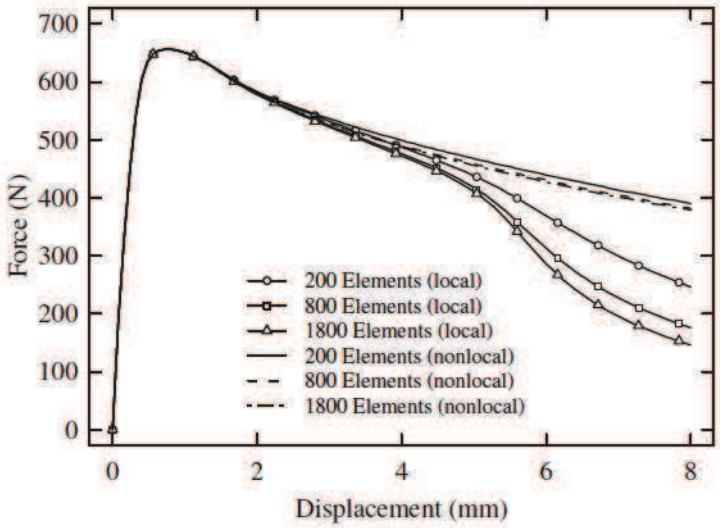

Figure 5.9: *Necking of a rectangular bar in plane strain. Forces versus displacements for the three finite element meshes and for the two damage models (nocal and nonlocal).*

to simulate the softening behaviour involved in the investigated material.

5.2.3 Three-dimensional cylindrical bar necking analysis

This example consists of the simulation of the necking of a cylindrical bar. The cylindrical bar with a length of 53.334 mm and a radius of 12.826 mm is subjected to uniaxial tension up to a total axial elongation of 8 mm (with a velocity of 1 $mm.s^{-1}$). For symmetry reasons, the analysis is performed on the eighth of the geometry with the appropriate boundary conditions. In order to evaluate the mesh sensitivity of the constitutive model, three dif-

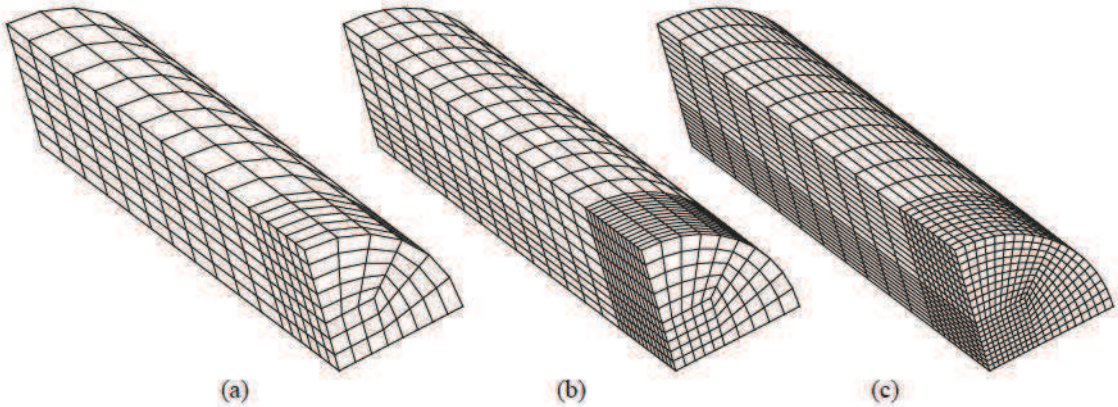

Figure 5.10: *Three-dimensional cylindrical bar necking. Finite element meshes of 663 (a), 2100 (b) and 6300 (c) elements.*

ferent meshes with 663, 2100 and 6300 reduced integrated eight node hexahedral elements are simulated with the constitutive model with and without the nonlocal damage model. The three different meshes are shown in Fig. 5.10. As in the example with the rectangular bar in plane strain, the three meshes contain a geometric imperfection of 1.8 % at the bottom in order to trig the necking in the centre of the cylindrical bar. In order to easily trig this necking, the material parameters α^+ used in the constitutive model is set to 0.5, a plastic Poisson ratio of 0.4 in tension is therefore obtained. An intrinsic length of 1 mm is used for the nonlocal regularisation. The deformed shapes which result to the simulations of the three meshes without the nonlocal regularisation is shown in Fig. 5.11. The same phenomenon like in the previous example is observed. Larger deformations of the elements in the centre of the bar is observed. A localisation of the deformations in the el-

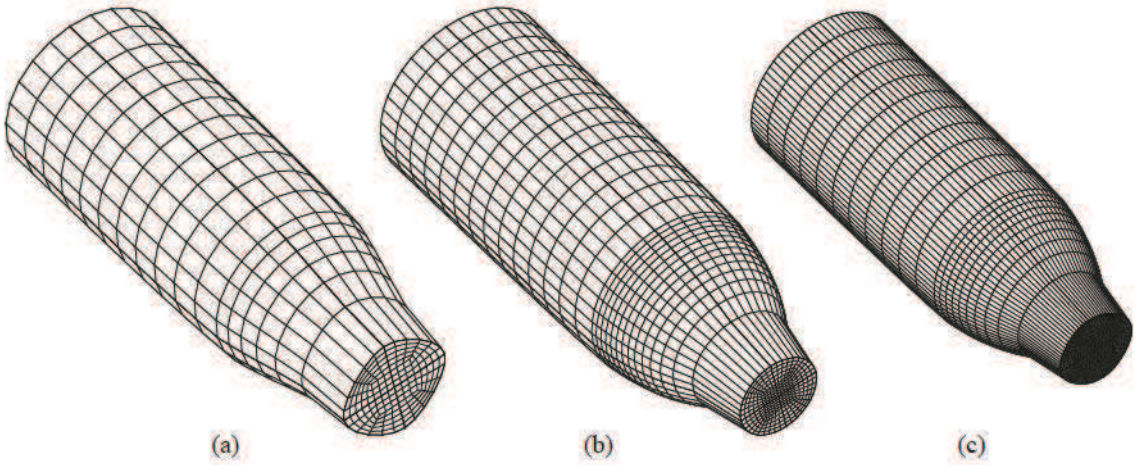

Figure 5.11: *Three-dimensional cylindrical bar necking. Deformed shapes for the three meshes with 663 (a), 2100 (b) and 6300 (c) elements simulated without the nonlocal regularisation.*

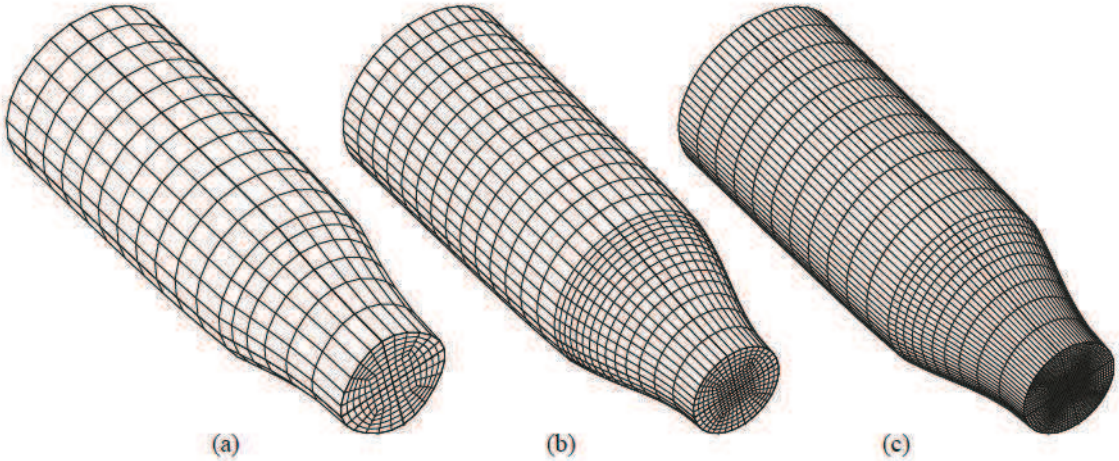

Figure 5.12: *Three-dimensional cylindrical bar necking. Deformed shapes for the three meshes with 663 (a), 2100 (b) and 6300 (c) elements simulated with the nonlocal regularisation.*

ements where the necking occurs take place. Fig. 5.12 shows the deformed shapes for the three meshes simulated with the nonlocal model. No localisation of the deformation in the elements which are situated at necking occurs. The general shapes of the elements located around the necking are uniform. The reaction forces in the bottom of the three meshes versus the displacements at the top boundaries are shown in 5.13. The simulations carried out with the local damage model have the same results in term of force-displacement until an axial elongation of 2mm. For a more important elongation the responses of these simulations become mesh dependent. By using the constitutive model with the nonlocal version of the damage model, the responses of the simulations are very close. A small difference with the coarse and the two fine meshes is observed. The coarse mesh does not describe enough accurately the geometry of the cylindrical bar. Fig. 5.14 shows the ratio between the initial and the current radius at the necking for the three meshes simulated with the nonlocal damage model. With the coarse mesh the simulation does not predict accurately the final radius at the necking. The two other meshes have a prediction of the radius very close and the difference with the coarse mesh is therefore a mesh convergence problem. The same conclusions that in the previous example are therefore deduced. At the start of the simulation, the viscoplastic formulation of the constitutive model brings an insensitive solution. However, with an higher deformation where the necking occurs, the local damage model does not predict accurately the geometry of the cylindrical bar. In this case, the nonlocal damage averaging play its rule of localisation limiter and the results becomes mesh independent for a finite element mesh enough dense.

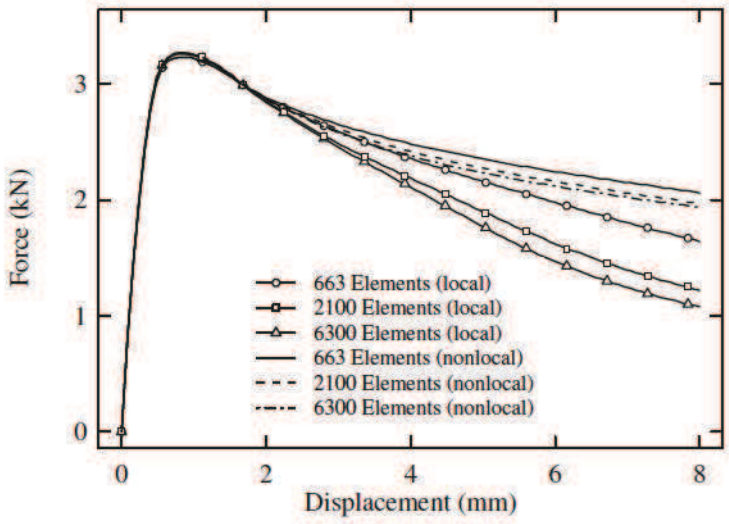

Figure 5.13: *Force response of the simulations for the 3 different meshes and the two damage models (local and nonlocal).*

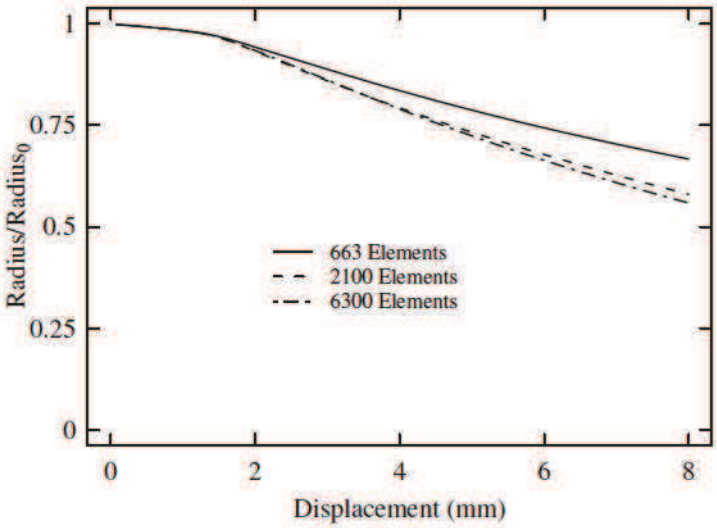

Figure 5.14: *Ratio between the initial and the current radius at the necking for the three meshes simulated with the nonlocal damage model.*

5.2.4 Notched specimen under uniaxial tensile loading analysis

The numerical tests carried out in this section are fulfilled on a notched specimen loaded in uniaxial tension. In order to evaluate the mesh dependency of the constitutive model on the numerical responses, two finite element meshes, with 253 and 1150 shell elements are used for the simulations. The simulations are performed with reduced integrated shell elements where 3 integration points through the thickness are used. The geometry, boundary conditions and finite element meshes are shown in Fig. 5.15.

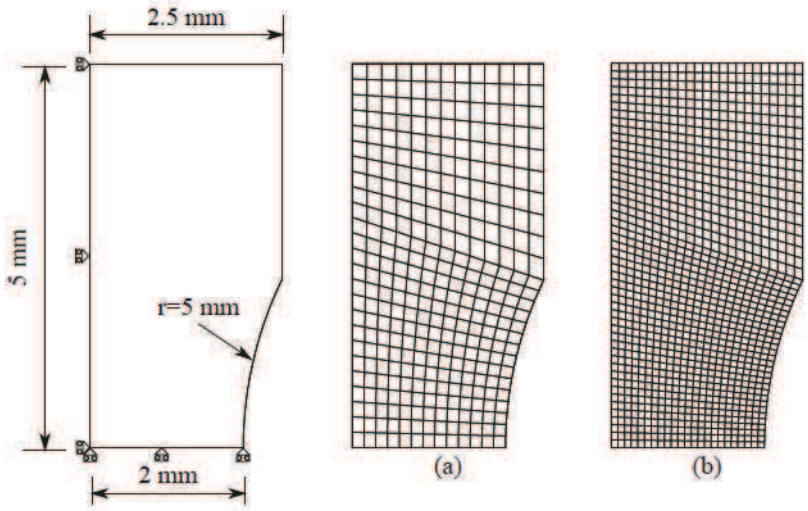

Figure 5.15: *Notched plate. Geometry, boundary conditions and finite element meshes: 325 (a) and 1150 (b) elements.*

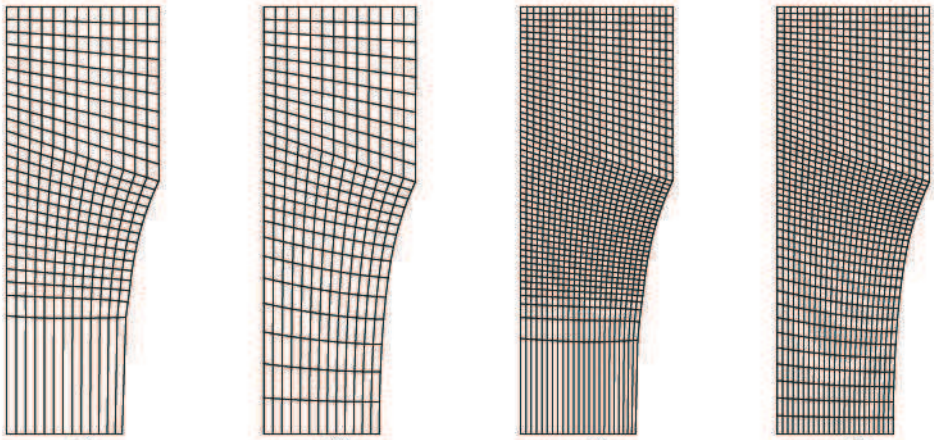

Figure 5.16: *Notched plate analysis. Deformed shape for the two meshes carried out without nonlocal regularisation (a) and (c), with the nonlocal regularisation (b) and (d).*

The loading consists of a prescribed monotonic velocity of the nodes on the top edge of the meshes up to a total axial elongation of 2 mm (with a velocity of 1 mm.s^{-1}). The constitutive model is used with and without the nonlocal regularisation as in the two previous examples. The simulations with the nonlocal damage model are carried out with an intrinsic length of 1 mm. The final deformed shapes for the two meshes simulated with and without the nonlocal regularisation is shown in Fig. 5.16. The obvious influence of the nonlocal damage model is highlighted by theses results. As already shown in the two previous examples, the two simulations carried out without the nonlocal averaging exhibit localisation of the deformation in the elements placed in the centre of the notch. The nonlocal damage model predict a more realistic solution where all the deformation is not contained in the elements at the centre of the notch. The reaction forces in the bottom of the two meshes versus the displacements at the top boundaries are shown in Fig. 5.17. The reaction forces calculated with the nonlocal damage model are exactly the same. In other way, the responses predicted with the local damage model are mesh-dependent.

Influence of the intrinsic length

In order to evaluate the influence of the intrinsic length (i.e. interaction radius) used in the nonlocal damage model, the coarse finite element mesh of the notched plate under uniaxial loading is simulated with different values of the intrinsic length: 1 mm, 0.5 mm, 0.3mm and 0mm (i.e. local model). The same boundary conditions are therefore used but with a final displacement of 1 mm. Fig. 5.18 shows the reaction forces calculated for all the simulations. The size of the intrinsic length has therefore an influence on the force response of the simulation. The force response decreases when the intrinsic length decreases until the

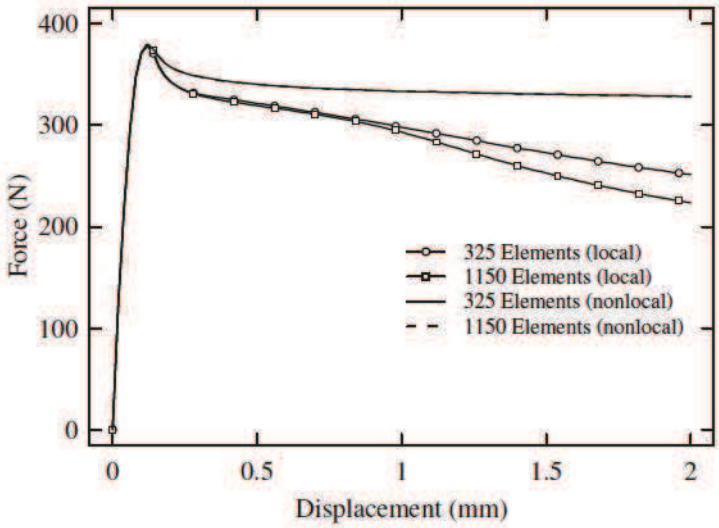

Figure 5.17: *Force response of the simulations for the two different meshes and the two damage models (local and nonlocal).*

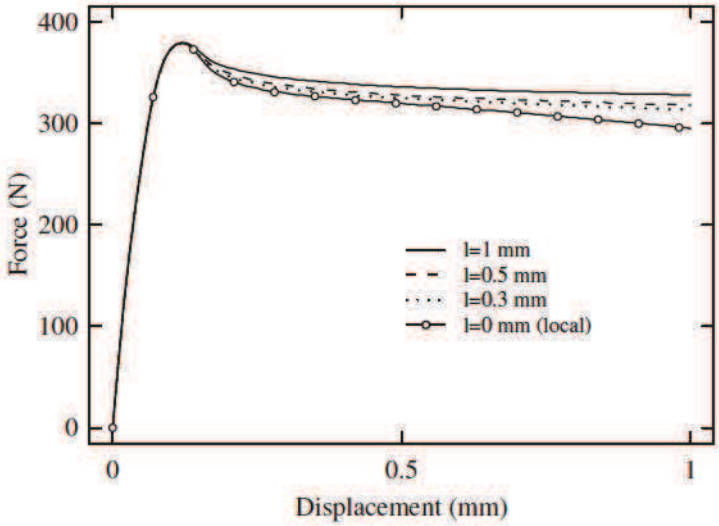

Figure 5.18: *Sensitivity of the interaction radius on the force responses.*

response of the local damage model (i.e. intrinsic length of 0 mm). The intrinsic length has therefore an influence on the deformations (axial and transversal). Fig. 5.19 shows the influence of the intrinsic length on the damage value. An increase of the damage value (i.e. equivalent viscoplastic strain) is observed for a decrease of the interaction radius. The damage values of the elements located in the notch (taken longitudinally) for the simulations carried out with the four interaction radius are shown in Fig. 5.20. When the intrinsic length decreases the deformation in the notch is more localised and the damage value in-

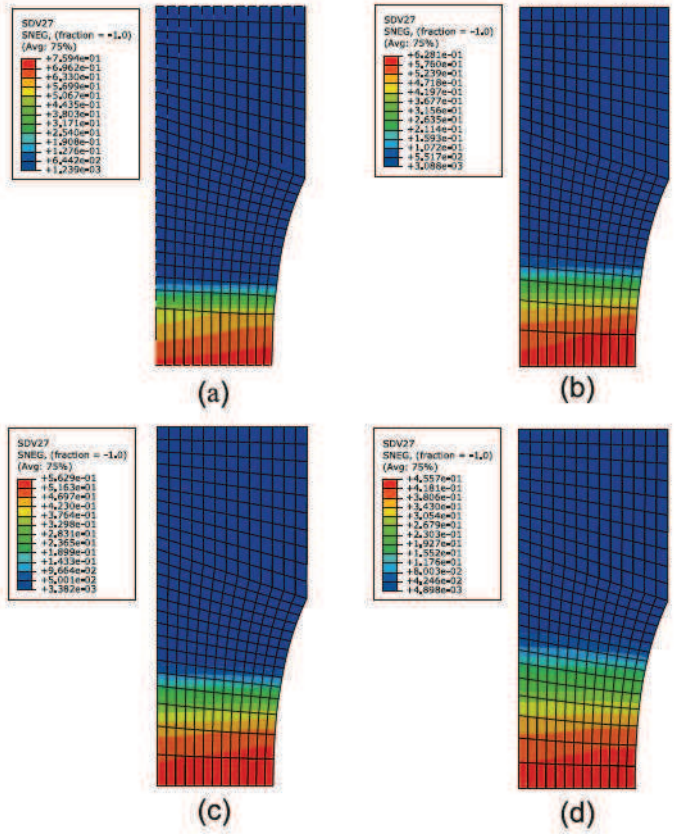

Figure 5.19: *Damage contour plotted for the notched plate simulation carried out with different intrinsic lengths: 0 mm (a), 0.3 mm (b), 0.5 mm (c) and 1mm (d).*

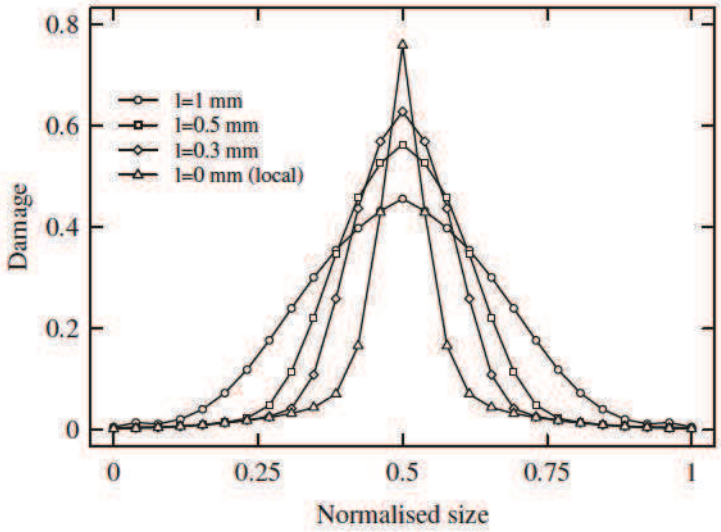

Figure 5.20: *Sensitivity of the interaction radius on the damage values.*

creases. This figure highlights the influence of the intrinsic length on the repartition of the damage (i.e. viscoplastic strain) around the notch. This result shows the localisation limiter rule of the nonlocal damage model which is implemented in the constitutive model. In order to simulate accurately the material being studied, the intrinsic length needs to be chosen according to the experimental observations.
This analysis shows the influence of the nonlocal damage model on the numerical responses for the simulation of a notched plate with continuum shell elements. More generally, when the deformation is not so localised, like in a straight tensile specimen, the rate-dependent formulation of the viscoplastic model ensures mesh insensitive responses despite of the softening behaviour. However, for a localised deformation, like a notched plate or the necking in a cylindrical bar, the nonlocal damage model is necessary to ensure the independence of the mesh on the numerical response.

5.3 Comparison of the numerical model with the experimental tests

5.3.1 Validation of the model on uniaxial tensile tests

The numerical uniaxial tensile tests presented in this section are carried out for the 5 following loading speeds: 1, 100 $mm.min^{-1}$, 0.08, 0.8 and 4 $m.s^{-1}$. The geometry of the specimen, boundary conditions and finite element mesh are shown in Fig. 5.1 (Section 5.1). For the simulations, the specimen is meshed with reduced integrated shell elements and 3 integration points through the thickness are used. The loading consists on a prescribed monotonic velocity (with free horizontal displacement) on the nodes of the right edge of the mesh. The comparisons between the constitutive model and the experimental data are shown in Fig. 5.21. The reaction forces at the left of the specimens versus the displacements enforced at the right boundaries are compared with the experimental data. The constitutive model results are in agreement with the experimental measurements for all the speed loadings. In order to show the accuracy of the viscoelastic model, Fig. 5.22 shows the comparison between the numerical model and the experimental data for three speed loadings: 1, 50 $mm.min^{-1}$ and 0.08 $m.s^{-1}$. The results are focused on the first part of the curves where the viscoelastic part can be visualised easily. The numerical model has a good prediction of the stiffness of the material loaded at various speed loadings. In order to compare the evolution of the local logarithmic strains (longitudinal and transverse) of the numerical model with the experimental observations, Fig. 5.23 shows the true stresses (Cauchy)-strains (logarithm) responses of one element in length gauge of the specimen given by the numerical

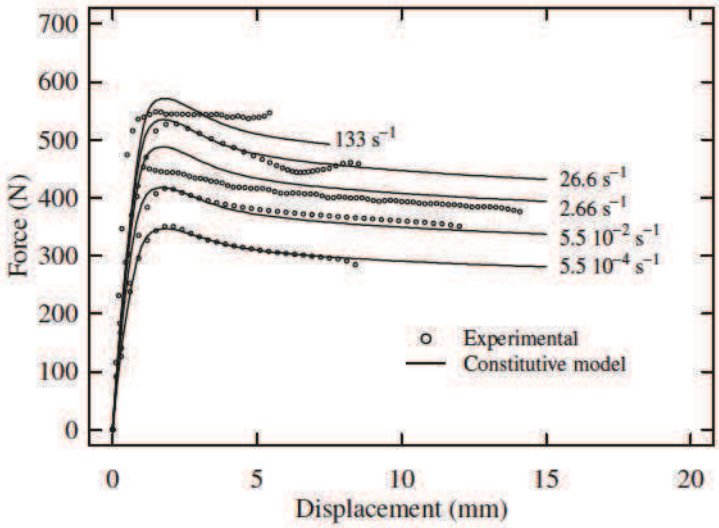

Figure 5.21: *Experimental vs. constitutive model in uniaxial tensile loading.*

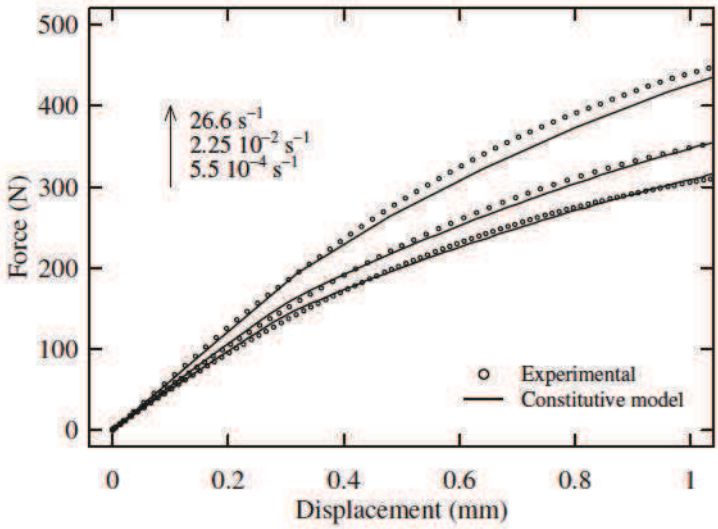

Figure 5.22: *Experimental vs. constitutive model in uniaxial tensile loading.*

model with the experimental measurement (by DIC) for 4 different speed loadings. The experimental stresses-strains values arise from the SEĖ method, they are therefore given for all the ZOI of the specimen. In the same way, the volumetric logarithm strains measured by DIC (calculated with the SEĖ method on each ZOI) at the same speed loadings are compared with the numerical model in Fig. 5.24. The numerical model is in agreement with the experimental data for all the speed loadings.

The combination of the behaviour law deduced from the SEĖ method with the damage leads to a good description of the true stress. In terms of local strains, the lon-

gitudinal and transverse logarithmic strain components are well captured by the non-associative viscoplasticity as the comparison of the volume variation (volumetric strain) shows (Fig. 5.24).

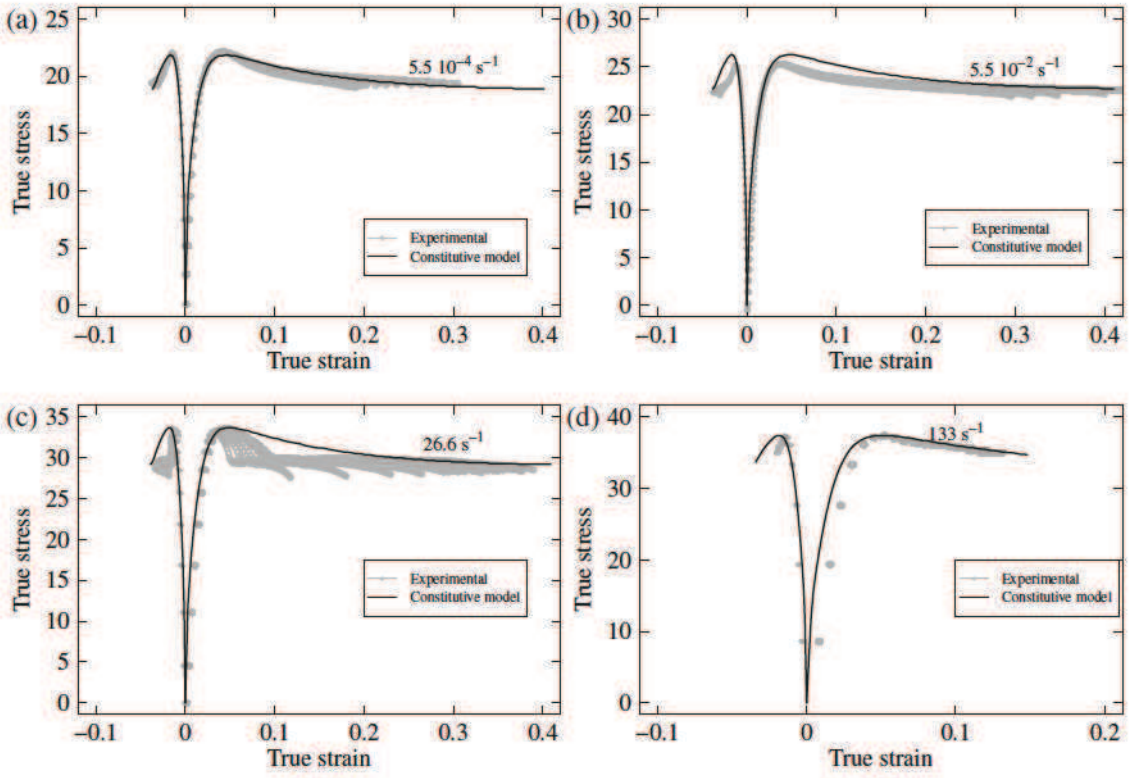

Figure 5.23: *True stresses (Cauchy) versus true strains (longitudinal and transverse logarithmic) comparison between the numerical model and the experimental data at 5.5 10^{-4} s^{-1} (a), 5.5 10^{-2} s^{-1} (b), 26.6 s^{-1} (c) and 133 s^{-1} (d).*

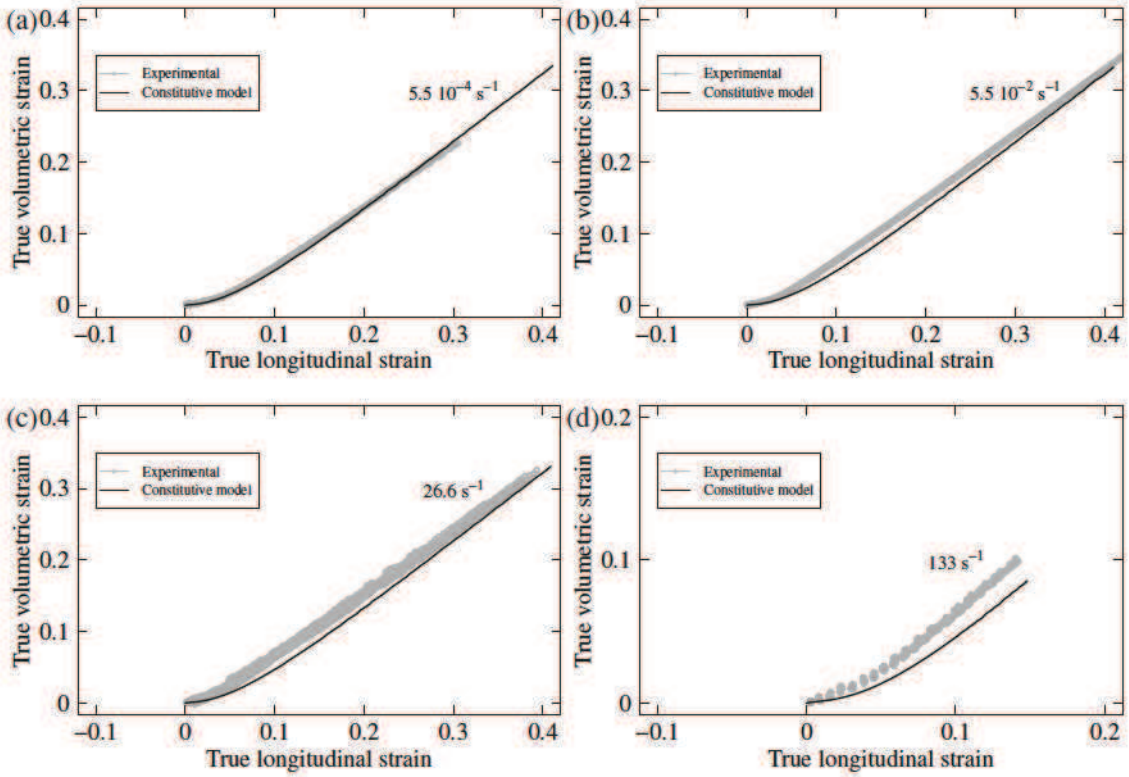

Figure 5.24: *Volumetric logarithmic strains comparison between the numerical model and the experimental data at 5.5 10^{-4} s^{-1} (a), 5.5 10^{-2} s^{-1} (b), 26.6 s^{-1} (c) and 133 s^{-1} (d).*

5.3.2 Validation of the model on notched tensile specimens

In order to validate the constitutive model on notched tensile specimens, experimental uniaxial tensile tests are carried out on 2 notched specimens with two different radius, 2 and 5 mm. The experimental tests are performed on the electromechanical device (INSTRON E3000) with two loading speeds 1 and 100 mm.min^{-1}. As uniaxial tensile tests, the Digital Image Correlation is used for the local strain measurements (logarithmic). The geometries, boundary conditions and finite element meshes of the specimens are given in Fig. 5.25. The specimens are meshed with reduced integrated shell elements and 3 integration points through the thickness are used. A prescribed velocity is applied at the top nodes of the specimens. In order to compare the logarithmic strains of the numerical model with the experimental tests, the size of ZOI (Zone of Interest) used in the digital image software VIC 2D® is the same as the finite element meshes in the centre of the specimens (0.2 mm). The simulations of the tensile tests with the notched specimens are performed with the constitutive model with the nonlocal damage model. Different intrinsic lengths (0.3, 0.5 and 1mm) are tested in order to obtain the simulation which have the better agree-

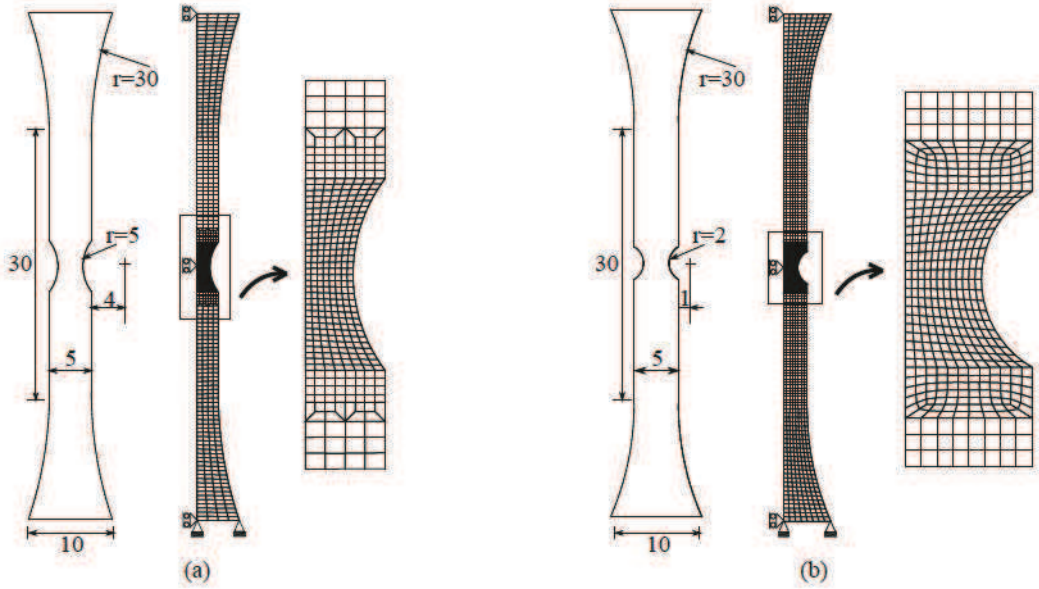

Figure 5.25: *Geometries, boundary conditions and finite element meshes of the two notched specimens with radius of 5 mm (a) and 2 mm (b).*

ment with the experimental observations. Fig. 5.26 shows the longitudinal logarithmic strains comparison between the constitutive model with three different intrinsic lengths and the experimental test carried out on the notched specimen with a radius of 5 mm at 1 mm.min^{-1}. The logarithmic longitudinal strains shown in Fig. 5.26 are measured in the same place of the specimen, in the centre of the notch where the deformation is higher.

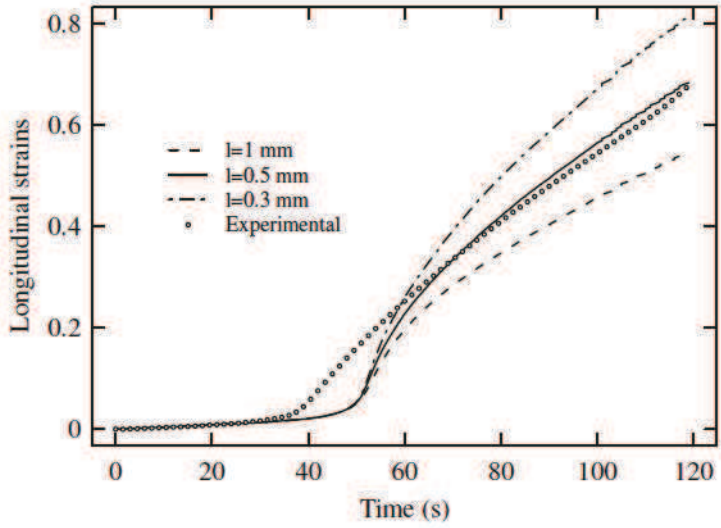

Figure 5.26: *Logarithmic strain comparison between the experimental test at 1 mm.min^{-1} with the numerical model with three different intrinsic lengths: 1 mm, 0.5 mm and 0.3 mm.*

Regarding Fig. 5.26, the obvious better intrinsic length is therefore 0.5 mm. The longitudinal logarithmic strain is under estimated with an interaction radius of 1mm and over estimated with a value of 0.3. These results highlight the importance of the nonlocal regularisation in order to model accurately the real behaviour of the material. Fig. 5.27 shows the logarithmic strains (longitudinal and transverse) comparison between the experimental test carried out on the notched specimen with the radius of 5 mm at 1 $mm.min^{-1}$ with the numerical simulation. As shown with the results on the uniaxial tensile specimens, the non-associated viscoplastic formulation of the constitutive model is able to predict the volume change of the material. The longitudinal and transverse strains are well predicted by the constitutive model. The comparison of reaction forces predicted by the numerical model with the experimental tests for the two loading speeds and with the two geometries are given in Figs. 5.28 and 5.29, respectively. The numerical model is in agreement with the experimental data for the two geometries and for the two speed loadings. The strain rate and the pressure[§] sensitivity is well captured by the constitutive model. However, for the two geometries, the softening slope seems to decrease with an increasing strain rate. This slope variation with the strain rate is not observed on the uniaxial tensile loading with tensile specimens. The constitutive model is therefore not able to reproduce this phenomenon.

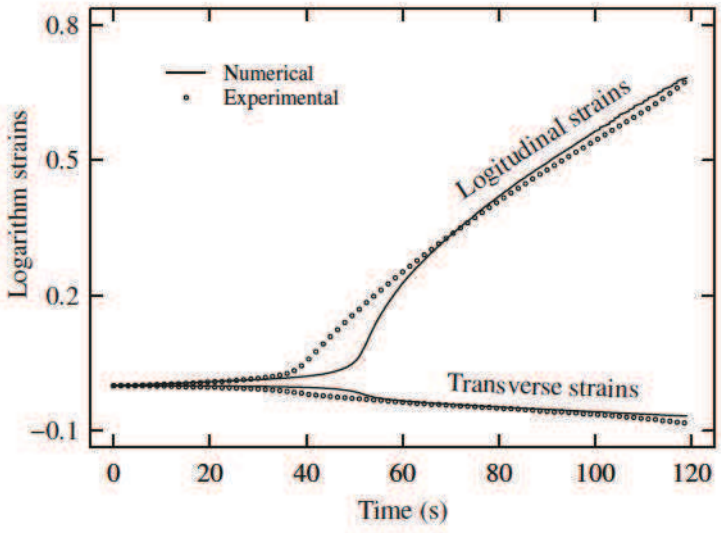

Figure 5.27: *Logarithmic strains (longitudinal and transverse) comparison between the experimental test at 1 $mm.min^{-1}$ with the numerical model on the notched specimen (radius=5 mm).*

[§]The two geometries of the notched tensile specimens (r=5 and r=2) have a initial triaxial stress ratio of 0.4 and 0.5, respectively.

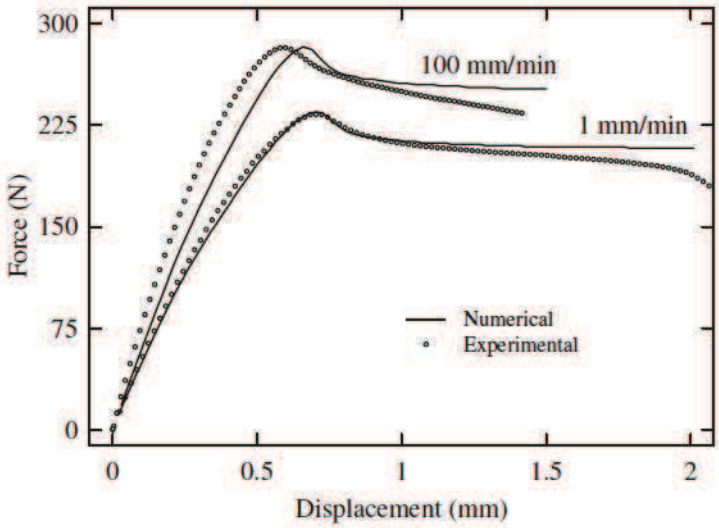

Figure 5.28: *Comparison between the experimental tests and the numerical model on the notched specimen (radius=5 mm) in term of force displacement.*

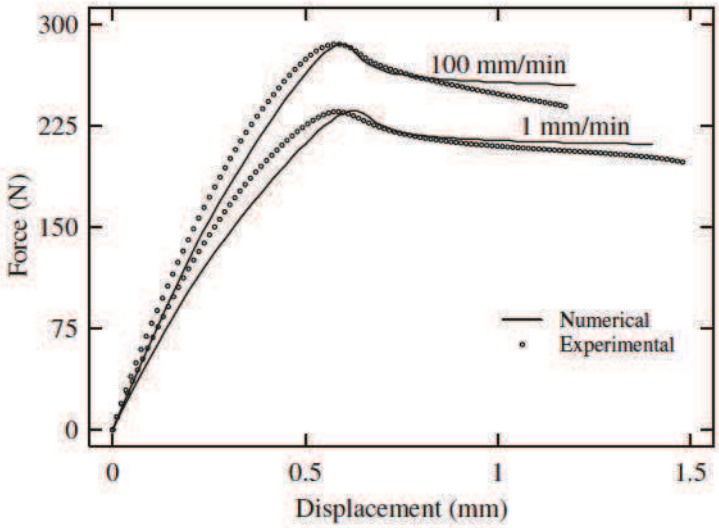

Figure 5.29: *Comparison between the experimental tests and the numerical model on the notched specimen (radius=2 mm) in term of force displacement.*

5.3.3 Validation of the model on uniaxial compression tests

The experimental uniaxial compression tests carried out on cylindrical specimens are simulated in order to validate the constitutive model under compressive loading. The cylindrical specimen used to simulate the uniaxial compression tests is modelled with reduced integrated eight noded-hexahedral elements in order to avoid the locking effect. For a more efficient solution, the analysis is performed on a quarter of the section with appro-

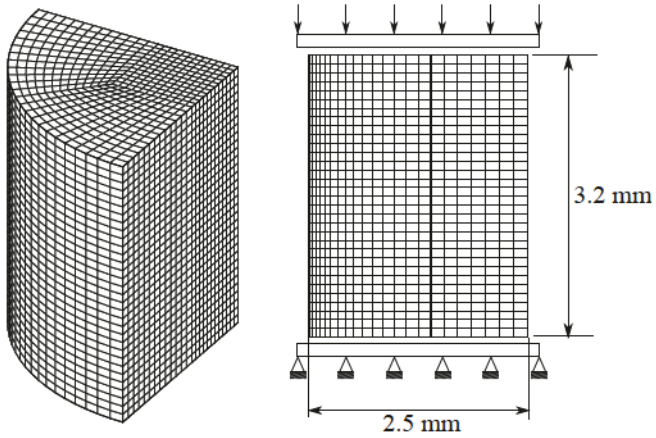

Figure 5.30: *Finite element mesh and boundary conditions for uniaxial compression tests.*

priate boundary conditions. The analysis is carried out with two rigid bodies which are in contact with the specimen at the top and at the bottom with a friction coefficient of 0.05. The loading consists of a prescribed monotonic velocity (with free vertical displacement) imposed on the rigid body placed on the top of the specimen. Two speed loading, 1 $mm.min^{-1}$ and 1 $mm.s^{-1}$ are used. The other rigid body (at the bottom of the specimen) has its displacement following the loading direction clamped. The geometry of the specimen, boundary conditions and finite element mesh are shown in Fig. 5.30. Due to the absence of softening under compression loading the local version of the damage is used in the two simulations. The comparison between the numerical simulations and the experimental tests in uniaxial compression loading is shown in Fig. 5.31.

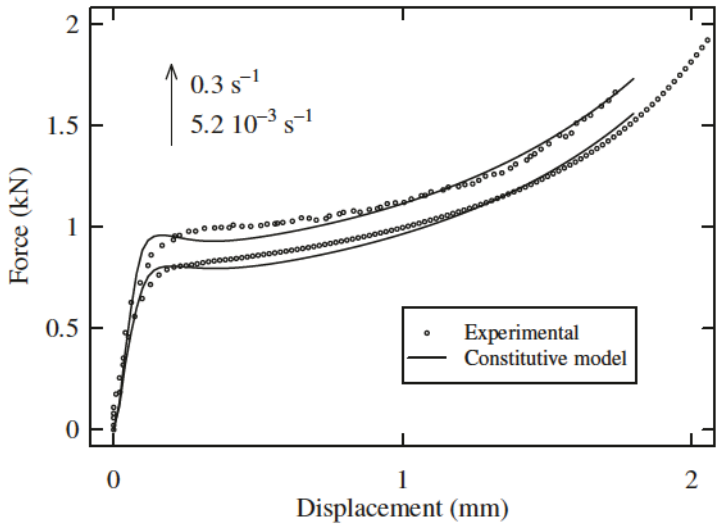

Figure 5.31: *Reaction force comparison between the numerical model and the experimental data at 1 $mm.min^{-1}$ and 1 $mm.s^{-1}$.*

The reaction forces versus the displacements predicted by the constitutive model are in agreement with the experimental tests. The strain rate effect, pressure sensitivity and hardening evolution is well captured by the constitutive model.

Influence of the material parameter α^-

In order to evaluate the influence of the material parameter α^- introduced in the viscoplastic potential flow, two other simulations at 1 mm.min^{-1} are performed with different values of α^-, 0 and 3.27. As under tensile loading the parameter α^+ has an influence on the dilatation of the material, under negative hydrostatic pressure the material parameter α^- controls the compaction of the material. Fig. 5.32 shows the deformed shapes of the three simulations performed with different values of α^-: 0, 0.5 and 3.27.

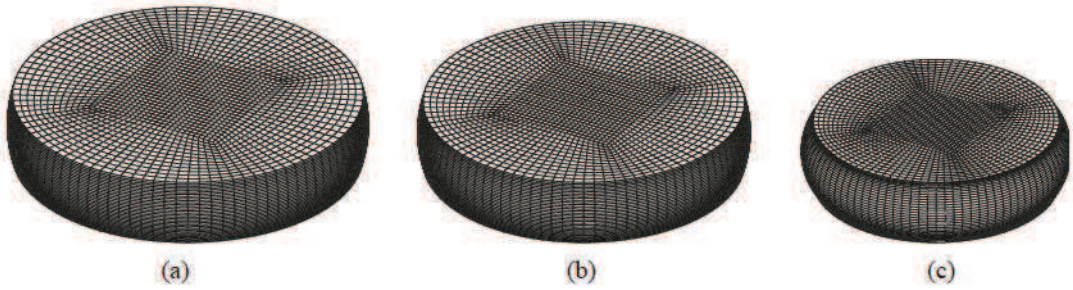

Figure 5.32: *Final deformed shapes of the compression tests simulated with three values of* α^-*: 0 (a), 0.5 (b) and 3.27 (c).*

The three deformed shapes are represented at the same scale. The final shapes of the specimens are very different. A decrease of the final volume is observed for an increase of α^-. Fig. 5.33 shows the volumetric strain in function of the global longitudinal strain. The global volumetric strain is calculated with the volume predicted by the constitutive model following $e_v = \ln\left(\frac{V_0}{V}\right)$, where V_0 and V are the initial and current volumes, respectively. A decrease of the volumetric strain is therefore observed with the increase of α^-. Unfortunately, due to the small size of the cylindrical specimen, it is not possible to follow the evolution of the volumetric strain during an experimental test by Digital Image Correlation.

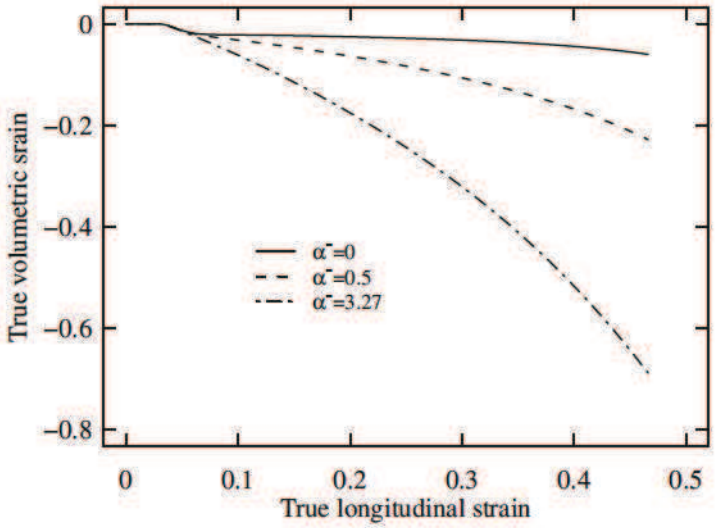

Figure 5.33: *Evolution of the volumetric strain predicted by the constitutive model with three values of* α^-.

5.4 Conclusions

The obvious mesh dependency problem caused by the softening behaviour of the material being studied is overcome in the constitutive model. Under loadings where the deformation is not so localised, the viscoplastic formulation of the constitutive model is enough to obtain a mesh independent response. Where the major part of the deformation is localised in a small zone of the specimen, the mesh independence is obtained by using the nonlocal damage model. In this case, the intrinsic length of the material needs to be chosen according to the experimental observations. The proposed constitutive model is able to reproduce the strain rate effect, the pressure dependency and the volume variation which exhibits the semi-crystalline polymer modelled. The comparison between the numerical model and the experimental data reveals good correlations with straight and notched specimens under tensile loadings and in compression loadings as well. The reaction forces versus displacements predicted by the constitutive model are in accordance with the experimental tests. Furthermore, in a more local point of view, the comparison of the local Henky strains given by the numerical simulations and measured by Digital Image Correlation highlights the modelling of the volume variation which is crucial for polymeric material.

Chapter 6

Conclusions and future perspectives

Due to the common use of polymeric materials in industrial applications, their behaviours are still widely investigated nowadays. The mechanical performance in term of stiffness, strength, ductility and the processability of the thermoplastics are the reasons of their common employment in structural applications (e.g. in automotive sector). Semi-crystalline polymers, as polypropylene, are good candidates to obtain these specifications. The nature of their micro-structure (i.e. amorphous and crystalline phase) yields to complex deformation mechanisms with many external factors influencing their behaviour. The temperature, rate, time and pressure dependency of these materials lead to their characterisation and modelling complex. Furthermore, in the interest of decreasing the cost and increasing the mechanical performances, fillers have been added in polymeric materials. In this context, a mineral filled semi-crystalline (polypropylene) polymer used in automotive sector has been investigated in this thesis.

Experiments conducted at several speeds and loadings with Digital Image Correlation and optical extensometry for the strain and displacement field measurements, have highlighted the pressure and rate dependency accompanied to non-isochoric deformation*. Magnifications SEM micrograph of the fracture surface under tensile loading at 1 $mm.min^{-1}$ have shown nucleation of cavities around the mineral fillers. Adding inorganic and rigid fillers in semi-crystalline polymers bring out the damage process during the material deformation.

A constitutive model developed in the framework of the continuum mechanics based on state variables has been proposed in order to predict the observed phenomena. In the

*The isothermal deformation is considered in this thesis

developed model, damage coupled with viscoelasticity-viscoplasticty in a non-associated manner is used to describe the behaviour of the polymeric material. In this model, the linear viscoelastic Wierchert model, a pressure dependent yield surface and a phenomenological damage model are coupled with a viscoplastic dissipation potential able to describe the dilatation and the compaction of the material independently. This model is developed for three- and two-dimensional elements (i.e. eight-node hexahedral and four-node quadrilateral under plane strain condition) and continuum shell elements. The stress update procedure has therefore been modified by a second iteration loop in order to respect the plane stress condition (i.e. thickness stress must vanish) to use the proposed model with shell elements. The constitutive model is implemented under finite strain framework in two finite element codes, implicit and explicit, ABAQUS/Standard®and LS-DYNA®, respectively. In order to retain the material frame indifference during large deformations/rotations, an hypoelastic formulation of the viscoelastic-viscoplastic model using the corotational rate of the Cauchy stress with the polar spin tensor (i.e Green-Naghdi rate) is proposed in the constitutive model.

Comparisons of simulations carried out with the constitutive model and experiments show good results in term of pressure and rate dependency and also volume variation of the developed model. These comparisons have been carried out on several loadings (straight and notched tensile and compression) and strain rates. The numerical responses in term of force-displacement are also in good agreement with the experimental ones. In term of volume variation, the comparison of strains under tensile with straight and notched specimens have shown that the non-isochoric deformation of the material is well modelled with the proposed viscoplastic dissipation potential. The small size of the compression specimens does not allow to use the Digital Image Correlation technique for the strain field measurements, the local strains predicted by the constitutive model can therefore not be compared with the experiments. Nevertheless, the proposed viscoplastic flow rule is able to describe the compaction of the material by the parameter α^{-}.

The damage involved in the deformation of the mineral-filled semi-crystalline polymer causes a decrease of stress at increasing strain. This softening behaviour leads to the mesh dependency pathology arising to localisation of the deformations in a narrow zone of the finite element model. Examples carried out with various element types and under several conditions: straight and notched plates under tensile loading and necking analysis of plane strain and cylindrical bar, have revealed that the rate-dependent formulation is able to predict mesh independent solutions when the deformation is not so localised as a straight specimen under uniaxial tensile loading. In the case where the deformation is more localised, as in a notched specimen or during the necking of a bar, the regularisation

by the viscoplastic formulation is not enough efficient to ensure mesh independent results. The nonlocal formulation of the damage model, implemented in a simple manner, with a penalty factor calculated by the ratio between of the nonlocal averaging of the rate damage variable with its local value, has proven its efficiency for localised deformation. With the introduction of the intrinsic length in the constitutive model, mesh independent results are obtained under several loadings and problem dimensions.

Future perspectives

Future researches can be focused on the fracture modelling of the material investigated. The experiments carried out with Digital Image Correlation at several speeds and loadings have shown that the strain rate and the triaxiality have an influence on the fracture. No fracture is observed in compression loading for all the strain rates. Concerning the straight tensile specimens, an increase of the true fracture strain with an increase of the true strain rate is observed until an equivalent strain rate of 10^{-1} s^{-1}. Beyond this "critical" value, at increasing strain rate a decrease of the fracture strain is observed. For the notched specimens (with radius of 2 and 5 mm), this tendency is not similar, a decrease of the fracture strain for an increasing strain rate is observed. These results are shown in Fig. 6.1. Due to the influence of the size of the ZOI on the strain value, all the strain values calculated by the DIC software have been extrapolated with a base of measurement of 1 mm. This

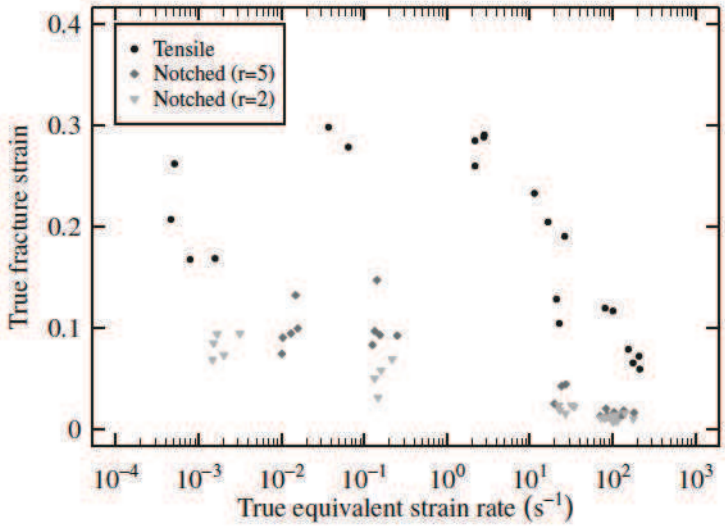

Figure 6.1: *True equivalent fracture strains versus true strain rates for straight and notched specimens under uniaxial tensile loading.*

extrapolation is fulfilled with the following expression

$$\kappa_f = \ln\left(1 + \frac{l_0^{\mathrm{DIC}} \exp(\kappa^{\mathrm{DIC}}) - l_0^{\mathrm{DIC}}}{l_0}\right) \tag{6.1}$$

where κ_f is the true equivalent fracture strain, l_0 is the desired size of measurement, κ^{DIC} and l_0^{DIC} are, respectively, the true equivalent fracture strain calculated with its corresponding ZOI size, i.e. l_0^{DIC}. This extrapolation is made in order to compare the results of all the experiments with various base of measurements. Furthermore, due to the scattered fracture strain values observed on the straight specimens, only the more representative values are represented in Fig. 6.1. The obvious triaxiality influence on the fracture strain is highlighted by Fig. 6.1. The irregular strain rate influence on the tensile tests in term of fracture may be explained by the cavitation phenomenon. The material investigated is a mineral filled polypropylene where the decohesion at filler-matrix interface occurs during deformation (i.e. nucleation, growth and coalescence of cavities). Magnification SEM micrograph of the fracture surface under tensile loading at 10^{-3} s^{-1} is shown in Fig. 6.2(a). This fracture surface presents many cavities and an important decohesion between the mineral fillers and the matrix. Fig. 6.2(b) shows the magnification SEM micrograph of the fracture surface for the tensile test in dynamic for an approximate strain rate of 300 s^{-1}. This fracture surface is very different as the previous one. At this strain rate (i.e. 300 s^{-1}) no decohesion at filler-matrix interface occurs. For relative low strain rate, the cavitation phe-

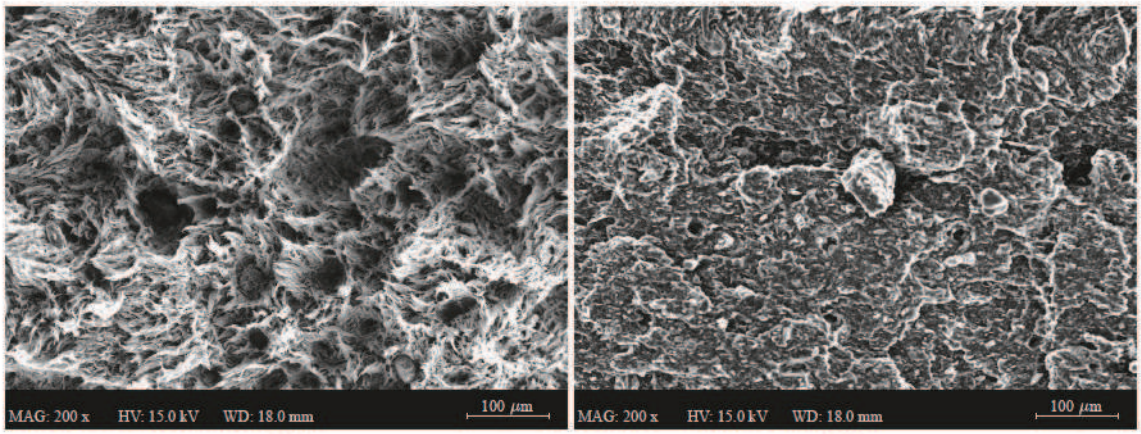

(a) (b)

Figure 6.2: *Magnification SEM micrograph of the fracture surface of mineral filled polypropylene under tensile loading at* 10^{-3} s^{-1} *(a) and hight magnification SEM micrograph of the fracture surface of mineral filled polypropylene under tensile loading at 300* s^{-1} *(b).*

nomenon occurs and the fracture strain value is relatively low due to the important number of cavities. When the strain rate increases sufficiently (around 10^{-1} s^{-1}), the decohesion at fillers-matrix interface is not dominant on the fracture process and the fracture strain is more dependent on the strain rate (i.e. decrease when the strain rate increases). Two kinds of fracture morphology are therefore observed, fibrillation (ductile) for low strain rate and brittle for higher strain rate. Fig. 6.3 shows a low magnification SEM micrograph of the fracture surface of the material studied under tensile loading at 10^{-1} s^{-1}. On this fracture surface, the two types of fractures are present, the ductile fracture (on the left), where the sample appears porous with its deformed fibrils and the brittle (on the right). The fracture is therefore initiated on the left where the voids are nucleated and, further, extended on the right of the specimen.

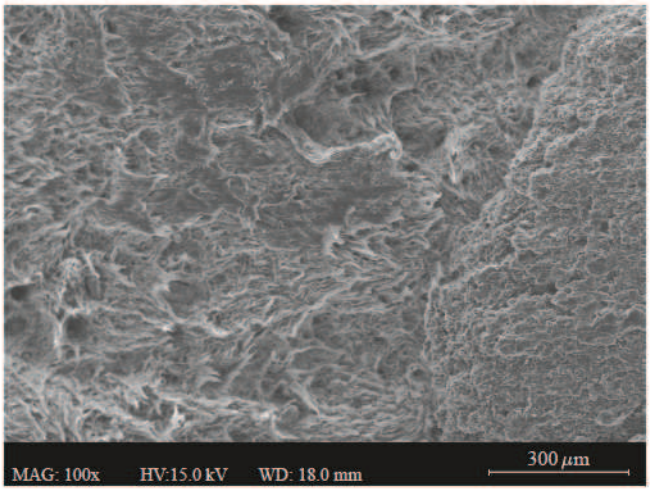

Figure 6.3: *Low magnification SEM micrograph of the fracture surface of mineral filled polypropylene under tensile loading at* 10^{-1} s^{-1} .

A fracture criterion which depends of the triaxial stress ratio and the strain rate can therefore be used in order to model the both fracture modes observed experimentaly. An interesting fracture criterion proposed by Wierzbicki *et al.* (2005); Xue (2007) which depends on the triaxial stress ratio and the lode angle can be used to model the triaxiality influence on the fracture. This criterion have been developed for aluminium material which does not exhibit strain rate dependency on the fracture. An extension of the above criterion can be developed in order to reproduce the strain rate effect on the fracture present in the polymeric material.

For further developments, it would be interesting to introduce in the model the effect of the initial temperature. As already seen in the literature, the initial temperature has a strong influence on the behaviour of the polymers and on the fracture as well. The manufacturing

process itself has an influence on the behaviour of parts. The injection flow with complex mould will introduce flow joints which can be weak points on parts. This new model is also a good start to introduce some reinforcement materials like short fibres into the polymer. It will be a really interesting challenge.

Appendix A

Data about experimental scattering

In order to present the scattering of the experimental responses, the following figures show the raw responses in term of force versus displacement for five tests under tensile loading with the straight specimens at 1 mm.min^{-1} and 4 m.s^{-1} and with the notched specimens (radius=5 mm) at 1 mm.min^{-1} .

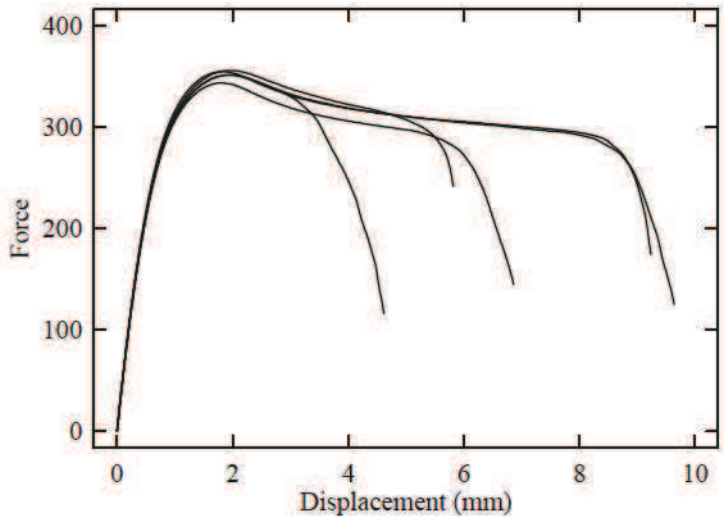

Figure A.1: *Force versus displacement of the straight specimens under uniaxial tensile loading at 1 mm.min^{-1}* .

As shown in Fig. A.1, the tests at 1 mm.min^{-1} have a good repeatability in term of behaviour but an important scattering is observed in term of fracture. The fracture scattering is classic

with straight specimens, the rupture depends on various factors like quality of cutting, initial defects, manufacturing ...

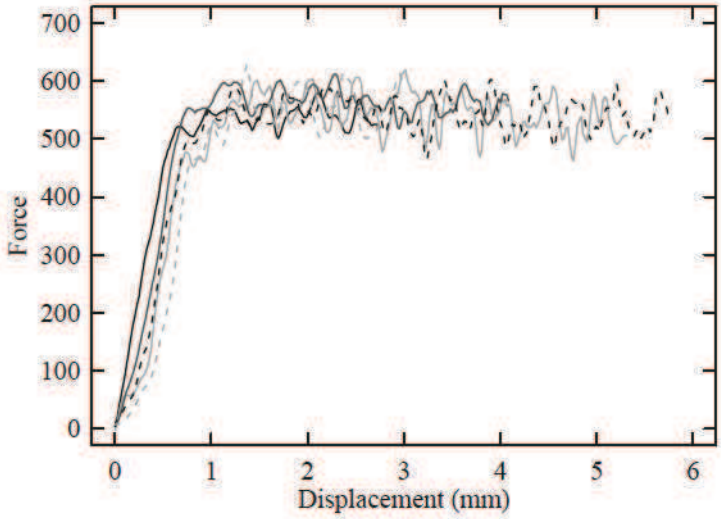

Figure A.2: *Force versus displacement of the straight specimens under uniaxial tensile loading at 4 $m.s^{-1}$.*

Due to the hydraulic device used for the tensile tests at 4 $m.s^{-1}$, noisy force-displacement curves are obtained (Fig. A.2). As in the quasi-static tests, an important scattering is observed in term of fracture.

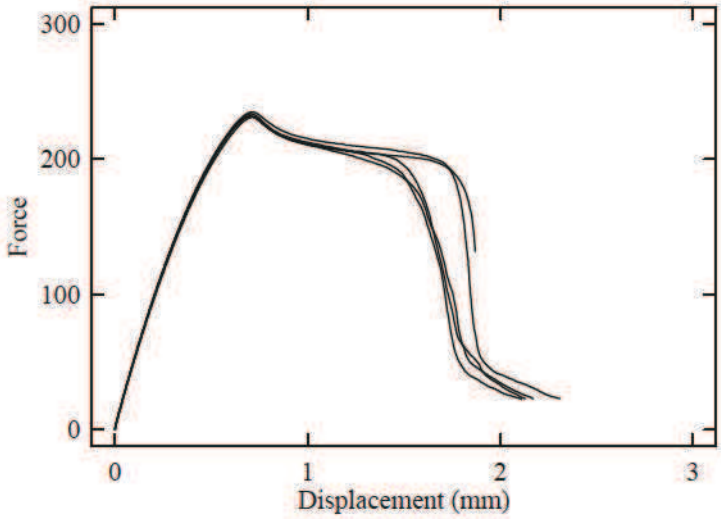

Figure A.3: *Force versus displacement of the notched specimens (r=5 mm) under uniaxial tensile loading at 1 $mm.min^{-1}$.*

As with the straight tensile specimens, a good repeatability is observed with the notched specimens (Fig. A.3) on the behaviour and due to the localisation of the deformation in the centre of the notch, a very low scattering on the fracture is shown for this kind of specimen.

References

Ahzi, S., Makradi, A., Gregory, R. and Edie, D. (2003). Modeling of deformation behavior and strain-induced crystallization in poly(ethylene terephthalate) above the glass transition temperature. *Mechanics of Materials*, **35**, 1139 – 1148.

Ames, N.M., Srivastava, V., Chester, S.A. and Anand, L. (2009). A thermo-mechanically coupled theory for large deformations of amorphous polymers. part ii: Applications. *International Journal of Plasticity*, **25**, 1495 – 1539.

Anand, L. and Ames, N. (2006). On modeling the micro-indentation response of an amorphous polymer. *International Journal of Plasticity*, **22**, 1123–1170.

Anand, L. and Gurtin, M.E. (2003). A theory of amorphous solids undergoing large deformations, with application to polymeric glasses. *International Journal of Solids and Structures*, **40**, 1465 – 1487.

Anand, L., Ames, N.M., Srivastava, V. and Chester, S.A. (2009). A thermo-mechanically coupled theory for large deformations of amorphous polymers. part i: Formulation. *International Journal of Plasticity*, **25**, 1474 – 1494.

Andrade, F.X.C., S, J.M.A.C.D. and Pires, F.M.A. (2011). A ductile damage nonlocal model of integral-type at finite strains: Formulation and numerical issues. *International Journal of Damage Mechanics*, **20**, 515–557.

Arruda, E.M. and Boyce, M.C. (1993). A three-dimensional constitutive model for the large stretch behavior of rubber elastic materials. *Journal of the Mechanics and Physics of Solids*, **41**, 389–412.

Ayoub, G., Zaïri, F., Naït-Abdelaziz, M. and Gloaguen, J. (2010). Modelling large deformation behaviour under loading-unloading of semicrystalline polymers: Application to a high density polyethylene. *International Journal of Plasticity*, **26**, 329–347.

Ayoub, G., Naït-Abdelaziz, M., Zaïri, F., Gloaguen, J. and Charrier, P. (2011a). A continuum damage model for the high-cycle fatigue life prediction of styrene-butadiene rubber under multiaxial loading. *International Journal of Solids and Structures*, **48**, 2458 – 2466.

Ayoub, G., Zaïri, F., Frderix, C., Gloaguen, J., Naït-Abdelaziz, M., Seguela, R. and Lefebvre, J. (2011b). Effects of crystal content on the mechanical behaviour of polyethylene under finite strains: Experiments and constitutive modelling. *International Journal of Plasticity*, **27**, 492 – 511.

Besson, J. (2009). Damage of ductile materials deforming under multiple plastic or viscoplastic mechanisms. *International Journal of Plasticity*, **25**, 2204 – 2221.

Besson, J., Cailletaud, G., Chaboche, J.L. and Forest, S. (2001). *Non-Linear Mechanics of Materials*. Solid Mechanics and Its Applications, DOI: 10.1007/978-90-481-3356-7.

Bodner, S.R. and Partom, Y. (1975). Constitutive equations for elastic-viscoplastic strain-hardening materials. *Journal of Applied Mechanics*, **42**, 385–389.

Bonora, N. (1997). A nonlinear cdm model for ductile failure. *Engineering Fracture Mechanics*, **58**, 11 – 28.

Bonora, N., Gentile, D., Pirondi, A. and Newaz, G. (2005). Ductile damage evolution under triaxial state of stress: theory and experiments. *International Journal of Plasticity*, **21**, 981 – 1007.

Borst, R.D. (1991). The zero-normal-stress condition in plane stress and shell elastoplasticity. *Communication in applied numerical methods*, **7**, 29fb33.

Boyce, M.C., Parks, D.M. and Argon, A.S. (1988). Large inelastic deformation of glassy polymers. part i: rate dependent constitutive model. *Mechanics of Materials*, **7**, 15–33.

Boyce, M.C., Socrate, S. and Llana, P.G. (2000). Constitutive model for the finite deformation stress-strain behavior of poly(ethylene terephthalate) above the glass transition. *Polymer*, **41**, 2183–2201.

Brunig, M. (2003). An anisotropic ductile damage model based on irreversible thermodynamics. *International Journal of Plasticity*, **19**, 1679 – 1713.

Brunig, M., Chyra, O., Albrecht, D., Driemeier, L. and Alves, M. (2008). A ductile damage criterion at various stress triaxialities. *International Journal of Plasticity*, **24**, 1731 – 1755.

CASTRENZE AND POLIZZOTTO (2011). A unified residual-based thermodynamic framework for strain gradient theories of plasticity. *International Journal of Plasticity*, **27**, 388 – 413.

CELENTANO, D.J. AND CHABOCHE, J.L. (2007). Experimental and numerical characterization of damage evolution in steels. *International Journal of Plasticity*, **23**, 1739 – 1762.

CHABOCHE, J.L. (1997). Thermodynamic formulation of constitutive equations and application to the viscoplasticity and viscoelasticity of metals and polymers. *International Journal of Solids and Structures*, **34**, 2239 – 2254.

CHALLIER, M., BESSON, J., LAIARINANDRASANA, L. AND PIQUES, R. (2006). Damage and fracture of polyvinylidene fluoride (pvdf) at 20°c: Experiments and modelling. *Engineering Fracture Mechanics*, **73**, 79 – 90.

CICEKLI, U., VOYIADJIS, G.Z. AND AL-RUB, R.K.A. (2007). A plasticity and anisotropic damage model for plain concrete. *International Journal of Plasticity*, **23**, 1874 – 1900.

COLAK, O.U. (2005). Modeling deformation behavior of polymers with viscoplasticity theory based on overstress. *International Journal of Plasticity*, **21**, 145–160.

COLAK, O.U. AND DUSUNCELI, N. (2006). Modeling viscoelastic and viscoplastic behavior of high density polyethylene (hdpe). *Journal of Engineering Materials and Technology*, **128**, 572–578.

DASARI, A., SARANG, S. AND MISRA, R. (2004). Strain rate sensitivity of homopolymer polypropylenes and micrometric wollastonite-filled polypropylene composites. *Materials Science and Engineering: A*, **368**, 191–204.

DE BORST, R. AND MÜHLHAUS, H.B. (1992). Gradient-dependent plasticity: Formulation and algorithmic aspects. *International Journal for Numerical Methods in Engineering*, **35**, 521–539.

DE SCIARRA, F.M. (2008). A general theory for nonlocal softening plasticity of integral-type. *International Journal of Plasticity*, **24**, 1411–1439.

DIENES, J.K. (1979). On the analysis of rotation and stress rate in deforming bodies. *Acta Mechanica*, **32**, 217–232, 10.1007/BF01379008.

DODDS, R.H. (1987). Numerical techniques for plasticity computations in finite element analysis. *Computers and Structures*, **26**, 767–779.

DROZDOV, A. AND CHRISTIANSEN, J. (2007). Cyclic viscoplasticity of high-density polyethylene: Experiments and modeling. *Computational Materials Science*, **39**, 465 – 480.

DROZDOV, A. AND DE C. CHRISTIANSEN, J. (2007). Viscoelasticity and viscoplasticity of semicrystalline polymers: Structure-property relations for high-density polyethylene. *Computational Materials Science*, **39**, 729–751.

DROZDOV, A.D. AND GUPTA, R.K. (2003). Non-linear viscoelasticity and viscoplasticity of isotactic polypropylene. *International Journal of Engineering Science*, **41**, 2335–2361.

DUSUNCELI, N. AND COLAK, O.U. (2008). Modelling effects of degree of crystallinity on mechanical behavior of semicrystalline polymers. *International Journal of Plasticity*, **24**, 1224 – 1242.

ENGELEN, R.A.B., GEERS, M.G.D. AND BAAIJENS, F.P.T. (2003). Nonlocal implicit gradient-enhanced elasto-plasticity for the modelling of softening behaviour. *International Journal of Plasticity*, **19**, 403–433.

EPEE, A., LAURO, F., BENNANI, B. AND BOUREL, B. (2011). Constitutive model for a semi-crystalline polymer under dynamic loading. *International Journal of Solids and Structures*, **48**, 1590–1599.

FRANK, G.J. AND BROCKMAN, R.A. (2001). A viscoelasticfbviscoplastic constitutive model for glassy polymers. *International Journal of Solids and Structures*, **38**, 5149–5164.

GHONEIM, H. AND CHEN, Y. (1983). A viscoelastic-viscoplastic constitutive equation and its finite element implementation. *Computers & Structures*, **17**, 499–509.

GHORBEL, E. (2008). A viscoplastic constitutive model for polymeric materials. *International Journal of Plasticity*, **24**, 2032–2058.

GOLOGANU, M., LEBLOND, J.B. AND DEVAUX, J. (1993). Approximate models for ductile metals containing non-spherical voidsfbcase of axisymmetric prolate ellipsoidal cavities. *Journal of the Mechanics and Physics of Solids*, **41**, 1723–1754.

G'SELL, C. AND JONAS, J. (1979). Determination of the plastic behaviour of solid polymers at constant true strain rate. *Journal of Materials Science*, **14**, 583–591.

G'SELL, C., ALY-HELAL, N.A. AND JONAS, J.J. (1983). Effect of stress triaxiality on neck propagation during the tensile stretching of solid polymers. *Journal of Materials Science*, **18**, 1731–1742.

G'SELL, C., HIVER, J.M. AND DAHOUN, A. (2002). Experimental characterization of deformation damage in solid polymers under tension, and its interrelation with necking. *International Journal of Solids and Structures*, **39**, 3857–3872.

G'SELL, C., BAI, S.L. AND HIVER, J.M. (2004). Polypropylene/polyamide 6/polyethylenefboctene elastomer blends. part 2: volume dilatation during plastic deformation under uniaxial tension. *Polymer*, **45**, 5785–5792.

GURSON, A.L. (1977). Continuum theory of ductile rupture by void nucleation and growth, 1. Yield criteria and flow rules for porous ductile media. *Journal of Engineering Materials and Technology-Transactions of the ASME 99(1)*, 2–15.

HADAL, R. AND MISRA, R. (2004). The influence of loading rate and concurrent microstructural evolution in micrometric talc- and wollastonite-reinforced high isotactic polypropylene composites. *Materials Science and Engineering: A*, **374**, 374–389.

HADAL, R., DASARI, A., ROHRMANN, J. AND MISRA, R. (2004). Effect of wollastonite and talc on the micromechanisms of tensile deformation in polypropylene composites. *Materials Science and Engineering: A*, **372**, 296–315.

HADDAG, B., ABED-MERAIM, F. AND BALAN, T. (2009). Strain localization analysis using a large deformation anisotropic elasticfbplastic model coupled with damage. *International Journal of Plasticity*, **25**, 1970 – 1996.

HAMMI, Y. AND HORSTEMEYER, M. (2007). A physically motivated anisotropic tensorial representation of damage with separate functions for void nucleation, growth, and coalescence. *International Journal of Plasticity*, **23**, 1641 – 1678.

HAN, C.D. (1985). *Mechanical properties of solid polymers*. John Wiley & Sons.

HAWARD, R.N. AND THACKRAY, G. (1968). The use of a mathematical model to describe isothermal stress-strain curves in glassy thermoplastics. *Proceedings of the Royal Society of London. Series A. Mathematical and Physical Sciences*, **302**, 453–472.

HO, K. AND KREMPL, E. (2002). Extension of the viscoplasticity theory based on overstress (vbo) to capture non-standard rate dependence in solids. *International Journal of Plasticity*, **18**, 851–872.

JEONG, H.Y. AND PAN, J. (1995). A macroscopic constitutive law for porous solids with pressure-sensitive matrices and its implications to plastic flow localization. *International Journal of Solids and Structures*, **32**, 3669–3691.

Jerabek, M., Major, Z., Renner, K., Mcz, J., Puknszky, B. and Lang, R.W. (2010). Filler/matrix-debonding and micro-mechanisms of deformation in particulate filled polypropylene composites under tension. *Polymer*, **51**, 2040–2048.

Jetteur, P. (1986). Implicit integration algorithm for elastoplasticity in plane stress analysis. *Engineering Computations*, **3**, 251–253.

Jirásek, M. and Rolshoven, S. (2003). Comparison of integral-type nonlocal plasticity models for strain-softening materials. *International Journal of Engineering Science*, **41**, 1553–1602, damage and failure analysis of materials.

Johnson, G.C. and Bammann, D.J. (1984). A discussion of stress rates in finite deformation problems. *International Journal of Solids and Structures*, **20**, 725 – 737.

Kachanov, L. (1958). Time of the rupture process under creep conditions. *Izv Akad Nauk USSR Otd Tekh Nauk*, **8**, 26–31, (in Russian).

Katz, H. and Mileski, J. (1988). *Handbook Of Fillers For Plastics*. New York: Springer-Verlag.

Khan, A. and Zhang, H. (2001). Finite deformation of a polymer: experiments and modeling. *International Journal of Plasticity*, **17**, 1167 – 1188.

Khan, A.S. and Farrokh, B. (2006). Thermo-mechanical response of nylon 101 under uniaxial and multi-axial loadings: Part i, experimental results over wide ranges of temperatures and strain rates. *International Journal of Plasticity*, **22**, 1506–1529.

Khan, A.S., Lopez-Pamies, O. and Kazmi, R. (2006). Thermo-mechanical large deformation response and constitutive modeling of viscoelastic polymers over a wide range of strain rates and temperatures. *International Journal of Plasticity*, **22**, 581 – 601.

Khan, F. and Yeakle, C. (2011). Experimental investigation and modeling of non-monotonic creep behavior in polymers. *International Journal of Plasticity*, **27**, 512 – 521.

Kim, J.S. and Muliana, A.H. (2010). A combined viscoelasticfbviscoplastic behavior of particle reinforced composites. *International Journal of Solids and Structures*, **47**, 580–594.

Krempl, E. and Ho, K. (2001). Section 5.6 - inelastic compressible and incompressible, isotropic, small strain viscoplasticity theory based on overstress (vbo). In J. Lemaitre, ed., *Handbook of Materials Behavior Models*, 336 – 348, Academic Press, Burlington.

KREMPL, E. AND KHAN, F. (2003). Rate (time)-dependent deformation behavior: an overview of some properties of metals and solid polymers. *International Journal of Plasticity*, **19**, 1069–1095.

KREMPL, E., MCMAHON, J. AND YAO, D. (1986). Viscoplasticity based on overstress with a differential growth law for the equilibrium stress. *Mechanics of Materials*, **5**, 35 – 48.

LAIARINANDRASANA, L., BESSON, J., LAFARGE, M. AND HOCHSTETTER, G. (2009). Temperature dependent mechanical behaviour of pvdf: Experiments and numerical modelling. *International Journal of Plasticity*, **25**, 1301 – 1324.

LAURO, F., BENNANI, B., DRAZETIC, P., OUDIN, J. AND NI, X. (1997). Damage occurrence under dynamic loading for strain rate sensitive materials. *Communications in Numerical Methods in Engineering*, **13**, 113–126.

LAURO, F., BENNANI, B., DRAZETIC, P., OUDIN, J. AND NI, X. (1998). Damage occurrence under dynamic loading for anisotropic strain rate sensitive materials. *Shock and Vibration*, **5**, 43–51.

LAURO, F., BENNANI, B., MORIN, D. AND EPEE, A. (2010). The see method for determination of behaviour laws for strain rate dependent material: Application to polymer material. *International Journal of Impact Engineering*, **37**, 715–722, impact Loading of Lightweight Structures.

LAZZERI, A. AND BUCKNALL, C.B. (1995). Applications of a dilatational yielding model to rubber-toughened polymers. *Polymer*, **36**, 2895–2902.

LEE, B.J., PARKS, D.M. AND AHZI, S. (1993). Micromechanical modeling of large plastic deformation and texture evolution in semi-crystalline polymers. *Journal of the Mechanics and Physics of Solids*, **41**, 1651–1687.

LEMAITRE, J. (1985a). A continuous damage mechanics model for ductile fracture. *Journal of Engineering Materials and Technology*, **107**, 83–89.

LEMAITRE, J. (1985b). Coupled elasto-plasticity and damage constitutive equations. *Computer Methods in Applied Mechanics and Engineering*, **51**, 31–49.

LEMAITRE, J. (1996). *A course on damage mechanics.*

LORET, B. AND PREVOST, J.H. (1990). Dynamic strain localization in elasto-(visco-)plastic solids, part 1. general formulation and one-dimensional examples. *Computer Methods in Applied Mechanics and Engineering*, **83**, 247–273.

MILED, B., DOGHRI, I. AND DELANNAY, L. (2011). Coupled viscoelasticfbviscoplastic modeling of homogeneous and isotropic polymers: Numerical algorithm and analytical solutions. *Computer Methods in Applied Mechanics and Engineering*, **200**, 3381–3394.

MORA, V. (2004). *Etude de l'intégration temporelle du tenseur taux de déformation Application la modélisation de l'élastoplasticit en grandes transformations*. Ph.D. thesis, Université de Bretagne-Sud, [S.l.].

MOSS, W.C. (1984). On instabilities in large deformation simple shear loading. *Computer Methods in Applied Mechanics and Engineering*, **46**, 329 – 338.

NAHSHON, K. AND HUTCHINSON, J. (2007). Modification of the gurson model for shear failure. *European Journal of Mechanics - A/Solids*, **27**, 1–17.

NEEDLEMAN, A. (1988). Material rate dependence and mesh sensitivity in localization problems. *Computer Methods in Applied Mechanics and Engineering*, **67**, 69–85.

NEEDLEMAN, A. AND TVERGAARD, V. (1998). Dynamic crack growth in a nonlocal progressively cavitating solid. *European Journal of Mechanics - A/Solids*, **17**, 421–438.

NEMAT-NASSER, S. (1982). On finite deformation elasto-plasticity. *International Journal of Solids and Structures*, **18**, 857 – 872.

NIKOLOV, S. AND DOGHRI, I. (2000). A micro/macro constitutive model for the small-deformation behavior of polyethylene. *Polymer*, **41**, 1883–1891.

PARKS, D.M. AND AHZI, S. (1990). Polycrystalline plastic deformation and texture evolution for crystals lacking five independent slip systems. *Journal of the Mechanics and Physics of Solids*, **38**, 701–724.

PERZYNA, P. (1966). Fundamental problems in viscoplasticity. *Advances in Applied Mechanics*, **9**, 243–377.

PIJAUDIER-CABOT, G. AND BAŽANT, Z. (1987). Nonlocal damage theory. *Journal of Engineering Mechanics*, **113**, 1512–1533.

PIJAUDIER-CABOT, G., BAANT, Z.P. AND TABBARA, M. (1988). Dynamic strain localization in elasto-(visco-)plastic solids, part 1. general formulation and one-dimensional examples. *Engineering Computations*, **5**, 141–150.

PIJNENBURG, K.G.W. AND DER GIESSEN, E.V. (2001). Macroscopic yield in cavitated polymer blends. *International Journal of Solids and Structures*, **38**, 3575–3598.

PIRONDI, A., BONORA, N., STEGLICH, D., BROCKS, W. AND HELLMANN, D. (2006). Simulation of failure under cyclic plastic loading by damage models. *International Journal of Plasticity*, **22**, 2146 – 2170.

RAGHAVA, R., CADDELL, R.M. AND YEH, G.S.Y. (1973). The macroscopic yield behaviour of polymers. *Journal of Materials Science*, **8**, 225–232.

REGRAIN, C., LAIARINANDRASANA, L., TOILLON, S. AND SAÏ, K. (2009). Multi-mechanism models for semi-crystalline polymer: Constitutive relations and finite element implementation. *International Journal of Plasticity*, **25**, 1253–1279.

SAUER, J.A. AND PAE, K.D. (1974). The flow of solid polymers under high pressure. *Colloid and Polymer Science*, **252**, 680–695, 10.1007/BF01554493.

SCHAPERY, R.A. (1969). On the characterization of nonlinear viscoelastic materials. *Polymer Engineering & Science*, **9**, 295fb310.

SCHREYER, H.L., KULAK, R.F. AND KRAMER, J.M. (1979). Accurate numerical solutions for elastic-plastic models. *Journal of Pressure Vessel Technology*, **101**, 226–234.

SIMO, J.C. AND HUGHES, T.J.R. (1998). *Computational Inelasticity*. Interdisciplinary Applied Mathematics, New York: Springer-Verlag.

SIMO, J.C. AND TAYLOR, R.L. (1985). Consistent tangent operators for rate-independent elastoplasticity. *Computer Methods in Applied Mechanics and Engineering*, **48**, 101–118.

SIMO, J.C. AND TAYLOR, R.L. (1986). A return mapping algorithm for plane stress elastoplasticity. *International Journal for Numerical Methods in Engineering*, **22**, 649–670.

STAVERMAN, A.J. AND SCHWARZL, P. (1925a). Non equilibrium thermodynamics of viscoelastic behaviour. *Proceeding Academic sciences, The Netherlands*, **55**, 486–492.

STAVERMAN, A.J. AND SCHWARZL, P. (1925b). Thermodynamics of viscoelastic behaviour (model theory). *Proceeding Academic sciences, The Netherlands*, **55**, 474–485.

STEENBRINK, A.C., GIESSEN, E.V.D. AND WU, P.D. (1997). Void growth in glassy polymers. *Journal of the Mechanics and Physics of Solids*, **45**, 405fb437.

STRÖMBERG, L. AND RISTINMAA, M. (1996). FE-formulation of a nonlocal plasticity theory. *Computer Methods in Applied Mechanics and Engineering*, **136**, 127–144.

TSCHOEGL, N.W. (1989). The Phenomenological Theory of Linear Viscoelastic Behavior: an Introduction.

TVERGAARD, V. (1982). Material failure by void coalescence in localized shear bands. *International Journal of Solids and Structures*, **18**, 659–672.

TVERGAARD, V. AND NEEDLEMAN, A. (1984). Analysis of the cup-cone fracture in a round tensile bar. *Acta Metallurgica*, **32**, 157–169.

TVERGAARD, V. AND NEEDLEMAN, A. (1995). Effects of nonlocal damage in porous plastic solids. *International Journal of Solids and Structures*, **32**, 1063–1077.

VAN DOMMELEN, J.A.W., PARKS, D.M., BOYCE, M.C., BREKELMANS, W.A.M. AND BAAIJENS, F.P.T. (2003). Micromechanical modeling of the elasto-viscoplastic behavior of semi-crystalline polymers. *Journal of the Mechanics and Physics of Solids*, **51**, 519–541.

VOYIADJIS, G.Z. AND ABED, F.H. (2006). A coupled temperature and strain rate dependent yield function for dynamic deformations of bcc metals. *International Journal of Plasticity*, **22**, 1398 – 1431.

VOYIADJIS, G.Z. AND AL-RUB, R.K.A. (2003). Thermodynamic based model for the evolution equation of the backstress in cyclic plasticity. *International Journal of Plasticity*, **19**, 2121 – 2147.

VOYIADJIS, G.Z. AND DORGAN, R.J. (2007). Framework using functional forms of hardening internal state variables in modeling elasto-plastic-damage behavior. *International Journal of Plasticity*, **23**, 1826 – 1859.

VOYIADJIS, G.Z., PEKMEZI, G. AND DELIKTAS, B. (2010). Nonlocal gradient-dependent modeling of plasticity with anisotropic hardening. *International Journal of Plasticity*, **26**, 1335 – 1356.

VOYIADJIS, G.Z., SHOJAEI, A. AND LI, G. (2012). A generalized coupled viscoplasticfbviscodamagefbviscohealing theory for glassy polymers. *International Journal of Plasticity*, **28**, 21 – 45.

WANG, D.A. AND PAN, J. (2006). A non-quadratic yield function for polymeric foams. *International Journal of Plasticity*, **22**, 434–458.

WIERZBICKI, T., BAO, Y., LEE, Y.W. AND BAI, Y. (2005). Calibration and evaluation of seven fracture models. *International Journal of Mechanical Sciences*, **47**, 719–743.

WU, P.D. AND VAN DER GIESSEN, E. (1995). On neck propagation in amorphous glassy polymers under plane strain tension. *International Journal of Plasticity*, **11**, 211–235.

XIAO, H., BRUHNS, O.T. AND MEYERS, A. (2000). The choice of objective rates in finite elastoplasticity: general results on the uniqueness of the logarithmic rate. *Proceedings of the Royal Society of London. Series A: Mathematical, Physical and Engineering Sciences*, **456**, 1865–1882.

XUE, L. (2007). Damage accumulation and fracture initiation in uncracked ductile solids subject to triaxial loading. *International Journal of Solids and Structures*, **44**, 5163–5181.

ZAÏRI, F., NAÏT-ABDELAZIZ, M., WOZNICA, K. AND GLOAGUEN, J.M. (2005). Constitutive equations for the viscoplastic-damage behaviour of a rubber-modified polymer. *European Journal of Mechanics - A/Solids*, **24**, 169 – 182.

ZAÏRI, F., NAÏT-ABDELAZIZ, M., GLOAGUEN, J. AND LEFEBVRE, J. (2008). Modelling of the elasto-viscoplastic damage behaviour of glassy polymers. *International Journal of Plasticity*, **24**, 945 – 965.

Abstract

Polymer materials are widely used for structural applications in the automotive sector and their behaviours are complex and require accurate models for finite element simulations. Polymer materials exhibit rate and time dependent behaviours. The rate dependency can be observed by an increase of the stiffness and the yield stress at increasing strain rate. The long time to recover the zero stress after solicitation of the material highlight the time dependent behaviour. Furthermore, particularly for filled polymers, the cavitation phenomenon cause the creation and growth of micro-voids and micro-cracks called damage and leads to volume change during the deformation. In this work, a behaviour model for mineral filled semi-crystalline polymer used in automotive industry is developed. A constitutive viscoelastic-viscoplastic non-associated model coupled with nonlocal damage is proposed in order to simulate the phenomena observed experimentally. In the constitutive model, a non symmetric yield surface is used to take the hydrostatic pressure into account. The non associated viscoplasticity coupled with damage leads to the non-isochoric viscoplastic deformation characterised experimentally. The material parameters arise from experimental tests carried out under various loadings and strain rates. For these experimental tests, different measurement techniques like Digital Image Correlation and optical extensometry are used for the displacements and the strain field measurements. The good agreement between the experimental data and the numerical simulations highlights the accuracy of the developed model for polymer modelling.

Résumé

Les matériaux polymères sont largement utilisés pour des applications structurelles dans le secteur automobile et leurs comportements complexes nécessitent des modèles précis pour la simulation éléments finis. Les polymères possèdent un comportement dépendant du temps et de la vitesse. La dépendance à la vitesse peut être observée par un accroissement de la rigidité et de la limite élastique en fonction de la vitesse de déformation. Le long temps nécessaire pour retrouver des contraintes nulles après sollicitation du matériau met en évidence la dépendance du temps sur le comportement. De plus, particulièrement pour les polymères chargés, le phénomène de cavitation se traduisant par la création et la croissance de micro-cavités et de micro-fissures conduit à un changement de volume durant la déformation. Dans ce travail, un modèle de comportement est développé pour un polymère semi-cristallin chargé de talc utilisé dans l'industrie automobile. Un modèle constitutif viscoélastique-viscoplastique non-associatif avec endommagement non-local est proposé dans le but de simuler les phénomnes observés expérimentalement. Dans le modèle développé, une surface de charge non-symétrique est utilisée pour prendre en compte la pression hydrostatique. La viscoplasticité non-associative couplée avec l'endommagement conduit aux déformations viscoplastiques non-isochoriques caractérisées expérimentalement. Les paramètres du modèle proviennent d'essais expérimentaux réalisés sous différentes conditions et à différentes vitesses de déformation. Pour ces essais, plusieurs techniques de mesure, telles que la corrélation d'images et l'extensommetrie optique sont utilisées pour les mesures de champs de déplacements. La bonne corrélation entre les données expérimentales et les simulations numériques mettent en évidence la précision du modèle développé afin de modéliser le comportement des matériaux polymères semi-cristallins.